ABSTRACT

Title of dissertation: RESPONSE OF PREMIXED HYDROCARBON FLAMES WITH AND WITHOUT HYDROGEN ADDITION TO STEADY AND OSCILLATORY STRAIN RATES

Joseph M. Plaia, Doctor of Philosophy, 2005

Dissertation directed by: Professor Gregory Jackson
Department of Mechanical Engineering

The response to steady-state and oscillatory strain rates of lean, premixed hydrocarbon-air flames with and without H_2 doping has been investigated analytically, numerically and experimentally. The analytical analysis provides a theoretical framework for assessing steady-state flame temperature (T_{flame}) response to strain rate as a function of reactant composition, through Lewis numbers (Le_k), and of non-dimensional stretch defined by the Karlovitz number (Ka). An integral analysis with discrete reaction zones for each fuel has been developed, capturing the linear response of T_{flame} to Ka (<0.2) for steady-state CH_4-H_2 and C_3H_8-H_2 lean flames as predicted by numerical models using full chemistry (GRI-Mech V3.0). This method improves predictions from single-flame zone integral analyses.

Detailed transient numerical simulations using GRI-Mech V3.0 determined the effects of H_2 addition on CH_4 premixed flame responses to strain oscillations. Symmetric velocity (pressure) oscillations in an opposed jet counterflow configuration were simulated for frequencies, f, ranging from 100 to 1000Hz, focusing on behavior at large Ka, near extinction. The oscillations cause flame characteristics (e.g. species mass

fractions and T_{flame}) to vary significantly from steady-state responses. While flame responses to 100Hz oscillations closely follow quasi-steady behavior, responses for f>200Hz deviate, with phase lags and different amplitudes, from quasi-steady predictions. At f=1000Hz, the flame acts as a low pass filter, reducing amplitudes in property oscillations compared to quasi-steady analysis. For the higher frequencies, predictions indicate premixed flames can persist momentarily beyond steady-state extinction strain rate limits during oscillations.

Strain rate oscillation amplitudes required to extinguish flames, A_{ext}, are determined numerically with the computational model and compared with experimental measurements. Simulations show that A_{ext} increases with f due to attenuated flame response for f>200Hz. Increasing flame equivalence ratio, ϕ, and/or percentage of O_2 consumed by H_2, α, increases reaction rates, decreasing the deviation from quasi-steady behavior and reducing the relative A_{ext}. Counterflow premixed flame experiments with upstream speaker-imposed oscillations are also used to evaluate A_{ext}. Phase-locked velocity measurements (with laser Doppler anemometry) assist in understanding how upstream pressure oscillations translate into velocity field (strain rate) oscillations. Measured A_{ext} values validated trends in the computational results.

RESPONSE OF PREMIXED HYDROCARBON FLAMES WITH AND WITHOUT HYDROGEN ADDITION TO STEADY AND OSCILLATORY STRAIN RATES

By

Joseph M. Plaia

Dissertation submitted to the Faculty of the Graduate School of the
University of Maryland, College Park, in partial fulfillment
of the requirements for the degree of
Doctor of Philosophy
2005

Advisory Committee:
Professor Gregory Jackson, Chair
Professor James Baeder
Professor Kenneth Kiger
Professor James Wallace
Professor Kenneth Yu

Acknowledgements

I would like to thank my advisor, Dr. Gregory Jackson, for his prodigious assistance and encouragement in bringing this dissertation to its conclusion. I also extend my gratitude to all my fellow students in the Reacting Flow Lab who were available to lend a hand whenever asked. Finally, I must thank my wife, whose unwavering support made this possible.

Table of Contents

List of Tables

List of Figures

Nomenclature

A	relative amplitude of imposed oscillation
A	flow cross sectional area
A_{ext}	extinction amplitude of oscillation
$A_{ext\text{-}1}$	oscillation amplitude one step prior to the A_{ext}
A_{fit}	amplitude of oscillation curve fit to experimental measurements
A_{flame}	cross sectional area at location of final reaction zone in integral analyses
A_{meas}	measure amplitudes from experiments
$A_{m,k}$	cross sectional area at beginning of mass diffusion zone for species k
A_n	cross sectional area at location of reaction zone n
A_0	cross sectional area of flow upstream of diffusion zones
B_k	the effective frequency factor for single step reaction of species k
c_p	constant pressure specific heat of mixture
$c_{p,k}$	constant pressure specific heat for species k
dP	pressure difference at counterflow stagnation plane between mean and maximum velocity oscillations
D	diameter of a seed particle
D_k	species mass diffusion
$D_{k,j}$	binary diffusion coefficients for species k and j
D_k^T	thermal diffusion coefficients for species k
f	frequency of imposed oscillations
f_D	measured frequency of scattered light in LDA measurements
f_0	frequency shift between the two intersecting laser beams
h_k	enthalpy of species k
Ka	Karlovitz number, non-dimensional strain
E_k	exponential term for the first order reaction for species k
Le_{eff}	effective Lewis number for a mixture
Le_k	Lewis number of species k
$\ell_{m,k}$	length of mass diffusion zone for species k
ℓ_T	length of overall thermal diffusion zone
$\ell_{T,n}$	length of thermal diffusion zone associated with flame n
$\dot{m}$	mass flow rate
P	excess gauge pressure ($P_{tot} - P_{atm}$)
P_{atm}	absolute atmospheric pressure
$P_{0,max}$	gauge stagnation pressure at stagnation plane at maximum velocity
$P_{0,mean}$	gauge stagnation pressure at stagnation plane at mean velocity
P_{tot}	total absolute pressure
q_k	heat of combustion for species k per unit mass
Q_k	heat release for species n (Y_k * q_k) per unit mass
$\hat{q}_k$	ratio of heat release from species k to total heat release of mixture
$\hat{Q}$	sum of heat release for all fuel species in the mixture per unit mass
r	radial direction from centerline in counterflow domain
R	universal gas constant

St_v	Stokes number
S_L	flame thickness
S^0_{flame}	laminar flame speed with zero imposed strain
t	time
T	temperature
T_{flame}	maximum temperature of the flame
T_n	temperature at discrete reaction zone n
T^0	combustion temperature for an unstrained flame
T_0	initial upstream temperature in integral analysis
ΔT^0	change in temperature associated with unstrained flame
u	axial velocity
$\overline{U}$	mean axial velocity
U_{in}	inlet axial velocity
U_k	axial diffusion velocity of species k
U_{max}	maximum imposed axial velocity during oscillation
U_{mean}	mean axial velocity from the steady state initial case
U_x	velocity component normal to the interference fringe pattern
v	radial velocity
V	radial velocity ratio v/r
V_{AC}	AC voltage of signal sent to speakers
$\overline{W}$	mixture average molecular weight
W_k	molecular weight of species k
x	axial distance along centerline of counterflow domain
x^+_{flame}	x location of the downstream side of the reaction zone
x^-_{flame}	x location of the upstream side of the reaction zone
X_k	mole fraction of species k
Y_k	mass fraction of species k
$Y_{k,0}$	initial, upstream mass fraction of species k
α	fraction of O_2 consumed by H_2 assuming complete combustion
α	mixture thermal diffusion coefficient
θ	angle between the two incident laser beams
κ	counterflow flow field strain rate
κ_{init}	strain rate of initial steady state solution
κ_{ext}	steady state extinction strain rate
λ	mixture conductivity
λ	laser wavelength
Λ	radial pressure eigenvalue for one-dimensional counterflow domain
μ	mixture average viscosity
μ_{art}	artificial viscosity
μ	viscosity of carrier fluid
ρ	mixture density of the gas phase
ρ_d	density of carrier fluid
τ	relative flame timescale
τ_v	viscous timescale of carrier flow

τ_f	fluid timescale
ϕ	equivalence ratio
Φ	time integral of Λ ($d\Phi/dt = \Lambda(t)$)
$\dot{\omega}_k$	generation rate of species k per unit volume

Chapter 1 Introduction

1.1 Background and Motivation

Power generation, transportation, and manufacturing are some of the important industries impacted by the current knowledge in combustion processes. Even after many years of research into combustion phenomena, there remain many areas in which the engineer's knowledge is incomplete. Fundamental research into premixed gaseous combustion is still providing new and deeper understanding to model and predict advanced low-emissions combustor behavior. Much of the combustor development for gas turbines, boilers, and other stationary combustion systems for power generation is aimed at reducing the production of pollutants and increasing efficiency through the development of high-temperature, lean, premixed combustors. Further progress in the design of lean combustors will require advances in several areas of combustion research. This study focuses on improving the understanding how fuel mixtures of multiple components affects both transient and steady state combustion properties. Increased knowledge in this area may lead to improved turbulent premixed combustion models of complex multicomponent, realistic fuels, including fuels such as syngas, natural gas, and vaporized liquid fuels.

Lean premixed combustion reduces emissions of carbon monoxide and unburned hydrocarbons as long as good flame stability is maintained. Reduced combustion temperatures, resulting from burning lean mixtures, reduce the production of nitrogen oxide compounds (NO_x), a key component in the production of smog. However, design and operation of lean combustors is problematic. Difficulties arise from the fact that when the combustors are run at equivalence ratios less than 0.5, the temperatures are low

enough (~1600K) to maintain NO_x emissions less than 10ppm, but the flames are on the edge of extinction [1]. Small perturbations in the combustion conditions, caused by interactions between the combustion and gas dynamic processes, may lead to flame extinction or excessive emissions of CO or unburned hydrocarbons. For reliable combustor operation, methods to extend the lean extinction limits are needed, and optimization of such methods requires further understanding of the behavior of lean flames in response to transient conditions associated with turbulent fluctuations present in combustors. The turbulent conditions in lean combustors preclude the use of simplified laminar combustion model. Furthermore, turbulent combustion models using detailed chemistry for predicting extinction and NO_x formation are typically impractical for large scale systems. Improving simplified turbulent combustion models will lead to improved lean combustor designs.

Some research has been conducted to investigate the use of multicomponent fuels for improving combustor operation. For example, the addition of H_2 to another gaseous fuel may increase the stability of a flame [1-5]. Even common fuels like natural gas are inherently multicomponent, containing mixtures of CH_4 and other light hydrocarbons. The typical composition of domestic natural gas can be seen in Table 1.1. In addition, as the United States increases importation of liquefied natural gas, the variation in natural gas composition will increase. Also, with the increasing interest in alternative fuels, reformed fuels and coal or biomass gasification fuels are becoming more important for future power generation systems. Steam reforming of CH_4 and coal gasification produces primarily syngas, a mixture of H_2 and CO [6, 7], and such mixtures are being used in existing IGCC (integrated gasification combined cycle) plants. Reformate or partially

reformed fuels are being considered for future low emissions combustion applications [8]. Although all these multi-component fuels are becoming more important in industrial combustion processes, there is currently a limited understanding of their behavior during unsteady combustion.

Table 1.1: Average composition of natural gas in the United States [7].

Component	Methane	Ethane	Propane	trace
Percentage	93.9	3.2	0.7	2.2

Finally, much of the past combustion research has focused on steady state conditions. As computing power has increased, the ability to model transient conditions has improved. Researchers are beginning to take advantage of this improved modeling capability to investigate transient combustion performance. Most real systems, even when designed for steady state operation, are still subject to oscillations. Gas turbines exhibit oscillations typically in the 100-1000Hz range upstream of the combustors [9] and internal combustion engines operate under continuously transient conditions. Improved understanding of the transient combustion process may allow designers to improve the performance of such combustors.

Results from combustion investigations using well defined transient flames will inform model development for turbulent flames, particularly under conditions where the turbulent flame can be modeled as a wrinkled sheet. Such conditions arise when the flame zone thickness, S_L, and the chemical reaction timescales are much smaller, respectively, than the integral length scale and timescale of the turbulent flow field. The

flame may be considered independent of the turbulence. Under such conditions, the flamelet model of turbulent combustion assumes that although the flame front may be turbulent on the macro scale, at scales smaller than the turbulence integral length the turbulent flame front may be modeled as a collection of contiguous laminar flames otherwise referred to as flamelets. In this approach, the large scale flow field is computed from the conservation equations and the flame front properties are then interpolated from precomputed libraries of steady state flame properties. The flamelet approach allows the inclusion of turbulent combustion in a large scale combustion model. However, because the flamelet libraries are based on steady state flames, the interpolated flame properties cannot provide the effects of fast flow field transients on the flamelet. As turbulence is by definition transient, incorporating transient combustion effects in the flamelet libraries may lead to increased accuracy of the overall combustion model.

1.2 Literature Survey

1.2.1 Counterflow flames

Counterflow flames have been long established as outstanding means of investigating combustion phenomena. The techniques used to produce counterflow flames have been categorized into three types [10]. All three of the counterflow methods generate a stagnation plane from the interaction of two opposed gas flows and the flames are stabilized at an offset distance from this plane. Type I burners use premixed gasses flowing around and through a porous cylinder. Type II burners use two vertically opposed porous plates and Type III burners use two vertically opposed converging nozzles. In this study, a Type III configuration was used. Two vertically opposed converging nozzles produce a nearly uniform flow field that stagnates at a small

separation distance relative to the nozzle diameter. During premixed combustion, nearly planar flame fronts form on either side of the stagnation plane. A schematic of the counterflow design for this study may be seen in Figure 1.1.

The advantage of using a counterflow flame is its simplicity. If the distance between the stagnation plane and the nozzle exit is small compared to the nozzle exit diameter, property variation in the radial direction may be minimized. The aerodynamic flow within the counterflow domain, ignoring consideration of the expansion associated with the combustion reactions, resembles the potential field associated with two point sources for radial nozzles and two line sources for long rectangular nozzles. Such potential flow fields can be defined by the derivative of the velocity between the two point sources, which serves as an eigenvalue of the flow. Along the centerline of the flow from nozzle to nozzle, the radial variations go to zero, $(\partial()/\partial r = 0)$. Additionally, the axisymmetric flow makes variations in the circumferential direction zero, $\partial()/\partial\theta = 0$. Therefore, at the centerline between the two nozzles, properties only vary along the axial distance, x. It has been shown that the laminar flame speed depends strongly on the local stretch, $-du/dx$, independent of the separation distance as long as the separation distance is only one nozzle diameter or less [4]. This simplification to modeling only the one-dimensional behavior along the centerline allows detailed chemical kinetics and diffusion transport to be included in a computational model without requiring excessive computational time.

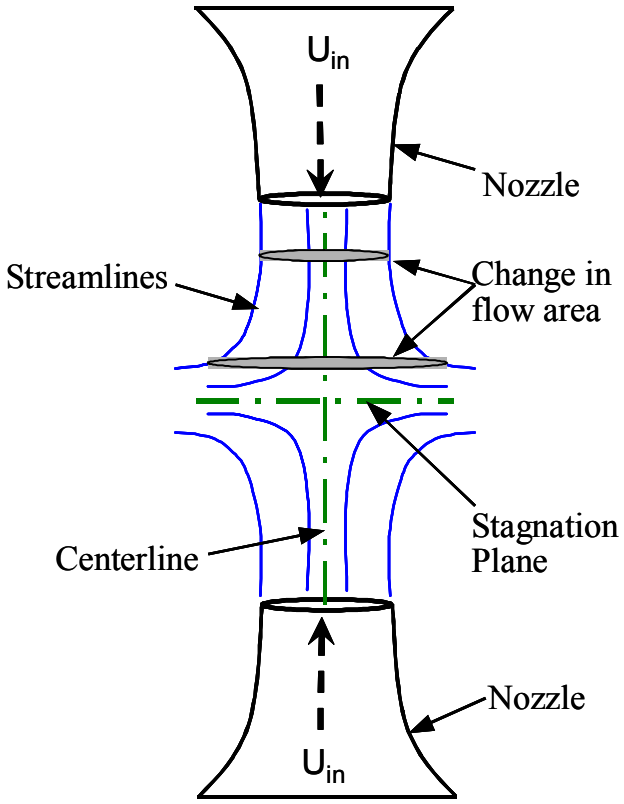

Figure 1.1: Schematic of the opposed nozzle counterflow configuration with important aspects labeled.

There are, however, disadvantages in using a counterflow technique. First, in premixed flame studies, the two flame fronts may interact, and any interactions may be difficult to quantify. This is especially true for highly strained flames, near extinction, where the flames stabilize near the stagnation plane. This double flame effect in counterflow premixed flame studies may be eliminated by using hot products flowing out of one nozzle and the premixed reactants from the other [11]. A second disadvantage is the experimental difficulty of limiting the heat lost to the nozzles. Furthermore, when using low speed flows, buoyancy forces become significant compared to the flow momentum. The buoyancy forces may impart curvature and edge instabilities to the otherwise planar flame. Increasing the temperature of the premixed flow exiting the

nozzle may reduce these last two difficulties. The preheated flow heats the nozzle and once it has reached a quasi-steady operating temperature, heat loss to the nozzles is reduced. Also, the higher initial temperatures allow the lean flame to exist at higher velocities, thereby reducing the significance of the buoyancy forces [1, 2, 12].

The schematic in Figure 1.1 shows that the flow area increases, or stretches, towards the stagnation plane. This is positive stretch and produces positive strain on the flow. Other types of flames, Bunsen burners for example, can experience negative stretch. The strain rate is related to the change in area and is the negative of the velocity gradient as shown in the following equation

$$\kappa = \frac{1}{A}\frac{dA}{dt} = -\frac{du}{dx}, \tag{1.1}$$

where κ is the strain rate, A is the flow cross-sectional area of a moving fluid element, and t is time. The counterflow flow field, with no flame present, has a constant κ; as the axial velocity decreases linearly from the nozzle exit to the stagnation plane.

Figure 1.2 is a plot of the axial velocity and gas temperature profiles from the nozzle to stagnation plane for an example counterflow flame. With a flame present, the heat release from the combustion increases the gas temperature and decreases the density, causing the axial velocity to increase as the flow nears the flame front. Far from the stagnation plane the axial velocity profile is still linear as the thermal effects are only significant in the thermal diffusion zone in which heat diffuses upstream. The non-linear curving of the velocity profiles far from the stagnation plane is due to the boundary condition requiring a zero slope at the nozzle exit. The non-linear variation in velocity means that κ is no longer constant throughout the domain. Therefore, the global strain

for a given flame is determined as the local κ found at the edge of the thermal diffusion zone.

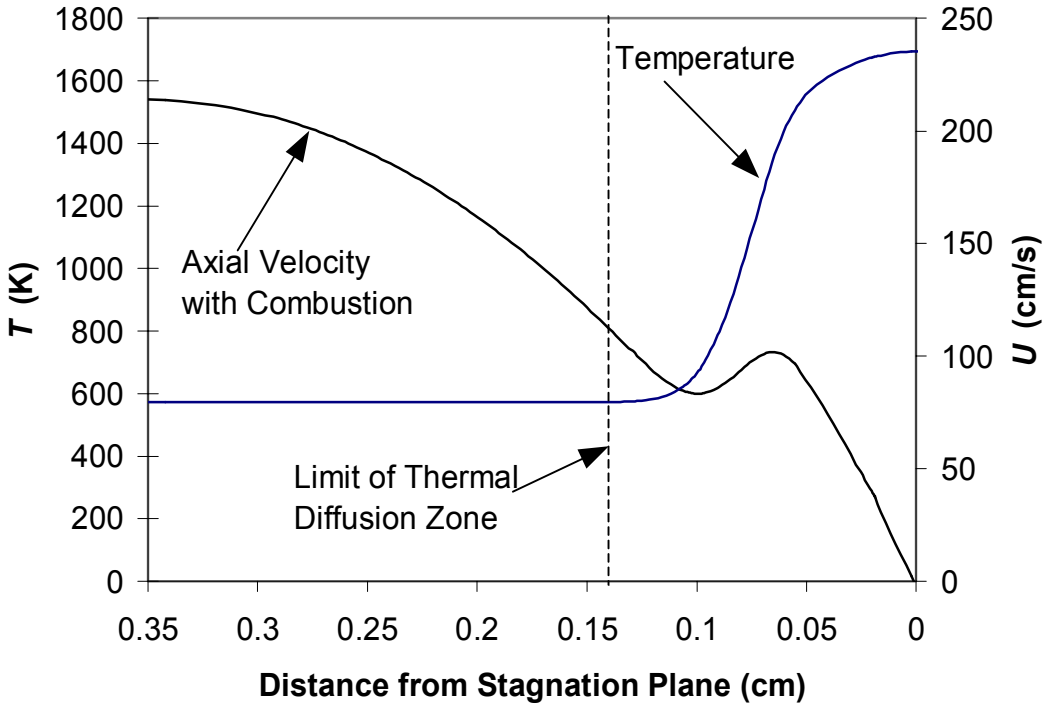

Figure 1.2: Plot of the axial velocity and gas temperature profile over half the counterflow domain for an example of CH_4/H_2-air combustion.

Many studies have investigated how strain alters the behavior of a premixed flame [1, 10, 13-19]. Straining a flame can preferentially increase or decrease the diffusion of species in the flame. As shown in Figure 1.1, as the flow stretches the streamlines diverge and the cross-sectional area increases. The diverging flow decreases the distance between the unburned mixture and the flame surface. The decreased distance increases the gradients of species concentrations and temperature between the flame zone and the upstream mixture. As diffusion is proportional to the gradients, the diffusion rates for the strained flame will differ from the unstrained flame.

The ratio of the thermal diffusion of a mixture to the mass diffusion for an individual species is the Lewis number, Le_k, defined as

$$Le_k = \frac{\alpha}{D_k}, \tag{1.2}$$

where α is the thermal diffusivity of the mixture and D_k is the mass diffusivity of species k with respect to the mixture. A species with a low Le_k has a higher mass diffusion rate than the mixtures heat diffusion. The Lewis number for a mixture, Le_m, is defined as the ratio of the mixture thermal diffusion to the mass diffusion rate of the most deficient major reactant (either fuel or oxidizer). In a lean CH_4-air flame, the deficient species is CH_4. If the mixture has a Le_m <1, CH_4 will preferentially diffuse into the positively strained flame ahead of the bulk flow. This will increase the concentration of CH_4 within the flame and increase the flame temperature. On the other hand, a lean propane flame with its C_3H_8-air reactant mixture typically has a $Le_m > 1$. C_3H_8 has a much lower mass diffusion rate than CH_4. For this situation, the constituents of air will tend to diffuse in the positively stretch flame ahead of the bulk flow, making the flame zone leaner and decreasing the flame temperature.

Several studies have investigated the impacts of preferential diffusion on flame stability and extinction limits. For a flame subject to positive stretch, such as a counterflow flame, reactant species with $Le_k < 1.0$ will diffuse into the flame ahead of the bulk flow. For a lean flame, if the fuel species has the $Le_k < 1.0$, the diffusion into the flame zone makes the flame zone richer than the bulk flow. Furthermore, if a multicomponent fuel is created through the addition of small amounts of H_2 to a lean hydrocarbon flame, the preferential diffusion of H_2 will increase the flame's steady state extinction limit [1, 2, 12, 20, 21]. Previous work has also attempted to predict the affect

of H_2 addition by computing an effective Le_m [20]. Le_m is intended to capture the overall diffusion effects of all the fuel components within a lean fuel-air mixture, and is thus useful for predicting the response of such a flame to stretch (i.e., κ).

1.2.2 Analytical models

Simplified analytical models can often provide insight into complex phenomena by revealing the controlling parameters. Asymptotic analyses have been conducted to determine stretch effects of flame [13, 22-25]. These analyses lead to complex relations that may or may not clearly indicate the relationship between physical parameters and flame behavior. Another method of generating an analytical model is through the use of an integral analysis [14, 16, 18]. Integral, or control volume, analysis is more commonly used in the areas of heat and mass transfer [14]. It can, however, be used in premixed combustion analysis with simplified (often single-step) reaction models to develop an analytical representation of a premixed flame and its surrounding flow field. For a counterflow premixed flame, the integral method can provide a representation of the behavior of the flame with respect to properties such as strain rate, reactant temperatures and Lewis number, *Le*.

These linearized representations are valid for only low strain rates. Higher strain rates result in non-linear flame responses. However, at low κ the integral model may provide information concerning the influence of all the above factors on flame temperature. The model may also provide a simple estimate of the expected flame temperature for a given condition.

In general, the integral analyses have shown that the flame temperature increases with increasing strain if the $Le < 1.0$. The opposite behavior is seen for $Le > 1.0$.

Furthermore, the integral results predict a linear rise or fall in the temperature at a constant rate with increasing strain. The non-linear behavior at higher strain rates is not captured with the linear simplifications. Since extinction is a non-linear behavior, extinction cannot be predicted with the standard integral analysis. Also, for a mixture with $Le < 1.0$, the flame temperature will first increase with increasing strain and then decrease as the flame zone is compressed against the stagnation plane. A recent study has extended the linear analysis to capture the effects of the decreasing flame zone size. This study allows for the prediction of flame extinction in an integral model [18].

1.2.3 Steady state computational models

As mentioned above, the simplicity of the one-dimensional flow field allows a numerical model to include detailed chemical kinetic, thermodynamic and molecular transport models. An example of such a model is the CHEMKIN flame solution code [26, 27]. Also, a transient code based on CHEMKIN has been developed as described further in this study. These one-dimensional, steady state computational models were based on well documented equation sets describing the counterflow regime [28, 29]. They can provide detailed distributions of temperature, pressure, velocities and species mass fractions as they vary through the domain. The aerodynamics of the counterflow region is completely defined by the eigenvalue of the flow. The derivation of the equation sets show that the eigenvalue is the radial pressure gradient divided by the radius,

$$\Lambda = \frac{1}{r}\frac{dP}{dr}. \tag{1.3}$$

This is constant along the center line from nozzle to nozzle, and is related to the strain rate by

$$\kappa = -\frac{du}{dx} = \sqrt{\frac{-4\Lambda}{\rho}}. \tag{1.4}$$

Examples of the results from a steady state code can be seen in Figure 1.2 and Figure 1.3 for an example CH_4/H_2-air flame. Figure 1.2 is plot of the axial velocity and gas temperature profiles from one nozzle exit plane to the stagnation plane. Figure 1.3 is a plot of several species mass fraction profiles from nozzle to nozzle. The profiles on each side of the stagnation plane are identical. The decrease in Y_{H2} and Y_{CH4} towards the stagnation plane illustrates the mass diffusion of the fuel species into the flame zone. The limits of each mass diffusion zone are noted in the plot.

Many studies have used these types of codes to investigate the properties of flames at fixed strain rates to study chemical reaction mechanisms [4], strain rate extinction mechanisms [28, 30], and other aspects of steady state combustion.

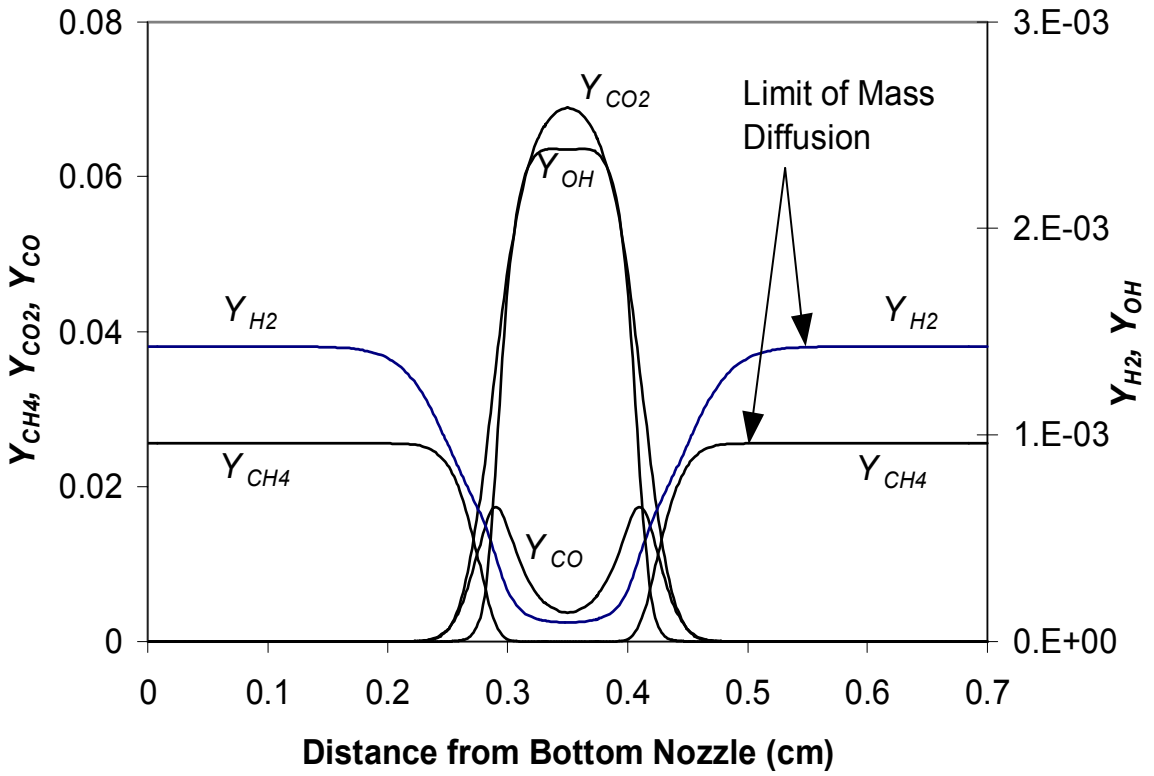

Figure 1.3: Plot of species mass fractions Y_{CO}, Y_{H2}, Y_{CH4} and Y_{OH} for an example counterflow flame burning a mixture of CH_4/H_2-air.

Steady state codes have also been used to determine the steady state flame responses as a function of strain. A series of steady state solutions may be computed at incrementally increasing or decreasing values of strain rate. With such a set of solutions, the change in flame properties, such as flame temperature, combustion product composition or flame speed, with respect to strain rate may be seen. Figure 1.4 shows the temperature profiles over half the counterflow domain for several increasing values of strain rate. A plot of the maximum flame temperature as a function of strain rate can be seen in Figure 1.5 for the same inlet fuel mixture. This curve was constructed by extracting the maximum flame temperature from each computed steady state solution and is typical of a lean, premixed flame with $Le < 1$. Figure 1.5 shows both the upper and

lower branches of the temperature strain curve. The upper branch represents typical, physical flames. The lower branch is a weak solution that may only exist under special circumstances.

As can be seen in Figure 1.5, the flame temperature initially increases with increasing strain. At a critical strain rate, near 800 1/s, the flame temperature reaches a peak and begins to decrease with increasing stain. The decrease is due to the flame region being constrained by the stagnation plane. The increasing inlet velocity pushes the flame closer to the stagnation plane compressing the reaction zones. At this point not all reactions are completed before the flow reaches the stagnation plane. Eventually, κ gets large enough, and the reaction rate low enough, that the heat release in the flame zone cannot diffuse upstream to sustain the early chain branching reactions, and the flame extinguishes [31]. Studies have shown that this extinction limit is approximately 1200K [30], though extinction may occur at higher temperatures. Finally, low strain flames may extinguish due to heat loss from radiation [32].

Figure 1.5 also illustrates the relation between the global strain rate, κ, and the non-dimensional strain rate called the Karlovitz number, *Ka*. *Ka* is related to κ by the following equation

$$Ka = \frac{\alpha\kappa}{S^0_{flame}}.$$

In the above equation, α is the mixture thermal diffusion coefficient. S^0_{flame} is the laminar flame speed for an unstrained flame ($Ka = \kappa = 0$). The laminar flame speed is defined as the flame axial velocity at the edge of the thermal diffusion zone, as shown in Figure 1.2.

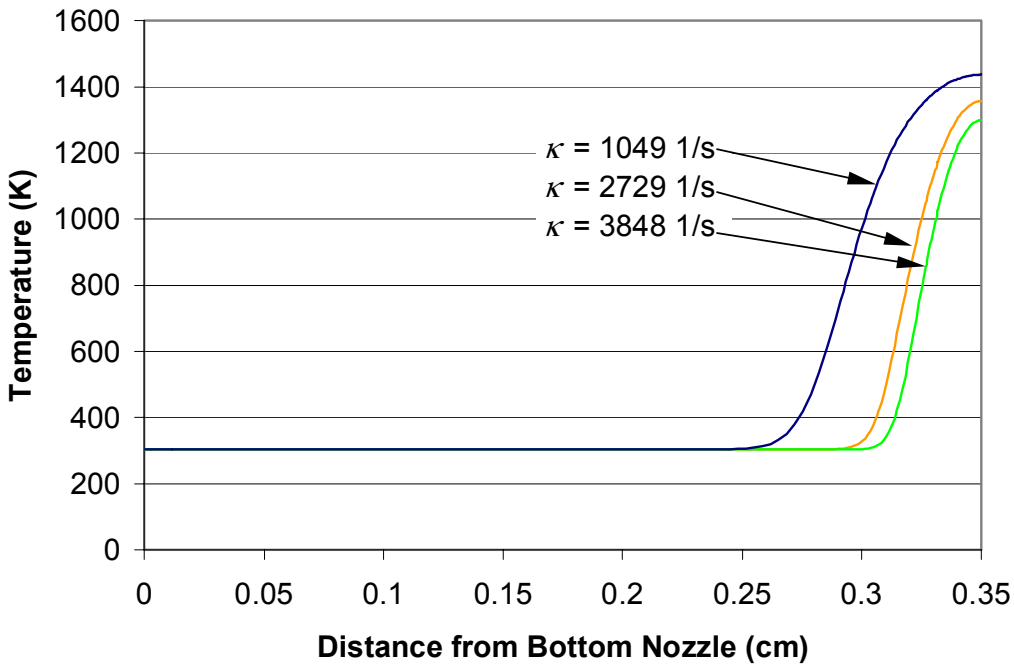

Figure 1.4: Temperature profiles for three strain rates for a H_2-air flame with $\phi = 0.28$.

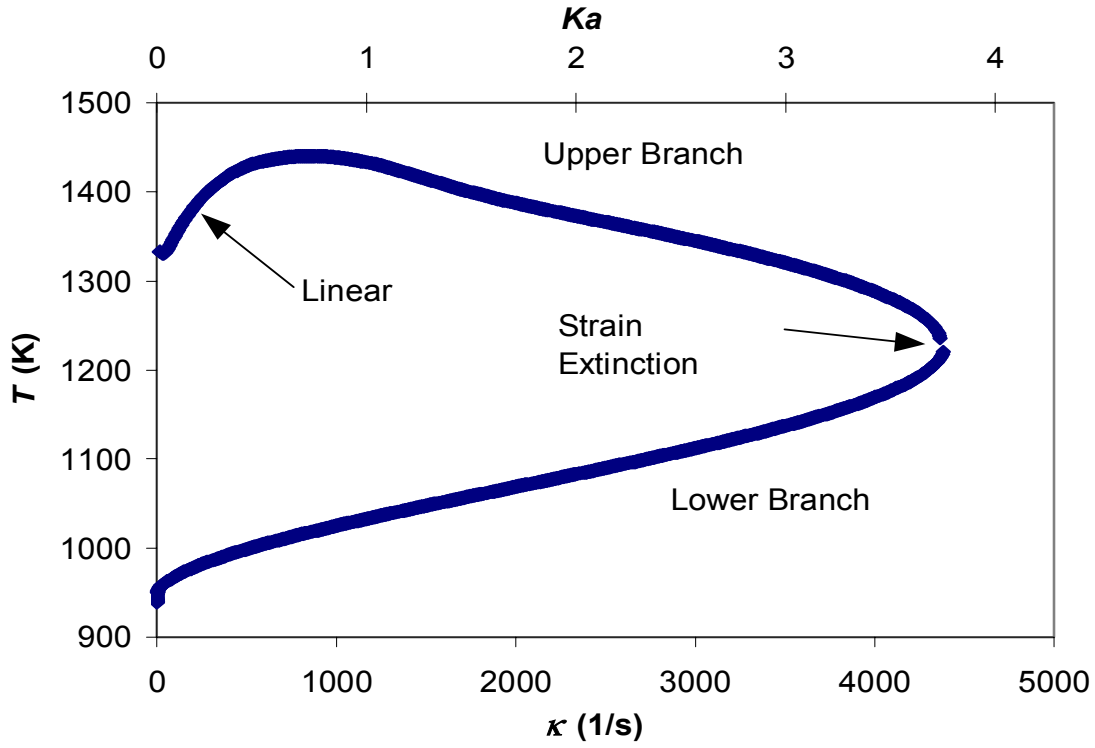

Figure 1.5: Maximum flame temperature as a function of strain rate for H_2-air flame with $\phi = 0.28$, $Le_{H2} = 0.34$ and $S^0_{flame} = 19$cm/s.

1.2.4 Transient counterflow studies

Steady state codes and models provide a good understanding of the relationship between the steady state global flame properties and the properties of the flow field and fuel stream. However, most real systems even when designed for steady state operation are subject to oscillations. Time varying strain rates are imposed on flames during the combustion stroke of an internal combustion engine. Turbulence during combustion also imposes varying strain with the amplitude of the oscillations proportional to the mean flow rate. Furthermore, gas turbines may experience oscillations due to interactions between the combustion and the flow conditions. Dominant excitations are often observed in gas turbine combustors in the low 100Hz range, precisely where hydrocarbon flames begin to show complex responses to oscillations [9, 19]. Investigations into transient combustion phenomena are needed to study the impact of transient conditions on laminar flames.

The results from dynamic flame models and experiments are beginning the development of a richer understanding of transient laminar flamelet behavior when subject to flow field oscillations [31]. Transient counterflow conditions have been investigated using both experimental and numerical techniques. A few studies have examined small perturbations to develop linearized transfer functions to be used in linear control models for combustion systems such as gas turbines [33]. Experimental studies have used speakers, either in-line with or normal to the flow, to impose oscillations on the flame [34, 35]. Computational models have also been developed to compute transient flame conditions. These numerical studies have included imposed oscillations on velocities [17, 19, 36, 37], the fuel equivalence ratio ϕ [9], and pressure [38].

In general, the transient investigations have shown that for small excitations at low frequencies (typically < 100Hz), premixed flames respond rapidly enough to maintain their quasi-steady structure and temperature for an instantaneous upstream condition. At very high frequencies (> 1000Hz or more), the flame behaves more like a low pass filter such that small excitations do not have a significant impact upon the instantaneous flame structure or temperature[36]. Flame behavior at high frequencies even becomes independent of *Le* [39].

Furthermore, results have indicated that extinction behavior is complicated by transient conditions. At intermediate (order of 100Hz) as well as higher frequencies, modeling has indicated that flames may persist even when oscillations force flame conditions temporarily beyond steady state extinction strain rates. However, a recent study suggested that the average conditions must remain within the steady-state flammability limits (in terms of flame temperature, and strain rate) for the flame to exist under oscillatory upstream conditions [9]. An experimental study also indicated that the local mean strain rate must not exceed a critical value, which is a function of ϕ, to avoid complete extinction [30].

A recent study looked at the species response to imposed transients for flames far from extinction limits. The results led to the proposal that the scalar dissipation, similar to turbulent non-premixed flames, is a better parameter than strain rate to characterize unsteady flame behavior. Furthermore, CO and NO_x concentrations were unaffected by the oscillations due to their relatively slow time scales [15].

An investigation into the effects of oscillations in equivalence ratio on the extinction limits of near extinction flames has also been conducted [9]. The fuel

equivalence ratio was varied over a sine wave starting at an initial condition near the lean extinction limit for that reactant composition. It was found that the oscillating conditions allowed the combustion to persist even though the oscillations pushed the equivalence ratio beyond the steady state extinction limit. It was concluded that the mean equivalence ratio must remain above the extinction limit to keep the flame from extinguishing. The results also showed that there may be a cut-off frequency above which the flame is unaffected by the oscillations.

The investigations mentioned above have helped improved the understanding of premixed, laminar flames. However, there are still many questions that remain unanswered. The research presented in this thesis will attempt to further the understanding of premixed, multicomponent laminar flames.

1.3 Objectives and Methods

Analytical models will be used to investigate the effects of strain and diffusion on a planar, counterflow flame. An integral, or control volume, method uses a simplified model of the counterflow domain to develop an expression for the flame temperature. The resulting analytical model can be used to predict the flame temperature as a function of fuel and flow field properties. This model will be tested to determine if it is possible to capture the overall effects of multiple fuel species using such a simplified modeling approach. Furthermore, if the model does work, the behavior of the flame as a function of the diffusion properties for multicomponent fuels can be investigated. Reactant compositions used for this investigation will be lean mixtures of CH_4, C_3H_8, H_2 and air with overall equivalence ratios of $\phi = 0.5$ and 0.75. The experimental and numerical investigations will focus on mixtures of CH_4/H_2-air.

The experimental and computational approaches parallel each other, allowing comparisons of the results. Both approaches are based on the counterflow flame configuration as shown in Figure 1.1. The computational domain extends from one nozzle exit plane to the opposite exit plane. The axial velocity U_{in} is the velocity exiting each nozzle and the separation distance is measured along the x-axis located along the nozzle centerline. Oscillations in velocity, and corresponding pressure oscillations, are imposed at the nozzle exit plane boundary conditions.

The model and experiments both determine the maximum relative oscillation amplitude the flame can withstand without extinguishing. Oscillations of different frequencies are used to determine the combustion response as a function of frequency. The addition of H_2, which increases the steady state extinction limits for a given fuel mixture, is also investigated to determine if benefits are realized in the transient case. For these tests, lean reactant compositions of CH_4 and H_2 mixed with air are used with mixture equivalence ratios of 0.5 and 0.75.

The computational analysis includes detailed chemical mechanisms, thermodynamics and molecular transport models. In addition to computing the extinction amplitudes for comparison to the experimental results, the computer model can investigate the behavior of the oscillating flame with respect to pollutant formation, flame temperature, and combustion efficiency.

The transient experiments use acoustic speakers to generate the pressure and velocity oscillations. The amplitude of the oscillations are recorded to determine the extinction amplitude for a given fuel composition and oscillation frequency. Also, the variation in velocity profile during a time-averaged cycle of oscillation is measured using

non-intrusive Laser Doppler Anemometry. The velocity profiles are used to validate the flame responses as determined with the computational results. Furthermore, the measured velocity profiles are used to help deduce the controlling mechanisms behind the flame response to forced oscillations.

The results of this investigation will improve the current state of combustion knowledge in several ways. First, current analytical analyses have only looked at single component fuels. The analysis here will allow quick determination of the effects of strain on fuel mixtures. Furthermore, the benefits of H_2 on steady state combustion have been demonstrated, but the effects of H_2 addition under transient conditions have not yet been investigated. This study will lead to improved understanding of the effects of H_2 addition.

Chapter 2 Steady State Analysis Methods

2.1 Introduction

Simplified analytical models can often provide insight into complex phenomena by revealing the controlling parameters. An integral analysis, often used in the areas of heat and mass transfer [14], has been used in this investigation to generate simple analytical models of premixed combustion. The analysis can include simplified reaction models to develop an analytical representation of a premixed flame and its surrounding flow field. For a counterflow premixed flame, the integral method can provide a representation of the behavior of the flame with respect to properties such as strain rate, reactant temperatures and mixture *Le*.

Previous integral analyses have focused on premixed streams of only single-component fuel. The fuel-oxidizer mixture is thus characterized by a single *Le* for the deficient reactant, either the fuel or the oxidizer. In mixtures with more than one fuel, it is not clear which fuel component's Le_k is the dominant value or if the *Le* effect is proportional to some combination of each species Le_k. Furthermore, multi-component flame behavior may occur with single-component fuels due to reactions occurring early in the pre-heat zone which may change the dominant fuel species and therefore change the effective *Le* in the flame zone [14]. This chapter explores the multi-component fuel effects on premixed flame structure through the development of an integral analysis to predict the global property of flame temperature for flames of multi-component fuels.

Two integral analyses are presented below for a planar flame exposed to pure stretch effects with no curvature. Both analyses assume relatively small amounts of strain such that the perturbation of the flame from the unstrained condition is still in the

linear region where flame properties vary linearly with the strain rate κ. The analysis is only applicable to low strain rates with $Ka << 1.0$ ($Ka \leq 0.2$). The combustion reactions of each fuel species are modeled as one-step reactions with an activation energy. The first integral analysis assumes that each fuel species is consumed in one lumped, overlapping flame zone. The second analysis assumes that there are discrete flame zones for each fuel species and is thus significantly more complicated than the single reaction zone analysis. These two conceptual flame models bound the possible structure of the multi-component flame. The physical flame likely lies somewhere between these two extremes. The analyses will provide a relation for flame temperature, T_{flame}, as a function of non-dimensional strain, Ka, initial temperature, T_0, and each fuel component's heat of combustion, q_k and Le_k.

A steady state computational model is also presented below. The computational model is used to compute flame temperature versus strain using detailed chemical kinetics, thermodynamics and species diffusion. The computational results are assumed the standard solution for evaluating the accuracy of the integral analyses. Results from the literature for single component fuels will also be used for comparisons of predictions of flame temperature, T_{flame}, versus imposed strain.

2.2 Integral Analysis Derivation

2.2.1 Single flame model

Two different integral analyses will be developed and investigated for their ability to predict combustion temperature. Both formulations start from the same set of initial equations [14]:

conservation of mass,

$$\frac{d(\rho u A)}{dx} = 0\,, \tag{2.1}$$

conservation of energy,

$$\left(A\rho u c_p T\right) - \left(A\lambda \frac{dT}{dx}\right) = \sum_k \left(\int A q_k B_k E_k Y_k dx\right) \tag{2.2}$$

and conservation of species.

$$\left(A\rho u Y_k\right) - \left(A\rho D_k \frac{dY_k}{dx}\right) = \int - A B_k Y_k E_k dx \tag{2.3}$$

In these equations A is the cross sectional flow area, ρ the density, u the flow velocity, c_p the specific heat, T the temperature, and λ the conductivity, q_k the heat of combustion of species 'k', B_k the effective frequency factor for the first order reaction for species 'k', E_k the exponential term of the first-order reaction for species 'k', Y_k the species mass fraction of species 'k', and D_k the species mass diffusivity of species 'k'. The energy equation sums the contributions of all k fuel species, while the species conservation equation is applied to each species individually.

The three equations are applied over a linearized counterflow combustion region. A schematic of the flame region is shown in Figure 2.1. The flow is assumed to move from left to right. The domain is divided into five regions. The flow begins in the upstream region unaffected by the flame where the gas temperature begins at the upstream temperature, T_0. In the thermal diffusion zone, ℓ_T, heat is diffused upstream. Mass diffusion takes place in the mass diffusion zone of length, ℓ_m. The relative lengths of the thermal and mass diffusion zones show that the $Le > 1.0$, since the thermal

diffusion is greater than the mass diffusion. The next zone is an infinitesimally thin reaction zone which is followed by the downstream burned region.

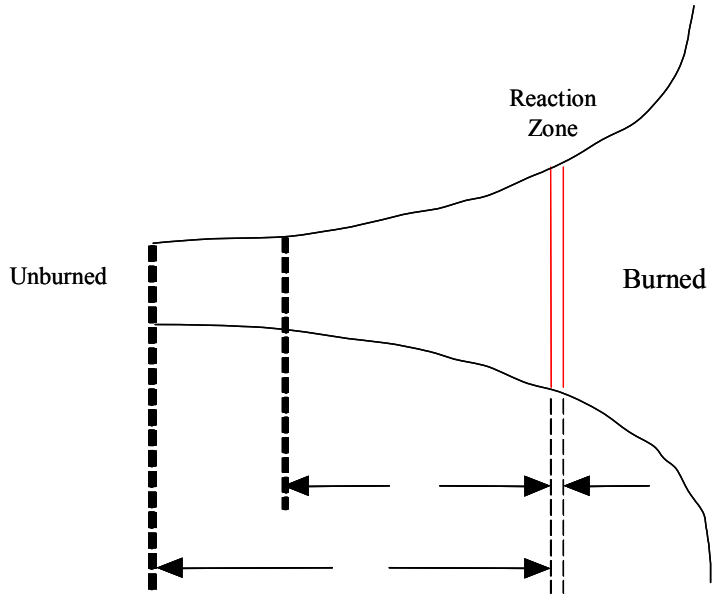

Figure 2.1: Schematic of the counterflow flame region for a single reactant species with a mixture $Le > 1.0$.

Figure 2.2 shows a plot of the linearized temperature and fuel species mass fraction profiles through the counterflow flame domain. The gas temperature increases the temperature from the initial temperature, T_0, to the flame temperature, T_{flame}, at the flame location. The species mass fractions begin at their upstream values of $Y_{k,u}$. The mass fractions decrease through their individual mass diffusion zones, $\ell_{m,k}$, as the species diffuse into the flame zone. The fuel species are assumed to have a zero mass fraction after the flame zone. For complete combustion at low strain rates this is a good assumption. Linear variations are assumed for both temperature and species mass fraction approaching the flame zone.

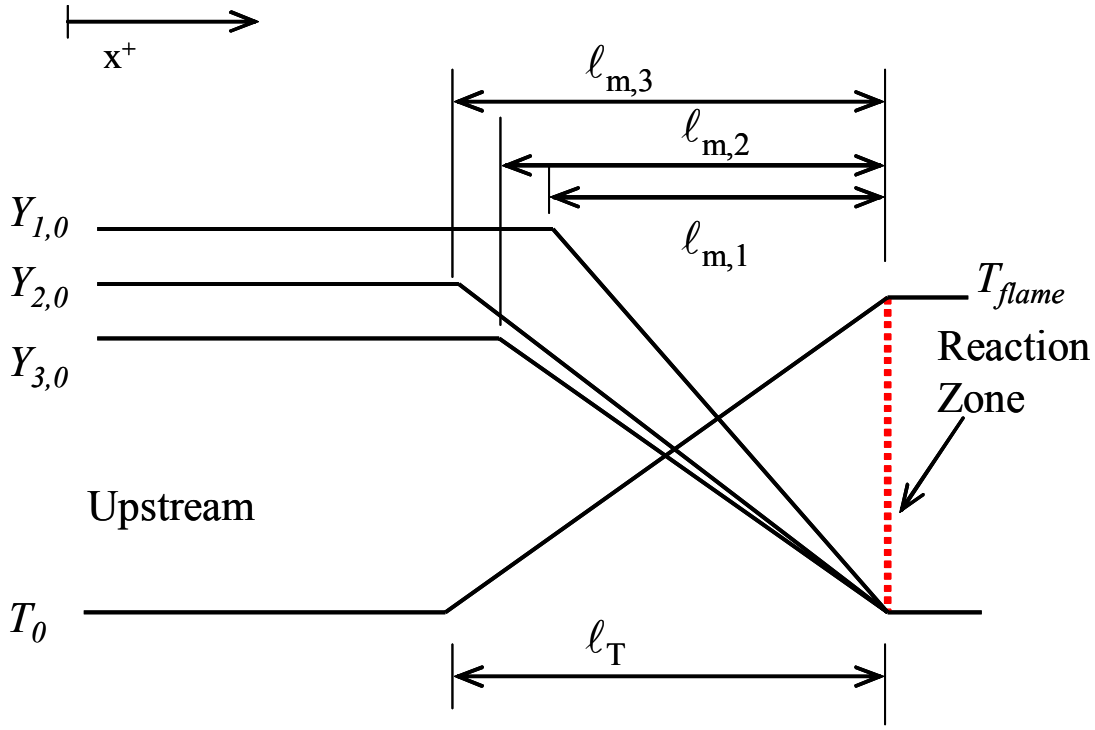

Figure 2.2: Schematic of a linearized counterflow strained flame for a mixture of multiple fuel species as modeled with a single combined reaction zone.

The conservation of mass equation (2.1) applied to the domain shows that the mass flow rate, $\dot{m}$, is constant,

$$\dot{m} = \rho u_0 A_0 , \tag{2.4}$$

where the subscript '0' refers to the upstream conditions.

Integrating equation (2.2) across the reaction zone gives

$$\dot{m} c_p \left(T_{x^+_{flame}} - T_{x^-_{flame}} \right) - \left(A \lambda \frac{dT}{dx} \right) \Bigg|_{x^-_{flame}}^{x^+_{flame}} = \sum_n \left(\int_{x^-_{flame}}^{x^+_{flame}} q_k B_k E_k Y_k dx \right). \tag{2.5}$$

The indices x^+_{flame} and x^-_{flame} refer to the downstream and upstream edges of the flame, respectively. With the assumption of a thin flame zone, and constant downstream temperature $T_{flame,}$ equation (2.5) simplifies to

$$\lambda \left.\frac{dT}{dx}\right|_{x_{flame}^-} = \sum_n \left(\int_{x_{flame}^-}^{x_{flame}^+} q_k B_k E_k Y_k dx \right). \tag{2.6}$$

Integrating equation (2.2) over the preheat region gives

$$\dot{m} c_p \left(T_{flame} - T_0\right) - A_0 \lambda \left(\left.\frac{dT}{dx}\right|_{x_{flame}^-} - \left.\frac{dT}{dx}\right|_{x_0} \right) = 0 . \tag{2.7}$$

The upstream area, A_0, is used in equation (2.7) because only heat conducted through A_0 heats the incoming flow. Equation (2.7) may be simplified to

$$\rho u c_p \left(T_{flame} - T_0\right) = \lambda \left.\frac{dT}{dx}\right|_{x_{flame}^-} . \tag{2.8}$$

Integrating species conservation, equation (2.3), over the flame zone for species k results in

$$\dot{m} \left(Y_{k,x_{flame}^+} - Y_{k,x_{flame}^-} \right) - A_{flame} \rho D_k \left(\left.\frac{dY_k}{dx}\right|_{x_{flame}^+} - \left.\frac{dY_k}{dx}\right|_{x_{flame}^-} \right) = -A_{flame} \int_{x_{flame}^-}^{x_{flame}^+} B_k Y_k E_k dx . \tag{2.9}$$

Assuming that the fuel has diffused into the flame zone from upstream so that the fuel mass fraction has reached zero at the flame zone, and that the gradient downstream of the flame is zero simplifies equation (2.9) to

$$\rho D_k \left.\frac{dY_k}{dx}\right|_{x_{flame}^-} = -\int_{x_{flame}^-}^{x_{flame}^+} B_k Y_k E_k dx . \tag{2.10}$$

Similar to the energy equation, integrating the species conservation over a mass diffusion zone for species n results in the following

$$\dot{m} \left(Y_{k,x_{flame}^-} - Y_{k,0} \right) - A_m \rho D_k \left(\left.\frac{dY_k}{dx}\right|_{x_{flame}^-} - \left.\frac{dY_k}{dx}\right|_{0} \right) = 0 , \tag{2.11}$$

which may be simplified to

$$\rho u_0 Y_{k,0} = -\frac{A_m}{A_0}\rho D_k \left.\frac{dY_k}{dx}\right|_{x_{flame}^-} . \tag{2.12}$$

Defining the mass diffusion length, $\ell_{m,k}$ for each of the fuel species and the combined thermal diffusion length, ℓ_T, as

$$\ell_{m,k} \equiv -Y_{k,0} \Big/ \left.\frac{dY_k}{dx}\right|_{x_{flame}^-} , \tag{2.13}$$

and

$$\ell_T \equiv \frac{\left(T_{flame} - T_0\right)}{\left.\frac{dT}{dx}\right|_{x_{flame}^-}} , \tag{2.14}$$

respectively, allows the simplification of equations (2.12) and (2.8) to

$$\rho u_0 \ell_{m,k} = \frac{A_{m,k}}{A_0}\rho D_k$$

$$\rho u_0 c_p \ell_T = \lambda . \tag{2.15}$$

Using equations (2.15), the Lewis number, Le_k, can then be defined for species k as

$$Le_k \frac{A_0}{A_m} = \frac{\ell_T}{\ell_{m,k}} . \tag{2.16}$$

Combining the assumption that the area changes are gradual and linearly similar,

$$\frac{A_{flame} - A_0}{\ell_T} = \frac{A_{flame} - A_{m,k}}{\ell_{m,k}} , \tag{2.17}$$

along with equation (2.16) and the non-dimensional strain Karlovitz number,

$$Ka = \frac{A_{flame} - A_0}{A_0} , \tag{2.18}$$

yields

$$\frac{A_0}{A_{m,k}} = Ka\left(\frac{1}{Le_k} - 1\right) + 1 . \tag{2.19}$$

The *Ka* defined in equation (2.18) is a non-dimensional strain rate and is a representation of the amount the flame is stretched in the counterflow flow field. If $Ka = 0$, then the area at the flame is the same as the upstream area and the flame is exposed to zero stretched.

Adding equation (2.6) with equation (2.10) multiplied by q_k, eliminates the integral and gives

$$\lambda \left.\frac{dT}{dx}\right|_{x_{flame}^-} = \sum_{k=1}^{K} q_k \rho D_k \left.\frac{dY_k}{dx}\right|_{x_{flame}^-} . \tag{2.20}$$

The above relations may be used to simplify equation (2.20) to

$$\left(T_{flame} - T_0\right) = \sum_{k=1}^{K}\left(\frac{q_k Y_k}{c_p}\left(Ka\left(\frac{1}{Le_k} - 1\right) + 1\right)\right), \tag{2.21}$$

Equation (2.21) shows that the flame temperature may be affected by strain only when some Le_k does not equal 1.0. Furthermore, if the flame is not strained, $Ka = 0$, the Le_k of the fuel species has no effect on the flame temperature. For a flame with either $Ka = 0$ or $Le_k = 1.0$, the change in temperature from burned to unburned is the adiabatic flame temperature,

$$T_{flame} - T_0 = \Delta T^0 = \sum_{k=1}^{K} \frac{q_k Y_k}{c_p}, \tag{2.22}$$

where the superscript '0' indicates the unstrained condition.

Finally, with equation (2.22) an effective *Le*, Le_{eff}, of the multi-component fuel may be defined, and this definition would account for the non-equidiffusive properties of the mixture of fuel species. By defining

$$\frac{1}{Le_{eff}} = \sum_{k=1}^{K} \frac{\hat{q}_k}{Le_k}, \tag{2.23}$$

where

$$\hat{q}_k = \frac{q_k Y_{k,0}}{\sum_{k=1}^{K} q_k Y_{k,0}}, \tag{2.24}$$

equation (2.21) may then be simplified to

$$T_{flame} = T_0 + \Delta T^0 \left(Ka \left(\frac{1}{Le_{eff}} - 1 \right) + 1 \right). \tag{2.25}$$

The final relation, equation (2.25), relates the flame temperature to the adiabatic, unstrained flame temperature, the flow strain, and the combined *Le* effects of all the fuel species. Results for Le_{eff} for several mixtures will be shown in the following chapter.

2.2.2 Discrete reaction zone model

The above derivation was based on the assumption that the flame consists of a single flame zone in which all the fuel species are consumed. A second possibility is that the individual fuel species are consumed in discrete flames, one for each species, each with a finite separation distance. Each flame has an associated reaction zone, mass diffusion zone and thermal diffusion zone. A schematic of this concept is shown in Figure 2.3.

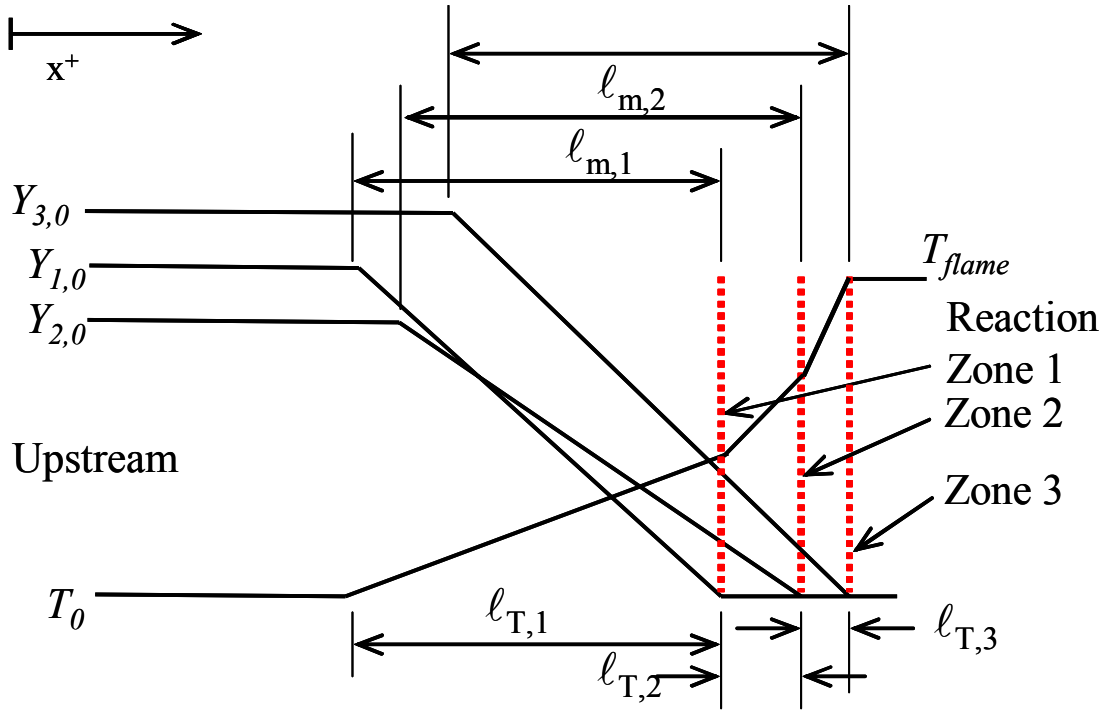

Figure 2.3: Schematic of a linearized counterflow strained flame for a mixture of multiple fuel species as modeled with discrete reaction zones for each species.

The two conceptual flame constructs discussed in this chapter bound the possible structure a physical flame. The derivation for the flame temperature relation for the assumption shown in Figure 2.3 is similar to the preceding derivation.

In this derivation, each fuel species is associated with an individual thermal diffusion zone, mass diffusion zone and reaction zone. Therefore, the single subscript *n* may be used to refer to the all the zones associated with species *n*. The conservation of energy, equation (2.2), is integrated over the reaction zone and the thermal diffusion zone associated with a single fuel species *n*, giving

$$-A_n\lambda\left(\left.\frac{dT}{dx}\right|_{n^+}-\left.\frac{dT}{dx}\right|_{n^-}\right)=B_nA_nq_n\int_{n^-}^{n^+}Y_nE_ndx\,, \tag{2.25}$$

and

$$A_0 \rho u_0 c_p (T_n - T_{n-1}) - \lambda A_{n-1} \left(\left. \frac{dT}{dx} \right|_{n^+} - \left. \frac{dT}{dx} \right|_{n-1^+} \right) = 0 , \tag{2.26}$$

where A_n is the area at reaction zone n for species n. The species conservation equation (2.3) is also integrated over the reaction region and the mass diffusion region to give

$$D_n \rho \left. \frac{dY_n}{dx} \right|_{n^-} = -B_n \int_{n^-}^{n^+} Y_n E_n dx , \tag{2.27}$$

and

$$\rho u_0 Y_{n,0} = -\frac{A_{m,n}}{A_0} D_n \rho \left. \frac{dY_n}{dx} \right|_{n^-} , \tag{2.28}$$

where $A_{m,n}$ is the area at the upstream boundary of the mass diffusion zone for species n. The thermal and mass diffusion lengths are defined as

$$\ell_{T,n} \equiv \frac{(T_n - T_{n-1})}{\left(\left. \frac{dT}{dx} \right|_{n^-} - \left. \frac{dT}{dx} \right|_{n-1^+} \right)} \tag{2.29}$$

$$\ell_{k,n} \equiv -Y_{k,n,0} \Big/ \left. \frac{dY_{k,n}}{dx} \right|_{n^-} . \tag{2.30}$$

It should be noted that the temperature gradient downstream of the last flame, $dT/dx|_{n^+}$, is zero. Using equations (2.29) and (2.30) with equations (2.26) and (2.28) gives

$$\rho u_0 c_p \ell_{T,n} = \lambda \frac{A_{n-1}}{A_0} \tag{2.31}$$

and

$$\rho u_0 \ell_{m,n} = \frac{A_{m,n}}{A_0} \rho D_n . \tag{2.32}$$

Equations (2.25) and (2.27) may be combined to yield

$$\lambda\left(\left.\frac{dT}{dx}\right|_{n^+} - \left.\frac{dT}{dx}\right|_{n^-}\right) = D_n \rho q_n \left.\frac{dY_n}{dx}\right|_{n^-}. \tag{2.33}$$

Summing equation (2.33) over all N reaction zones gives an equation for the entire composite flame. The summed equation, with the temperature derivatives reordered, is given as

$$-\lambda\left[\left.\frac{dT}{dx}\right|_{N^+} + \left(\left.\frac{dT}{dx}\right|_{N^-} - \left.\frac{dT}{dx}\right|_{N-1^+}\right) + \cdots + \left(\left.\frac{dT}{dx}\right|_{1^-} - \left.\frac{dT}{dx}\right|_{0^+}\right)\right] = \sum_{n=1}^{N} D_n \rho q_n \left.\frac{dY_n}{dx}\right|_{n^-}. \tag{2.34}$$

In the above equation, the first derivative on the left-hand-side is zero because there is no temperature gradient after the last reaction zone. Also, the last derivative on the left can be ignored because the temperature gradient in the upstream region, region '0', is zero by definition. Equation (2.34) may be simplified by with equations (2.31) and (2.32) to

$$\sum_{n=1}^{N}\left((T_n - T_{n-1})c_p \frac{A_0}{A_{n-1}} - q_n Y_{n,0}\frac{A_0}{A_n}\right) = 0. \tag{2.35}$$

To solve for the area ratios, a few assumptions must be made. First, it is assumed that the Karlovitz number, *Ka,* is defined as in equation (2.18). Next, the flame cross sectional areas are related by the heat release associated with each flame,

$$\frac{A_n - A_0}{A_N - A_0} = \frac{\sum_{i=1}^{n} q_i Y_{i,0}}{\sum_{n=1}^{N} q_n Y_{n,0}} = \frac{Q_n}{\hat{Q}}, \tag{2.36}$$

which allows the flame cross sectional areas to be related to the *Ka* by

$$\frac{A_n - A_0}{A_0} = Ka\frac{Q_n}{\hat{Q}}. \tag{2.37}$$

Similar to equation (2.17), the thermal and mass diffusion lengths may be related through the following

$$\frac{A_n - A_0}{\sum_{i=1}^{n} \ell_{T,i}} = \frac{A_n - A_{m,n}}{\ell_{m,n}}. \tag{2.38}$$

As can be seen in Figure 2.3, the first thermal diffusion length is much larger than the others,

$$\ell_{T,1} >> \ell_{T,2}, \ldots, \ell_{T,N}. \tag{2.39}$$

Therefore, equation (2.38) may be simplified to

$$\frac{A_0}{A_n} = Ka \frac{Q_n}{\hat{Q}} \left(\frac{1}{Le_n} - 1 \right) + 1. \tag{2.40}$$

Using the area ratios, equation (2.35) becomes

$$\sum_{n=1}^{N} \left(\left(T_n - T_{n-1} \right) \left(1 - Ka \frac{Q_{n-1}}{\hat{Q}} \right) - \frac{q_n Y_{n,0}}{c_p} \left(Ka \frac{Q_n}{\hat{Q}} \left(\frac{1}{Le_n} - 1 \right) + 1 \right) \right) = 0 \tag{2.41}$$

Equation (2.42) is one equation with each reaction zone temperature, T_1 to T_N, as unknowns. The final reaction zone temperature, T_N, is the overall flame temperature, T_{flame}. An additional relation is needed to compare the unknown temperatures. A final assumption is made to relate the flame temperatures through a ratio of the flame heat release,

$$\frac{T_n - T_0}{T_{flame} - T_0} = \frac{Q_n}{\hat{Q}}. \tag{2.42}$$

Together, equations (2.41) and (2.42) can be used to determine the flame temperature for multi-component, non-equidiffusive flames subjected to moderate strain rates.

2.3 Numerical Analysis Method

A numerical code was written to model a steady state counterflow flame. The code, CFPWHOLE, modeled the entire counterflow region from one nozzle to opposite.

The numerical formulation was based on work in the literature [20, 37] and was a steady state version of the equation set used for the transient combustion code discussed later. Modifications to the original equation set made it less stiff and therefore more readily solved [15]. These steady state equations were solved using the numerical code TWOPNT [40], which uses a combination of a conjugate gradient method and time stepping to arrive at the steady state solution. A series of steady state solutions can be obtained using each previous solution as an initial guess and incrementally changing the axial velocity by a small delta. This method is discussed more completely in later chapters describing the numerical modeling. This computational technique provides the variation in the steady state response of a counterflow flame to strain.

The analytical flame descriptions derived above attempt to quantify the affects of multiple fuels of different species on a strained flame. CFPWHOLE computes the flame properties using finite rate chemistry, multi-component diffusion and thermal diffusion based on the properties of the premixed flow and the imposed inlet conditions. The conservation equations solved in CFPWHOLE are composed of a steady state version of the transient conservation equations discussed in Chapter 4 for the transient code TREC. The equation set included conservation of mass, axial and radial momentum, energy and species and includes species diffusion velocities and species generation. The chemical reaction, thermodynamic and molecular diffusion effects were included through the use of GRI-Mech v3.0 [41] described in Chapter 4. The numerical solution technique has been validated through previous studies [1, 2, 12]. Therefore, if the analytical models predict flame temperature variations that match the numerical results, the analytical

models may be assumed to have correctly captured the effects of strain on a strained, multi-component, non-equidiffusive fuel-oxidizer mixture.

2.4 Definition of Inlet Composition

All the flames in this study are lean fuel-air mixtures, $\phi < 1.0$. The composition of the lean CH_4-air mixture is determined from the following chemical equation.

$$(1-\alpha)CH_4 + 4\alpha H_2 + \frac{2}{\phi}\left(O_2 + \frac{79}{21}N_2\right) \Rightarrow (1-\alpha)CO_2 + (2+2\alpha)H_2O + \frac{2}{\phi}\left((1-\phi)O_2 + \frac{79}{21}N_2\right) \quad \text{(R2.1)}$$

In the above global reaction, ϕ is the equivalence ratio. The variable α determines how much H_2 is to be added to be mixture, and represents the ratio of O_2 consumed by H_2 to the total amount of O_2 consumed in the reaction. If $\alpha = 1.0$, then all the O_2 is consumed by H_2 and there is no CH_4 in the fuel mixture. Conversely, if $\alpha = 0.0$ there is no H_2 in the mixture. Only a small amount of H_2 is required to affect large changes in flame behavior due to its high mass diffusivity and reaction rates. However, the replacement of CH_4 with H_2 does not greatly change the total heat release of the fuel mixture. Reaction (R2.1) shows that it requires four moles of H_2 to replace one mole of CH_4. The heat release for CH_4 is about 3.5 times less than the heat release for H_2. Therefore for small additions of H_2, the overall adiabatic flame temperature is not greatly changed. The mixtures used in this study have and equivalence ratio of $\phi = 0.0$, 0.05, or 0.10 and $\alpha =$ 0.0, 0.05, or 0.10.

CH_4 has a *Le* slightly less than one for the reactant compositions discussed here. Using lean C_3H_8-air flames provides a reactant mixture in which the deficient species, the C_3H_8, has a $Le > 1.0$. Reactant mixtures with $Le > 1.0$ behave differently than mixtures

with $Le < 1.0$. The analytical relations developed above will be tested to determine if they can capture T_{flame} versus imposed strain for $Le > 1.0$ as well. The following reaction was used to determine mixture compositions used in this investigation.

$$(1-\alpha)C_3H_8 + 10\alpha H_2 + \frac{5}{\phi}\left(O_2 + \frac{79}{21}N_2\right) \Rightarrow 3(1-\alpha)CO_2 + (4+6\alpha)H_2O + \frac{5}{\phi}\left((1-\phi)O_2 + \frac{79}{21}N_2\right) \quad \text{(R2.2)}$$

In reaction (R2.2), α represents the fraction of O_2 consumed by H_2 to the total amount of O_2 consumed in the reaction.

2.5 Conclusions

This chapter presented the derivations of two analytical representations of T_{flame} for premixed flames of multiple fuel species exposed to low strain. The relations predict T_{flame} as a function of mixture composition, Le_k, an imposed strain. Integral methods were used to derive the equations. One derivation was based on the assumption of a single reaction zone for all species and multiple mass diffusion zones. The second derivation assumed discrete reaction zones and associated thermal and mass diffusion zones for each fuel species.

The analytical relations will be examined in the following chapter by comparing the analytical predictions of T_{flame} to numerical T_{flame} calculations from a detailed computational code. The code evaluates multi-component diffusion and full chemical kinetics to provide an accurate T_{flame} for a given mixture composition and strain rate. The results of the comparison will indicate if the simple analytical relations derived here can adequately capture the effects of strain and diffusion on flame temperature.

Chapter 3 Steady State Analysis Results

3.1 Introduction

The analytical relations derived in the previous chapter relating flame temperature response to imposed strain for positively stretched flames are studied here. The major advantages of the integral analyses are their simplicity. The flame behavior with respect to several properties may be easily determined from the relations, providing valuable insight in interpreting experimental results and full numerical analysis with complex chemistry models. Integral analysis, as described in Chapter 2, is used to assess changes in flame behavior with respect to *Le*, *Ka*, and fuel composition for a linearized flame subject to low positive strain with $Ka << 1.0$ [14]. As strain, and *Ka*, increases the linear assumptions become less accurate. In this chapter, results from the derived integral analyses are compared to computational results for counterflow, premixed, one-dimensional flames. The computational results are obtained using the computational code CFPWHOLE, which models a one-dimensional, counterflow flame using detailed chemistry with GRI-Mech v.3.0 [41] and is described in Chapter 4. The variation in the flame temperature with respect to *Le* and *Ka* is examined.

All the fuel-air mixtures modeled with the integral equations are listed in Table 3.1. The fuel species are listed with their mass fractions at the inlet. The variables ϕ and α are the equivalence ratio and fraction of H_2.

Table 3.1: Definition of the reactant composition of all the fuel-air mixtures studied with the integral analysis including fuel species mass fractions and Le_k.

Mixture	**I**	**II**	**III**	**IV**	**V**
ϕ	0.50	0.50	0.75	0.75	0.75
α	0.00	0.10	0.00	0.00	0.10
Y_{C3H8} Le_{C3H8}	0.00	0.00	0.00	0.0459 1.74	0.0414 1.88
Y_{CH4} Le_{CH4}	0.0284 0.95	0.0256 1.00	0.0420 0.94	0.00	0.00
Y_{H2} Le_{H2}	0.00	0.0014 0.30	0.00	0.00	0.0021 0.29
S^0_{flame}	20 cm/s	35 cm/s	50 cm/s	80 cm/s	100 cm/s

3.2 Single Reactant Flames

3.2.1 Le effects

Both flame temperature relations derived in the previous chapter, equations (2.21) and (2.41), when applied to reactant mixtures with a single fuel species, reduce to the same equation. Therefore, using either relation provides the same predicted flame temperature for a single fuel species mixture and only one relation will be examined in this section. Furthermore, the simplified equation matches a simple relation in the literature specifically derived for single species reactants [42].

The response of the flame temperature prediction to *Le* variations can be deduced from an examination of equation (2.21), which includes *Le* and *Ka*, where *Ka* is the Karlovitz number or the dimensionless strain rate. Rewriting equation (2.21), the following relation is obtained

$$T_{flame} - T_0 = \frac{q_k Y_{k,0}}{c_p}\left(Ka\left(\frac{1}{Le_k} - 1 \right) + 1 \right). \tag{3.1}$$

where c_p is an average specific heat and Le_k is for the limiting reactant which in lean flames is always the fuel. Equation 3.1 states that $T_{flame} - T_0$ is proportional to the imposed strain rate κ since $Ka \propto \kappa$. Figure 3.1 is a plot of the dimensionless temperature rise $\frac{c_p\left(T_{flame} - T_0\right)}{q_k Y_{k,0}}$ using equation (3.1) with Le = 0.6, 0.8, 1.0, 1.2 and 1.4. The term $\frac{q_k Y_{k,0}}{c_p}$ is the temperature rise under zero strain (when Ka = 0).

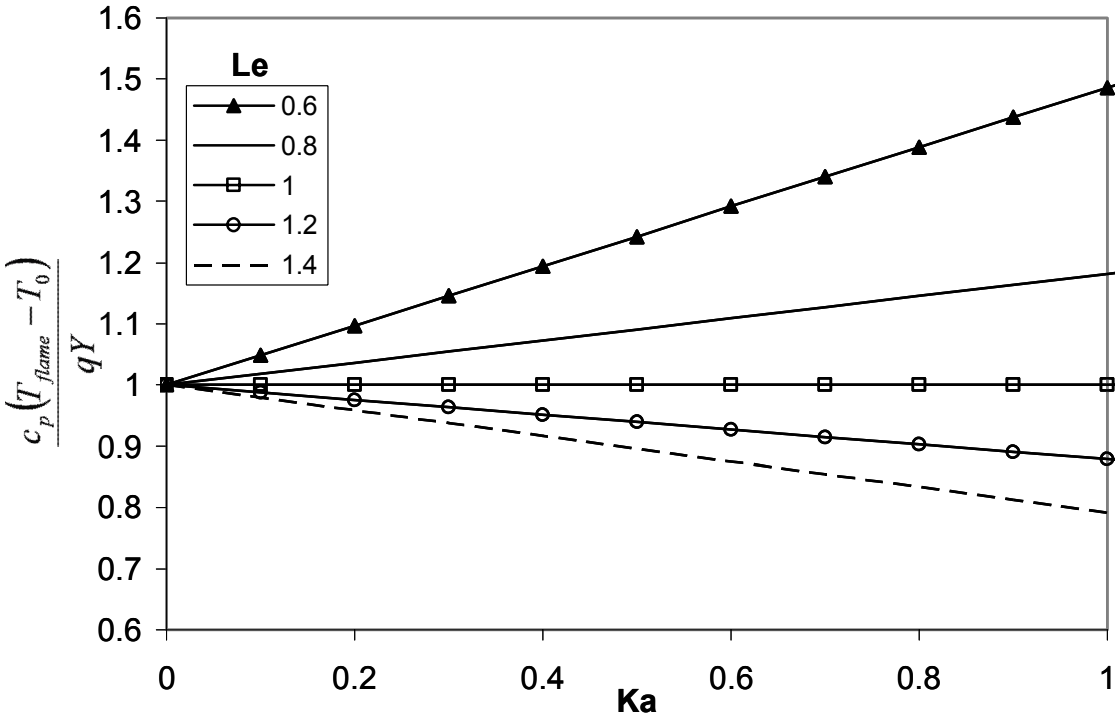

Figure 3.1: Non-dimensional temperature increase computed using integral relation for a lean flame with a single fuel species for several values of Le.

It can be seen in the figure that for a lean flame with Le = 1.0, the flame temperature is unaffected by the imposed strain. For this reactant composition, the thermal and mass diffusion of the fuel species are equal and strain can not impose non-

equidiffusive effects. When Le is not equal to 1.0, imposed strain and the associated flow field stretch affect the flame. When $Le < 1.0$ for a lean flame, the fuel species diffuses into the flame zone ahead of the bulk flow, enriching the flame and increasing T_{flame}. When $Le > 1.0$, air diffuses into the flame zone, making the flame leaner and decreasing T_{flame}. Plotting the dimensionless temperature in this manner also shows that the slope of the T_{flame} versus Ka lines increase with decreasing Le faster than they decrease with increasing Le. The integral analysis predicts that T_{flame} is more sensitive to $Le < 1.0$ than to $Le > 1.0$.

3.2.2 Comparison to numerical results

The computational results are obtained from the steady state, counterflow flame code CFPWHOLE. CFPWHOLE uses detailed chemical kinetics and multi-component species diffusion to model the one dimensional domain along the centerline between the two counterflow nozzles. Gas phase chemical kinetics and species diffusion velocities were evaluated using CHEMKIN [26, 27]. Several chemical mechanisms were used to model the chemical kinetics. The full kinetic mechanism GRI-Mech v3.0 [41] for methane-air combustion was used for this steady state analysis. GRI-Mech is a chemical reaction mechanism for natural gas combustion that may also be used for mixtures with significant C_3H_8. GRI-Mech contains 53 chemical species and 214 individual chemical reactions. Using the mechanism requires solving for each species mass fraction as well as the pressure, velocities, eigenvalue and gas temperature at each computational cell. Additionally, each of the chemical reactions must be solved to compute the species generation rates. The large computational effort to solve these chemical equations is the reason the computational domain is limited to a one-dimensional domain.

The *Ka* for the numerical results was determined by scaling the strain rate using the computational flame thickness, S_L, and flame speed at zero strain, S^0_{flame}, as done in previous studies [1]. The flame speed was scaled from previously reported results [43] and S_L was defined as

$$S_L = \alpha / S^0_{flame} \quad . \tag{3.2}$$

The analytical $T_{flame} - T_0$ at $Ka = 0$ was scaled to match the computational T_{flame} by reducing the heat of combustion for CH_4 by about 25%. The mixture properties used in the analytical equations, c_p, Le_k, were obtained from the initial conditions in CFPWHOLE.

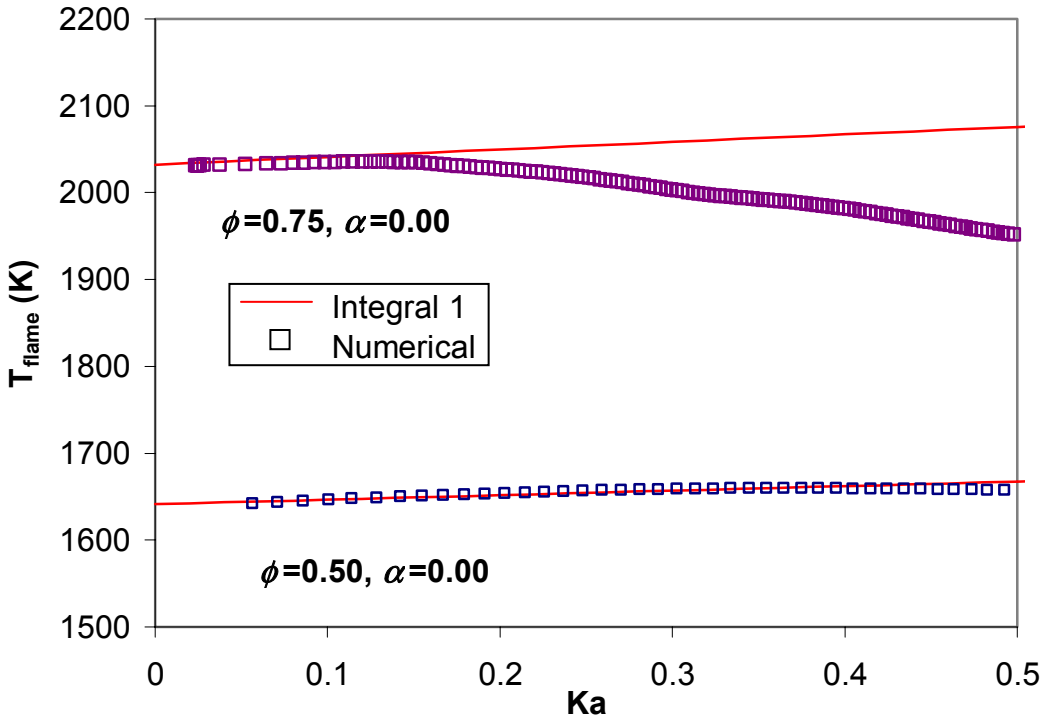

Figure 3.2: Computational and analytical predictions of T_{flame} for CH_4/air mixtures of ϕ = 0.75 and 0.50 (mixtures I and III).

Figure 3.2 is a plot of T_{flame} predictions from both numerical and integral analysis results for a CH_4-air flame with $\phi = 0.5$ and $\phi = 0.75$. It can be seen that at low strain the computational results show the flame temperature increases with increasing *Ka*. As *Ka* continues to increases, non-linear effects begin to dominate and T_{flame} begins to decrease. This occurs near *Ka* = 0.2 (κ= 716 1/s) for the $\phi = 0.75$ flame and near *Ka* = 0.4 (κ= 236 1/s) for the $\phi = 0.5$ flame. The linear integral analysis cannot capture the non-linear effects, and therefore predict a continual linear increase in T_{flame} with increasing *Ka*. For comparison, the extinction strain rates for the $\phi = 0.75$ and 0.5 flames are κ_{ext} = 4640 1/s and 1130 1/s, respectively. Therefore, the *Ka*'s above represent strain rates well below the extinction point.

In the region with T_{flame} increasing with *Ka*, the integral analysis results match the computational closely. T_{flame} increases approximately 52K and 92K per unit *Ka* for the ϕ = 0.5 and $\phi = 0.75$ cases, respectively. The larger slope for the $\phi = 0.75$ flame reflects the lower Le_{CH4} of 0.94 versus 0.95. This illustrates that a small difference in Le_k, when Le_k is close to 1.0, can have significant effect on the flame response to imposed strain.

3.3 Multiple Reactant Flames

As mentioned above, the two integral analysis developed in Chapter 2 reduce to the same relation for a reactant mixture with one fuel species. It is anticipated that the two relations will give different results for mixtures with more than one fuel. However, the relative contribution to the strain effects from each fuel species is ultimately scaled by the individual species mixture fraction. Therefore, using the relations to investigate the effects of *Le* on T_{flame} of a multi-component fuel mixture requires assumptions concerning

the composition of the mixture. Instead, a few real fuel mixtures are investigated to show these effects in the following sections.

3.3.1 CH_4, H_2 mixtures

Figure 3.3 is a plot of T_{flame} versus Ka for both analytical and computational results. The reactant mixtures were defined as mixtures with $\phi = 0.5$ and $\alpha = 0.0$ or 0.10. The Ka for the computational results are scaled from the computed κ as described above. The mixture properties used in the analytical analysis were determined from the computational initial conditions.

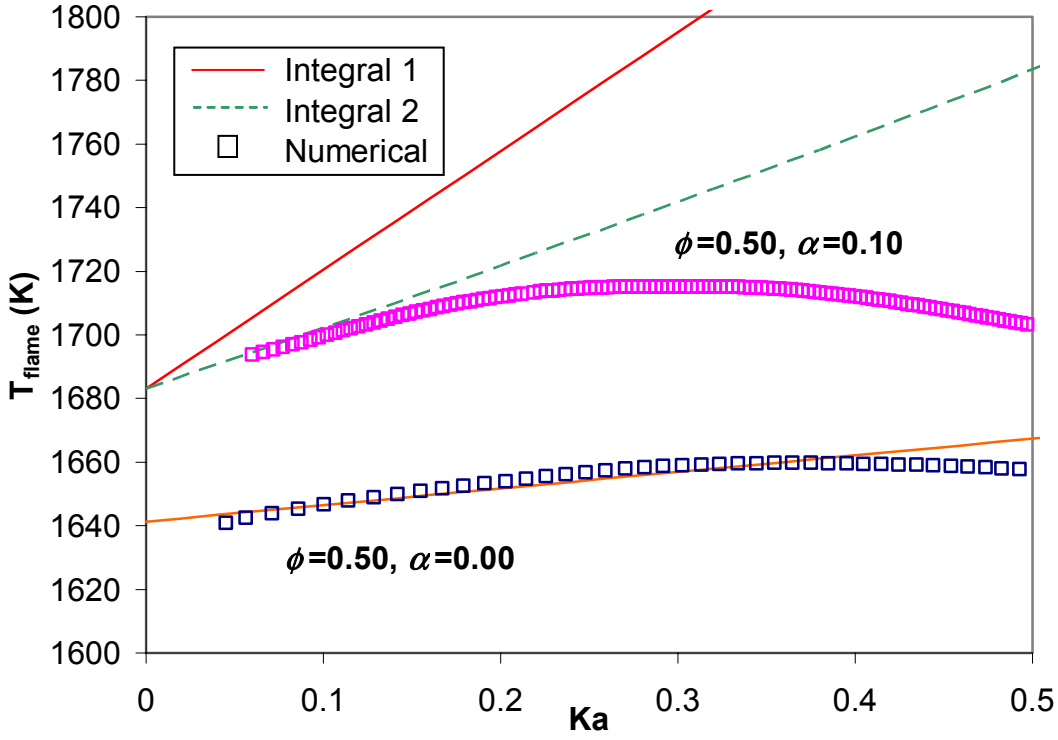

Figure 3.3: Computational and analytical predictions of T_{flame} for CH_4/H_2/air mixtures of $\phi = 0.5$ and $\alpha = 0.0$ and 0.10 (mixtures I and II).

As shown in Figure 3.3, T_{flame} increases with increasing strain for $Ka << 1.0$ for the numerical solutions as well as the integral analysis. This is as expected due to the fact that for both fuel components (CH_4 and H_2), $Le_k < 1.0$ as reported in Table 3.1. The $\phi = 0.50$, $\alpha = 0.0$ results are the same as in Figure 3.2. They are included here for comparison to the results for the $\phi = 0.5$, $\alpha = 0.10$ flame. The results of both integral analyses are plotted in the figure for the multi-component case, because the analyses yield different T_{flame} versus Ka. The first integral analysis method assumed a single reaction zone, while the second assumed discrete reaction zones for each fuel species.

The computational T_{flame} values do not extend all the way to $Ka = 0$, due to numerical difficulties at such low strain rates. As Ka, and the corresponding U_{in}, decrease, the flame moves further from the stagnation plane and closer to the inlet boundaries. At the edge of the thermal diffusion zone, the axial velocity sharply increases due to thermal expansion. When the flame moves close enough to the inlet boundary that the thermal expansion zone is within two computational cells from the boundary, the numerically predicted strain rates are strongly influenced by the $\partial U_{in}/\partial x = 0$ condition enforced at the inlet and are no longer valid. However, T_{flame} is linear approaching $Ka = 0$ and it may be easily extrapolated to zero strain. It can be seen that the numerical and analytical T_{flame} responses are very similar for both mixtures at $Ka < 0.15$ ($\kappa < 255$ 1/s). However, for the case with $\alpha = 0.10$, the second integral relation, assuming discrete reaction zones, provides a better estimate of the computed T_{flame} increase with Ka. The second integral relation decreases the importance of the secondary fuel, in this case H_2, in the prediction of T_{flame}. The Le effects of H_2 are confined to the first reaction zone and do not affect the behavior of the CH_4 diffusion. The T_{flame} slope

increase for the first and second integral relations are 373K and 189K per unit *Ka*, respectively. The slope of the computational results may be approximated as 150K per unit *Ka*.

3.3.2 C_3H_8 mixtures

C_3H_8/H_2 fuel mixtures provide an interesting comparison with CH_4/H_2 fuel mixtures because unlike for CH_4, the $Le_{C3H8} > 1.0$ for lean fuel/air mixtures. Figure 3.4 is a plot of the analytical and computational T_{flame} predictions for C_3H_8-H_2-air flames with ϕ = 0.75 and α = 0.00, and 0.10. The computational *Ka* was determined by scaling κ using the computational flame thickness and the approximated flame speed at zero strain. For the cases presented here, *Ka* = 0.1 corresponds to κ = 1025 1/s for the α = 0.00 case and κ = 1450 1/s for the α = 0.10 case.

The computational T_{flame} decreases with increasing strain for both mixtures. As can be seen in Table 3.1, Le_{C3H8} = 1.74 and 1.88 for the α = 0.00 and 0.10 mixtures, respectively. If the effect of the H_2 diffusion is ignored, the lower Le_{C3H8} for the case with α = 0.10 should result in a faster decrease in T_{flame} with *Ka*. However, the addition of H_2 to the mixture increases diffusion of reactant into the flame zone. This makes the flame zone richer, and decreases the magnitude of the negative slope of T_{flame} versus *Ka*. The computational results reflect this decrease in magnitude of the T_{flame} slope. The slope of the analytical results for the α = 0.00 case is very similar to the numerical slope. The analytical slope is -615K per unit *Ka* and the numerical is approximately -645K per unit *Ka*.

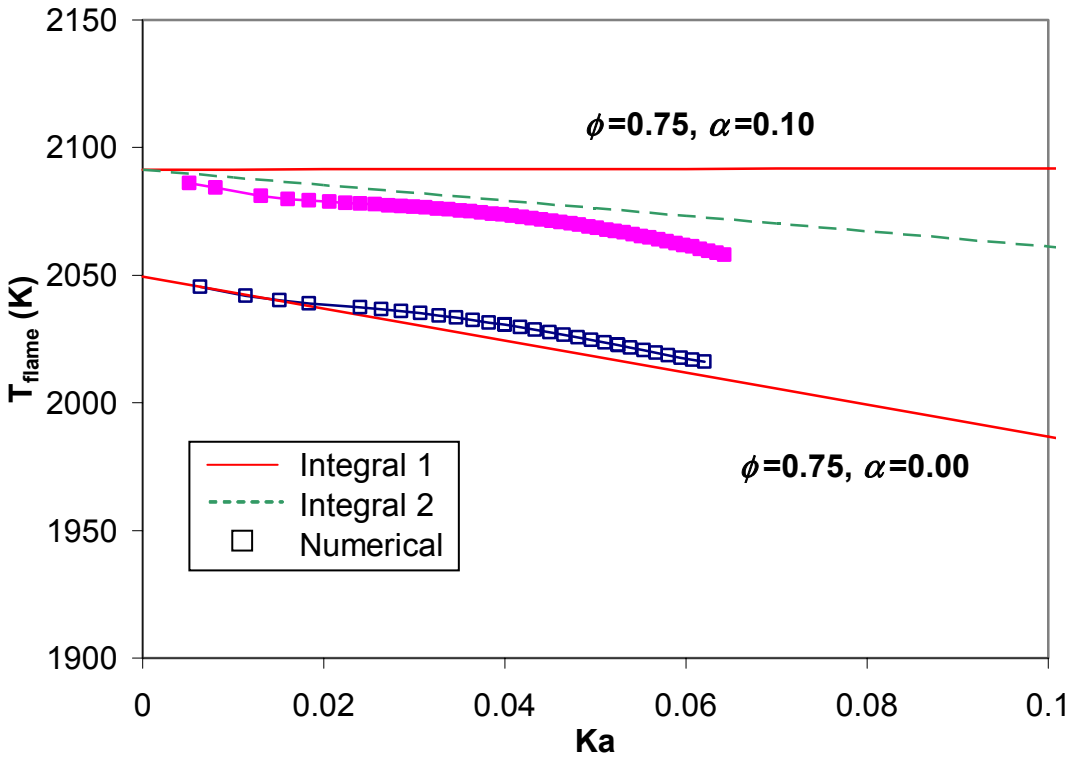

Figure 3.4: Computational and analytical predictions of T_{flame} for C_3H_8/H_2-air mixtures of $\phi = 0.75$ and $\alpha = 0.0$ and 0.10 (mixtures IV and V).

For the $\alpha = 0.10$ case, the two integral analyses provide very different T_{flame} predictions. The integral analysis shows a slight increase in T_{flame}, 49K per Ka, while the second integral analysis indicates a negative slope of -274K per Ka. The computational results indicate an approximate slope of -230K per Ka. The second integral relation does a better job of capturing the effect of H_2 addition.

3.4 Effective *Le*

As mentioned above, both the multi-component relations simplify to the same single-component equation from the literature. It is possible to compute an effective *Le*, Le_{eff}, for the multi-component mixtures. Using the Le_{eff} with the single component equations will provide the correct behavior of the flame with respect to strain, and should

provide a basis for comparing the expected T_{flame} behavior between mixtures of various compositions. The equations for Le_{eff} were presented in the previous chapter and are repeated here for reference. Equation (2.23) defines Le_{eff} for the single reaction zone

$$\frac{1}{Le_{eff}} = \sum_{k=1}^{K} \frac{\hat{q}_k}{Le_k}, \tag{2.23}$$

integral analysis. It is more complicated to determine a direct relation for Le_{eff} from the second integral analysis, for discrete reaction zones. An alternative method to find Le_{eff} is to use equation (2.25) and solve for Le_{eff}

$$Le_{eff} = \frac{1}{\frac{1}{Ka}\left(\frac{T_{flame} - T_0}{\Delta T^0} - 1\right) + 1} \tag{3.3}$$

where the variables are as defined in Chapter 2.

Table 3.2 provides the predicted Le_{eff} using both methods described above. A third Le_{eff} is also provided in Table 3.2. The third method assumes the mixture properties are ignored and the Le_{eff} is taken as the Le of the dominant fuel species. For a CH_4 mixture with $\phi = 0.75$ and $\alpha = 0.10$, the dominant fuel species would be CH_4 based on the mass fraction of CH_4. All three methods evaluate the Le_{eff} using mixture properties at the nozzle exits, upstream of any thermal or mass diffusion effects.

Table 3.2: Le_{eff} for each fuel mixture considered as computed using three methods.

Mixture	**I**	**II**	**III**	**IV**	**V**
Single Zone	0.954	0.748	0.944	1.74	0.969
Discrete Zones	0.954	0.855	0.944	1.74	1.216
Dominant Le	0.954	1.001	0.944	1.74	1.88

The single component mixtures, I, III and IV de facto give the same Le_{eff} for each method. The behavior of T_{flame} with respect to strain is captured by the *Le* of the single fuel species. Mixtures II and V have multiple fuel species. If the *Le* of the dominant fuel species is used to characterize T_{flame} response, the incorrect behavior will be seen. In mixture II, the dominant species is CH_4 by mass fraction and $Le_{CH4} = 1.001$. However, as in Figure 3.3 that the flame temperature increases with increasing strain for low *Ka*, even with the detailed chemistry numerical simulations. This behavior is indicative of an $Le_{eff} < 1.0$. Therefore the two analytical models developed here capture the combined effects better than simply assuming the dominant species *Le* controls the T_{flame} response to strain. The Le_{eff} for the single and discrete methods are 0.748 and 0.855, respectively. The two methods differ in the amount of contribution from the secondary fuel species to Le_{eff}.

The difference between the three Le_{eff} is even greater for mixture V with C_3H_8 and H_2. The dominant fuel species, C_3H_8, has a $Le = 1.88$. This would cause a sharp decrease in T_{flame} with increasing *Ka* not seen in Figure 3.4. The negative T_{flame} versus *Ka* slope for mixture IV is less steep than would be predicted from the dominant fuel species with $Le_{eff} = 1.88$. However, like with the CH_4/H_2 mixtures, the two analytical methods for C_3H_8/H_2 fuel mixtures produce very different Le_{eff} as well, with the single reacting zone model $Le_{eff} = 0.969$ and the discrete reacting zone model $Le_{eff} = 1.216$. The two models will give different response of T_{flame} with respect to Ka. The single reacting zone model has $Le_{eff} < 1.0$, and therefore predicts T_{flame} will increase with increasing *Ka*. The discrete reacting zone model has $Le_{eff} > 1.0$, predicting will decrease with increasing *Ka*. As in Figure 3.4, T_{flame} does decrease with increasing *Ka*. The discrete reacting zone

model appears to have better captured the combined influence of the *Le* for each fuel species.

3.7 Conclusions

For counterflow flames exposed to low strain in the linear region, the behavior of flame temperature with respect to strain rate may be accurately predicted using simple analytical models developed from integral analyses. When these analytical models are applied to reactant mixtures with a single fuel species, al the models predict the same T_{flame} variation with respect to imposed strain. However, when reactant mixtures with more than one fuel species are used, the models predict different T_{flame} responses. The response of the mixture T_{flame} is controlled by a combination of the properties of each fuel species. The two integral models developed in the previous chapter combine the effects of each fuel species to give different T_{flame} results. The results shown here indicate that the analytical model developed assuming discrete reaction zones better match the numerically predicted T_{flame} versus Ka.

An Le_{eff}, can be computed for each mixture to capture the mixture effects with a single *Le*. Again, the discrete reaction zone model better matched the predicted behavior. Using the single reaction zone model gave a $Le_{eff} < 1.0$ for a C_3H_8-H_2-air mixture. The computationally predicted T_{flame} decreased with increasing strain, indicating a $Le_{eff} > 1.0$, which was predicted using the discrete reaction zone model. Finally, if the *Le* of the dominant fuel species is assumed to capture the effects of T_{flame} with respect to strain, the resulting T_{flame} predictions do not match the trends seen in the numerical results.

Chapter 4 Transient Model Description

4.1 Introduction

As computational power has increased, the ability to numerically model dynamic processes in flames has become more accessible to combustion researchers. The computational advances combined with improved experimental diagnostics for transient measurements have led to several recent studies on the effects of imposed oscillations on premixed flames. These studies, and the current study, have often relied on using the counterflow flame configuration, since the core central flow is well characterized by a single strain rate, κ.

The current study extends previous modeling efforts on oscillatory premixed flames by exploring the impact of fuel composition on the flame behavior. Recent studies have explored the addition of small amounts of H_2 to CH_4 and its influence on extinction strain rates and flammability limits [1, 4, 5]. The effects of H_2 addition on the early flame chemistry and, to a lesser extent, on the diffusive transport upstream of the flame lead to an extension of the extinction strain rates as well as improved combustion efficiency compared to pure CH_4 fuels for a given strain. It has been shown that premixed flame response to upstream velocity oscillations is a function of fuel Lewis number [19]. As the addition of H_2 impacts the effective fuel Lewis number [1], this study investigates the influence of H_2 addition on the response of lean premixed CH_4 flames to oscillations in strain rate. The current study focuses on lean-premixed flames in hopes of gaining some insight for practical low-NO_x premixed combustion system behavior. In particular, the reactant compositions will be composed of mixtures of CH_4, H_2 and air with $\phi = 0.50$ or 0.75 and $\alpha = 0.00$, 0.05, or 0.10.

This chapter presents the development of computational code, for modeling counterflow, opposed-jet, premixed flames with imposed transient inlet conditions. The code provides the basis for assessing how near extinction behavior under oscillatory flow conditions is influenced by the fuel composition. The objective of the numerical modeling effort presented later in this thesis was to assess, both qualitatively and quantitatively, the impact of H_2 addition to hydrocarbon flame behavior and stability.

4.2 Computational Model

4.2.1 Transient equation set

Previous non-transient models, including the numerical model discussed in Chapters 2 and 3, have solved the steady state, incompressible system [3, 28, 29, 44-46]. These models assume incompressible flow, which leads to an infinite Mach number and requires pressure disturbances to be transmitted instantly throughout the system. Therefore, when a fluctuation is imposed at the boundary the effects must be immediately felt throughout the system. This is not physically correct and gives rise to numerical instabilities when large amplitude, high frequency fluctuations are imposed on the system [37].

To model the transient combustion processes in this thesis, a different formulation is required to correctly model the imposed fluctuations and allow the pressure disturbances to move through the system at acoustic speeds. To achieve this, the computational model development of the transient model followed previous work in the area of transient combustion phenomena [37].

The model simulates the one-dimensional flow along the centerline of the axisymmetric opposed-jet flow. The equations may be derived from the standard,

compressible conservation laws in cylindrical coordinate system, and since along the center-line all first order derivatives in the radial an circumferential directions vanish to zero, the transient conservation equations collapse to one-dimensional equations with an eigenvalue associated with the radial pressure derivative divided by *r* at the centerline [29].

$$\Lambda = \frac{1}{r}\frac{dP}{dr}. \tag{4.1}$$

The differential conservation equations governing the axisymmetric centerline flow in the counterflow system of equation are given as follows:

Continuity

$$\frac{\rho}{Ptot}\frac{\partial P}{\partial t} - \frac{\rho}{T}\frac{\partial T}{\partial t} - \rho\overline{W}\sum_k \frac{1}{W_k}\frac{\partial Y_k}{\partial t} + \frac{\partial}{\partial x}(\rho u) + 2\rho V = 0, \tag{4.2}$$

Axial Momentum

$$\rho\frac{\partial u}{\partial t} + \rho u\frac{\partial u}{\partial x} + \frac{\partial P}{\partial x} - 2\mu\frac{\partial V}{\partial x} - \frac{4}{3}\frac{\partial}{\partial x}\left(\mu\frac{\partial u}{\partial x}\right) + \frac{4}{3}\frac{\partial}{\partial x}(\mu V) = 0, \tag{4.3}$$

Radial Momentum:

$$\rho\frac{\partial V}{\partial t} + \rho u\frac{\partial V}{\partial x} - \frac{\partial}{\partial x}\left(\mu\frac{\partial V}{\partial x}\right) + \rho V^2 + \Lambda = 0, \tag{4.4}$$

Energy Conservation:

$$\begin{aligned}&\rho C_p\frac{\partial T}{\partial t} + \rho c_p u\frac{\partial T}{\partial x} - \frac{\partial P}{\partial t} - u\frac{\partial P}{\partial x} - \frac{\partial}{\partial x}\left(\lambda\frac{\partial T}{\partial x}\right) + \rho\sum c_{p,k}Y_k U_k\frac{\partial T}{\partial x},\\ &+\sum\dot{\omega}_k h_k = 0\end{aligned} \tag{4.5}$$

and Species Conservation:

$$\rho\frac{\partial Y_k}{\partial t} + \rho u\frac{\partial Y_k}{\partial x} + \frac{\partial}{\partial x}(\rho Y_k U_k) - \sum\dot{\omega}_k W_k = 0. \tag{4.6}$$

The excess pressure is defined as

$$P = P_{tot} - P_{atm}\,, \tag{4.7}$$

and the equation of state

$$\rho = \frac{(P + P_{atm})\overline{W}}{RT}. \tag{4.8}$$

The independent variables are U, the axial velocity, T, the temperature, P, the excess pressure, Y_k, the mass fraction of species 'k', Λ, and V, the radial velocity ratio defined as

$$V \equiv \frac{v}{r}. \tag{4.9}$$

The Λ in the radial momentum equation is an eigenvalue of the system as defined in equation (4.1). Λ is a constant throughout the flow field for a steady state case, and each steady state solution can be characterized by this single value. For the transient case, the eigenvalue varies in time but remains constant with respect to the axial distance. The equation

$$\frac{d\Lambda}{dx} = 0\,, \tag{4.10}$$

for Λ is added to the equation set to ensure the iteration matrix is tridiagonal.

The remaining terms are W_k, molecular weight of species 'k', $\overline{W}$, the average molecular weight of the mixture, ρ, the density, h_k, the species enthalpy, and $\dot{\omega}$, the generation rate of species 'k'. The viscosity and conductivity are μ and λ, respectively. c_p is the mixture specific heat at constant pressure, and $c_{p,k}$ is the constant pressure specific heat of species 'k'.

4.2.2 Solution domain and boundary conditions

The transient equation set is solved over a domain spanning the entire distance between the two nozzle exits of a counterflow flame configuration. The entire domain was used, instead of assuming symmetry at the stagnation plane. This was done to move the boundaries far from the region of interest to limit the influence on the flame properties of any numerical errors incurred from the boundary conditions. In addition, this also allowed the future possibility of imposing different oscillations at each nozzle inlet boundary. However, non-symmetric oscillations were not used in this study. Non-symmetric oscillations would cause movement of the center of the flame zone, adding complexity to experimental measurements. Therefore, the experimental work consisted of symmetric oscillations and the computational modeling was similarly restricted to allow comparison to the experiments.

The equations are solved using a staggered computational grid with one node fixed at the exact center of the domain [37, 47]. The center point was used to ensure the centerline values were obtained in the solution. An example of the grid is shown in Figure 4.1. All the equations except for the axial momentum equation are descretized using the cell centers of a one-dimensional finite volume grid. The axial momentum is descretized using properties at the cell faces and is, therefore, considered staggered from the rest of the solution. The use of a staggered grid allows central differencing of the continuity equation [48]. Central differencing is only neutrally stable, so artificial viscosity is added to the continuity equation to ensure stability. The artificial viscosity is of the form

$$+\mu_{art}\frac{d^2P}{dx^2}, \tag{4.11}$$

and μ_{art} is set to a small value, -1*10^{-6}.

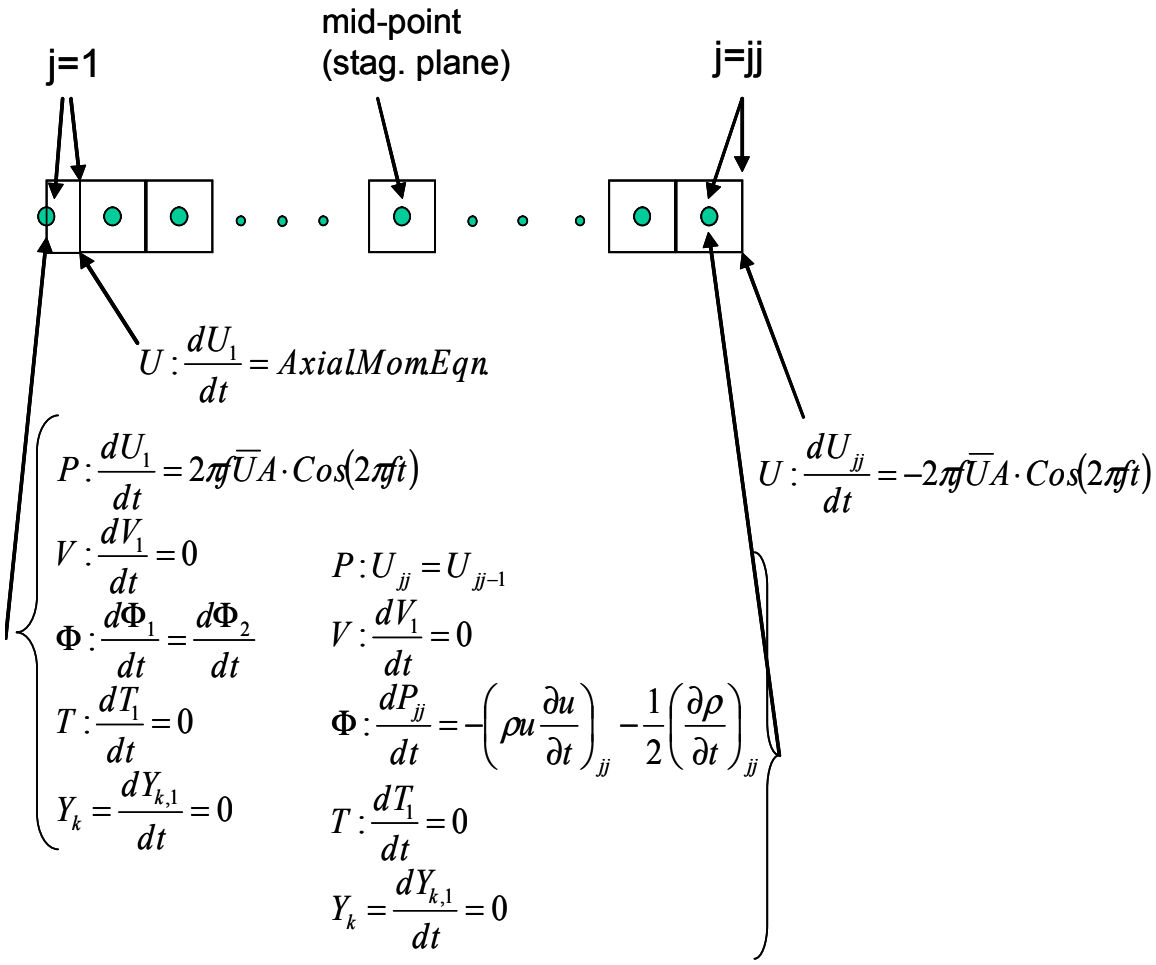

Figure 4.1: Schematic illustrating the computational grid and the applied boundary conditions.

Velocity fluctuations at the boundary are imposed using

$$U_{in} = \overline{U}\left(1 + A\left(1 + Sin\left(2\pi f t\right)\right)\right), \tag{4.12}$$

where $\overline{U}$ is the initial, or mean, inlet velocity, and A and f are the amplitude and frequency of the velocity variations, respectively. This function form was chosen for the

imposed oscillations because it provides a U_{in} that varies ±A* $\overline{U}$ about the initial inlet velocity. The fluctuating boundary condition is applied using its time derivative

$$\frac{dU_{inlet}}{dt} = 2\pi f \overline{U} A \cdot Cos\left(2\pi ft\right). \tag{4.13}$$

The numerical solution method converges to a solution faster when time derivative are used at the boundaries. The solution method is described in detail in Section 4.3. At time zero, the axial velocity equals the mean initial value and the time derivative of the velocity is also zero. The zero derivative at t = 0s provides the opportunity to start from a consistent set of initial conditions provided by the steady state counterflame simulations described in Chapter 2. On the other hand, the slope of the oscillation is at its maximum at time zero, which requires very small timesteps at the beginning of the solution for stability. An example if the imposed oscillation is plotted in Figure 4.2. Note that the opposite nozzles have opposite oscillations imposed.

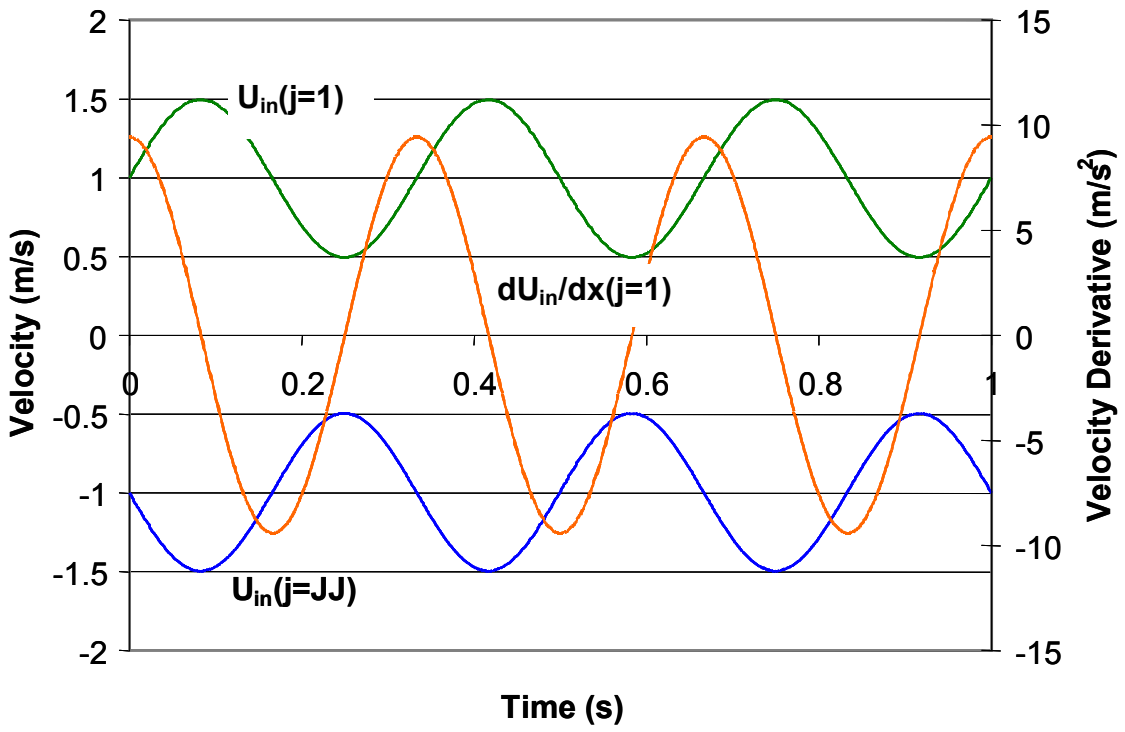

Figure 4.2: A plot of the applied oscillating axial velocity at the two boundaries and the derivative of the velocity at the first cell.

The pressure at the nozzle boundary varies according to the velocity, and is determined by taking the time derivative of the Bernoulli equation,

$$\left(P + P_0\right) + \frac{1}{2}\rho u^2 = Const\,, \tag{4.14}$$

which gives

$$\frac{\partial P}{\partial t} + \rho u \frac{\partial u}{\partial t} + \frac{1}{2}\frac{\partial \rho}{\partial t} = 0\,. \tag{4.15}$$

The form of the Bernoulli equation in equation (4.14) neglects the transient terms. It was assumed that due to the low flow velocities relative to the speed of sound, the transient terms would have a negligible effect on the boundary condition and on the flame behavior. Furthermore, simplifying the pressure boundary condition to equation (4.15)

allowed faster convergence of each step in the numerical code. Therefore, the transient terms were ignored. A computational test case was computed which included the transient terms in the pressure boundary condition. The results of this test case were compared to the results using the boundary conditions as stated here. The comparison is shown in Section 4.6.

The remaining boundary conditions, temperature, radial velocity ratio, radial pressure gradient and species mass fractions are held constant. Their time derivatives are therefore zero. The boundary conditions for these variables are

$$\frac{dG}{dt} = 0\,, \tag{4.16}$$

where G is T, V, Y_k, or Λ.

The boundary conditions were imposed as shown in Figure 4.1. The second order radial momentum, energy and species conservation equations require two boundary conditions each. Continuity, axial momentum and eigenvalue equations are first order and require only one boundary condition each. A unique descretization method was used to apply the required boundary conditions to the domain.

The radial momentum, energy and species conservation, and continuity equations are central differenced. The axial momentum equation is considered a first order equation and is forward differenced along with the eigenvalue equation. At the first cell, the temperature, radial momentum and species mass fractions boundary conditions are set to

$$\frac{dT}{dt} = \frac{dV}{dt} = \frac{dY_k}{dt} = 0\,. \tag{4.17}$$

The axial momentum equation is solved at its first node, a half-cell into the domain. The continuity equation at the first cell is used to impose the axial velocity variation, and the eigenvalue at cell one is set equal to the value at cell two.

At the last cell in the domain, the energy, radial momentum and species mass fractions boundary conditions are set just as the first cell, shown in equation (4.17). Because the axial velocity was forward differenced, the last cell must be used to impose the time varying oscillations. The continuity equation is used to set the axial velocity at the last cell equal to the preceding cell. Finally, the eigenvalue equation for the last cell is used to impose the Bernoulli pressure boundary to compute the pressure variation with respect to the imposed velocity variation.

4.3 Solution Method

4.3.1 Transient numerical solver

When descretized using the various differencing schemes described above, the conservation equations (equations (4.2)-(4.6) and (4.10)) and the corresponding boundary conditions (equations (4.13), (4.15) and (4.17)) form a set of Differential Algebraic Equations (DAE). The eigenvalue, Λ, in the equation set is solved as an algebraic, not differential equation, in the system. The fact that the time derivative Λ of does not appear in the equation set makes the system a DAE index-2 system. The index of a DAE system refers to the number of times any part of the system needs to be differentiated with respect to time to make the entire system a continuous function of time. DASSL, and other similar numerical solution algorithms, can only control errors for at most index-

1 systems [47]. To reduce the index, a substitution may be made for the eigenvalue. In the final equation set, the following substitution is made

$$\frac{d\Phi}{dt} = \Lambda(t), \tag{4.18}$$

to reduce the DAE system to Hessenberg index-1 form [37, 49]. A system of this type is numerically stable, and may be solved using a DAE solver such as DASSL [50] or LIMEX [51]. Both of the DAE solvers can adaptively adjust the timestep to maintain the solution stability during fast transients.

The DAE solution algorithms require a converged steady state solution as input to begin the transient iterations. To compute a steady state initial condition, a FORTRAN code, CFPWHOLE, was developed to obtain a steady state solution of the above formulation. The steady state formulation is found by setting the time derivatives equal to zero and retaining the Λ term instead of making the transformation to ϕ. CFPWHOLE uses the same domain, computational grid as the transient code with steady state boundary conditions. The numerical solver TWOPNT [40] is used to converge to the solution. The output from the steady state code was then used as the initial, mean condition for the transient code. The steady state solution method is also discussed in Chapter 2.

4.3.2 Analytical Jacobian

The solution of the DAE using DASSL requires the evaluation of the Jacobian of the descretized equation set. The Jacobian may be evaluated numerically, but this is a computationally intensive task. For numerical Jacobian evaluation, partial derivatives of each equation at each point must be computed with respect to all the variables at all the

grid points. About 97% of the computational time for TREC is spent evaluating the Jacobian. A faster alternative is to provide DASSL with a routine to compute the Jacobian analytically. This requires analytical equations for the partial derivatives. Because the variables at a given node are only influenced by its neighboring points, most of the Jacobian entries are zero and the Jacobian matrix is a banded matrix. An analytical Jacobian routine was included in TREC. When the analytical Jacobian in TREC is used, each iteration takes 45% of the time required when using the numerical Jacobian.

4.3.3 Evaluation of chemical properties

As with the earlier steady state analysis, CHEMKIN [27] was used along with GRI-Mech v3.0 [41] to evaluate the chemical kinetics, thermodynamics and species diffusion. GRI-Mech is optimized for capturing ignition and extinction phenomena. Since the GRI-Mech mechanism is a large mechanism (53 species and 214 reactions), it takes considerable computational time to evaluate a solution. Therefore, a reduced mechanism was also used to model simple cases of CH_4-air [52] during code development.

The species mass diffusion velocities are evaluated using the multicomponent formulation of

$$V_k = \frac{1}{X_k \overline{W}} \sum_{j=1}^{K} W_j D_{kj} \frac{dX_j}{dx} - \frac{D_k^T}{\rho Y_k} \frac{1}{T} \frac{dT}{dx}, \tag{4.19}$$

where D_{kj} is are the multicomponent coefficient of diffusion between species k and j, and D_k^T is the thermal diffusion coefficient for species k. X_k is the mole fraction of species k. The multicomponent diffusion formulation provides more accurate diffusion velocities than a mixture averaged formulation. This is especially true when there are large

differences between the diffusion rates of important species, such as the diffusion of H_2 and CH_4 in this study. Modeling the effects of H_2 addition to CH_4 mixtures requires accurate representation of the diffusion velocities of these species.

4.4 Test Case Details

4.4.1 Mixture compositions

The focus of this study was to investigate the effects of doping lean, premixed CH_4-air flames with H_2. The mixture compositions used were determined from the global combustion reaction for a lean flame assuming complete combustion, reaction (R2.1), discussed earlier and repeated here:

$$(1-\alpha)CH_4 + 4\alpha H_2 + \frac{2}{\phi}\left(O_2 + \frac{79}{21}N_2\right) \Rightarrow (1-\alpha)CO_2 + (2+2\alpha)H_2O + \frac{2}{\phi}\left((1-\phi)O_2 + \frac{79}{21}N_2\right) \quad \text{(R2.1)}$$

In the above reaction, α represents the percentage of O_2 consumed by H_2. When $\alpha = 0$, all the O_2 is consumed by CH_4, and when $\alpha = 1$ all the O_2 is consumed by H_2.

For the cases modeled and tested in this study, the value of ϕ was fixed at either 0.5, or 0.75, and α was set to 0.0, 0.05, or 0.10. The different equivalence ratios and alphas create large differences in premixed flame properties, such as Le_k's, flame speed, flame temperature and steady state extinction strain rate. For example, for a reactant composition of $\phi = 0.05$, $\alpha = 0.00$ $Le_{CH4} = 0.95$, while for a mixture with $\phi = 0.75$, $\alpha = 0.10$ $Le_{CH4} = 1.01$. With $\alpha = 0.10$ and $\phi = 0.5$, the mole fractions for H_2 and O_2 are the equal. Table 4.1 shows the fuel compositions investigated in this study with their corresponding mass and mole fractions. The limited range of alpha was set to look at

what might be practical mixtures of H_2 and CH_4 in a real combustion system where the addition of high purity H_2 is limited by its high production and the processing costs.

Table 4.1: Mass fractions the species in each fuel mixture used in the study.

	α	Y_{CH4}	Y_{H2}	Y_{O2}	Y_{N2}
$\phi = 0.50$	0.0	0.02837	0	0.2263	0.7453
	0.05	0.02697	0.0007	0.2265	0.7458
	0.10	0.02557	0.001	0.2267	0.7464
$\phi = 0.75$	0.0	0.04196	0	0.2232	0.7349
	0.05	0.03990	0.001	0.2234	0.7356
	0.10	0.03784	0.002	0.2236	0.7364

4.4.2 Initial conditions

Since this study investigated near extinction flames, the initial, or mean, steady state flame conditions for each case were flames with strain rates near the steady state extinction strain rate. Using the steady state counterflow flame code written for this study, CFPWHOLE, steady state flames were computed for a large range of strain rates. The steady state flames were initially solved at a low strain rate, $\kappa/\kappa_{ext} < 0.60$, because flame solutions are easier to compute at low relative strain rates. The strain rate was then incrementally increased and a new steady state flame was found. This process was repeated until the steady state extinction strain rate, $\kappa_{ext,}$ was reached for each fuel mixture composition. With the extinction strain rate determined, the strain rate variation of each steady state case could be transformed to the ratio, κ/κ_{ext}, where κ is the steady state strain rate, and κ_{ext} is the steady state extinction strain rate for the corresponding mixture. Using the strain rate ratio, initial conditions were selected which matched the values $\kappa_{init}/\kappa_{ext} = 0.8, 0.9, 0.95$, where κ_{init} is the strain rate of the initial steady state flame

prior to imposing oscillations. Table 4.2 contains the steady state extinction strain rates for each fuel composition used in this study. The large increase in the steady state extinction strain rate resulting from the addition of H_2 has been well documented in other studies [1], and is one of the motivations for considering H_2 addition to hydrocarbon fuels. When α is increased from 0.00 to 0.10 for a steady state CH_4 flame with $\phi = 0.50$, κ_{ext} increases over 300% [1].

Table 4.2: Steady state extinction strain rates, κ_{ext} (1/s), and inlet velocities, U_{in} (m/s) for each fuel mixture composition for a counterflow domain with a 0.7cm separation between nozzle exits.

$\phi \setminus \alpha$	**0.0**	**0.05**	**0.10**
0.50	1128 1/s 2.37 m/s	2013 1/s 4.04 m/s	3274 1/s 6.35 m/s
0.75	4644 1/s 8.76 m/s	6539 1/s 12.18 m/s	8826 1/s 16.30 m/s

As discussed in the preceding chapter, identical velocity oscillations are imposed on both boundaries of the computational domain. The oscillation frequencies were set to100, 200, 400 or 1000Hz. As previously discussed, the range of oscillation frequencies seen in gas turbines is typically in this range. This range of frequencies is typical of many destabilizing oscillations observed in some lean-premixed combustion systems for gas turbines and other applications [9] and is capable of generating a wide range of flame responses. The amplitude of oscillation is given as a percentage of the mean initial axial velocity, U_{mean}. An amplitude of 0.1 imposes a maximum velocity of $1.1*U_{mean}$, and a minimum of $0.9*U_{mean}$. For steady state flames and flames oscillated at low frequencies and low amplitudes, κ and U_{in} are linearly related. An increase or decrease in U_{in} will

produce a corresponding increase or decrease in κ, respectively. While running the transient code, the amplitude of the velocity oscillation is held constant for several cycles and is then stepped up by a user supplied increment. The incremental increases are typically in the range of $0.01*U_{mean}$ to $0.05*U_{mean}$. Step increases in amplitude larger than $0.05*U_{mean}$ generally caused immediate extinction due to instabilities caused by the impulsive change in inlet velocity. The number of cycles at each constant amplitude is set by the user, is typically between 2 and 4, and depends on the frequency and initial conditions. This process is repeated until either the maximum desired amplitude is reached or the flame extinguishes. The extinction amplitude can then be determined.

4.5 Convergence Study

A convergence study was conducted for both a steady state initial solution and a transient solution after a few cycles. The steady state convergence study examined the change in the solution with respect to grid refinement. The transient study examined the cumulative errors between the initial solution and the solution after several complete cycles with respect to grid refinement. The results of the study were used to help determine the optimal number of computational cells to use in the 1-D grid. With no absolute, standard flame solution to compare the results, the convergence study essentially examined the change in the solution as a function of grid refinement. It is assumed that as the computational mesh becomes more refined errors introduced through descretization and truncation will be reduced. However, as the number of grid cells increases round-off error becomes more significant. A solution computed with the largest number of points without obvious round-off error contribution can be used as the solution to compare with solutions computed using other levels of grid refinement.

For this study, a steady state CH_4-air counterflow flame with $\phi = 0.75$ and $\alpha = 0.10$ was computed using CFPWHOLE. A reduced CH_4-air mechanism [52] was used for the convergence study, leading to much faster computational times and allowing the use of many computation cells with a reasonable run time. The results of the steady state grid study can be seen in Figure 4.3, a plot of the relative error between each grid solution and the solution computed using 1600 cells. The relative error was computed as the percent difference between the value at each grid refinement level and the value from the 1600 cell grid. The data in Figure 4.3 includes the relative error of T_{flame}, κ, and Y_{CO} at the stagnation plane. The relative error decreases until 400 cells, and there is a slight increase in error at 500 cells. The error again decreases for 600 cells. The solution for 800 and 1600 cells is identical to the accuracy of the reported solution. From these results, it appears that 400 cells provide a reasonably accurate solution with a manageable number of computational cells.

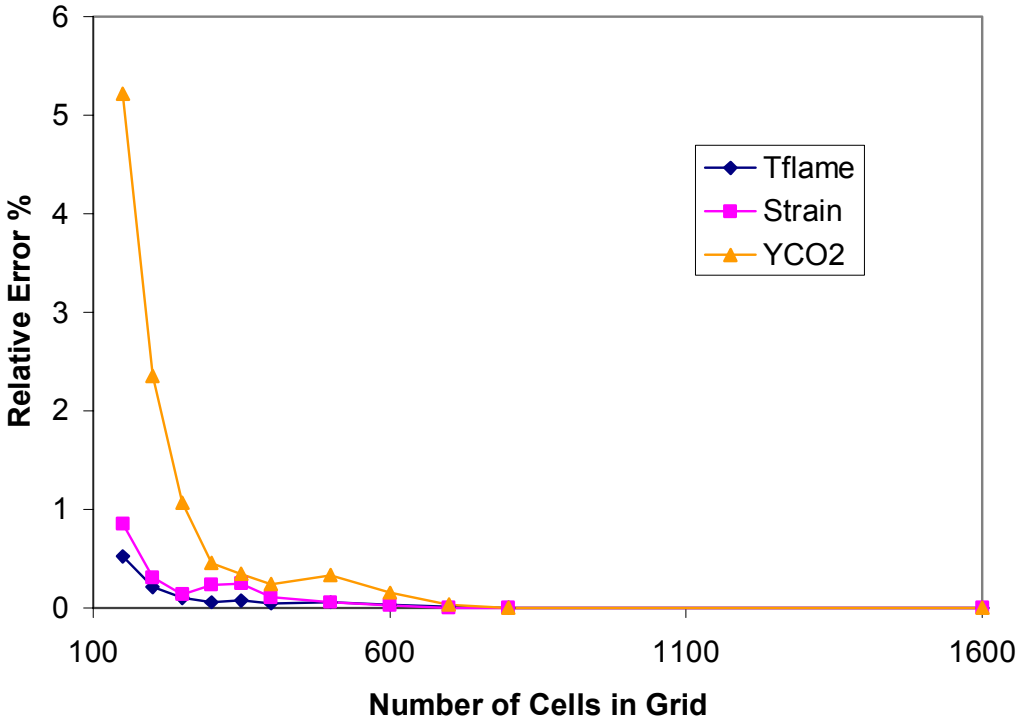

Figure 4.3: The variation of relative error of a steady state solution as a function of grid refinement for T_{flame}, flame strain rate (κ) and Y_{CO}.

The convergence study continued with a similar analysis for the transient computational code. The steady state flame computed for each level of grid refinement was used as initial conditions for the transient code. Each flame was oscillated for 3 cycles at 500Hz. T_{flame}, κ, and Y_{CO} at the stagnation plane were recorded at set time intervals for each case. Again, the 1600 cell solution was assumed the standard for comparison. Relative errors were computed using the following equation

$$\mathrm{Re}l.Error(F_n) = \frac{\left(\sum_i \left(F_{n,i} - F_{1600,i}\right)^2\right)^{1/2}}{F_{1600,1}} * 100\% \qquad (4.20)$$

where $F_{n,i}$ is either the flame temperature, the flow strain rate or the stagnation plane mass fraction of CO at timestep 'i' computed using a grid of 'n' cells. The results are plotted in Figure 4.4. Again, 400 cells appear to give a reasonably accurate solution.

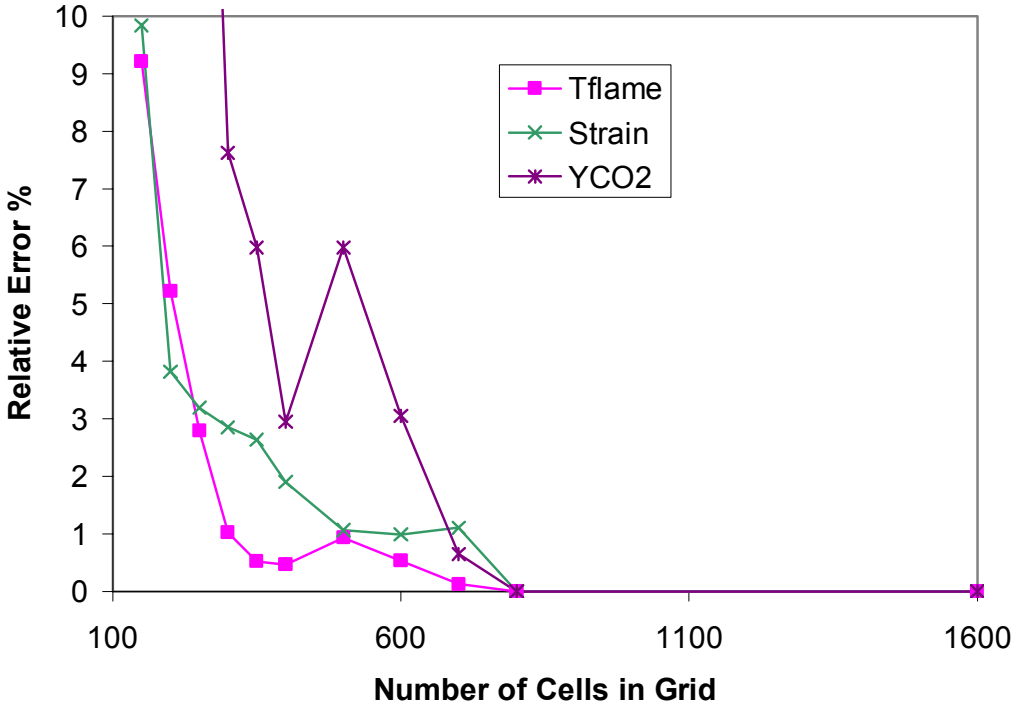

Figure 4.4: Relative error of three flame properties as a function of grid refinement after three transient cycles at 400Hz.

4.6 Example Results

A few sample results shown in this section will illustrate many of the characteristics observed in the transient results. As mentioned before, the transient code requires a converged steady state counterflow flame solution as an initial condition. The axial variation of several flame properties of a typical steady state solution is plotted as solid lines in Figure 4.5. For this example, $\phi = 0.75$, $\alpha = 0.10$ and $\kappa_{init}/\kappa_{ext} = 0.80$. The

flame zone is identified by the location of the steepest increase in temperature. The increase in temperature causes a drop in density and a corresponding increase in axial velocity approaching the flame zone, and this can also be seen in the axial velocity profile in Figure 4.5. The mass fraction of CH_4 decreases sharply beginning at approximately 0.5mm from the stagnation plane and reaches near zero by approximately 0.1mm from the stagnation plane. The CH_4 is completely consumed in this lean flame, and Y_{CH4} is essentially zero at the stagnation plane.

Figure 4.5 also shows the property values at the maximum and minimum of the imposed 200Hz velocity oscillations. It can be seen that the maximum velocity corresponds to a minimum T and maximum stagnation plane Y_{CH4}. The increased velocity causes an increased strain rate, moving the flame closer to the extinction strain rate. As the strain rate increases, the combustion weakens which can be seen by the decreased T_{flame} and the increased unburned CH_4 at the stagnation plane beyond the flame.

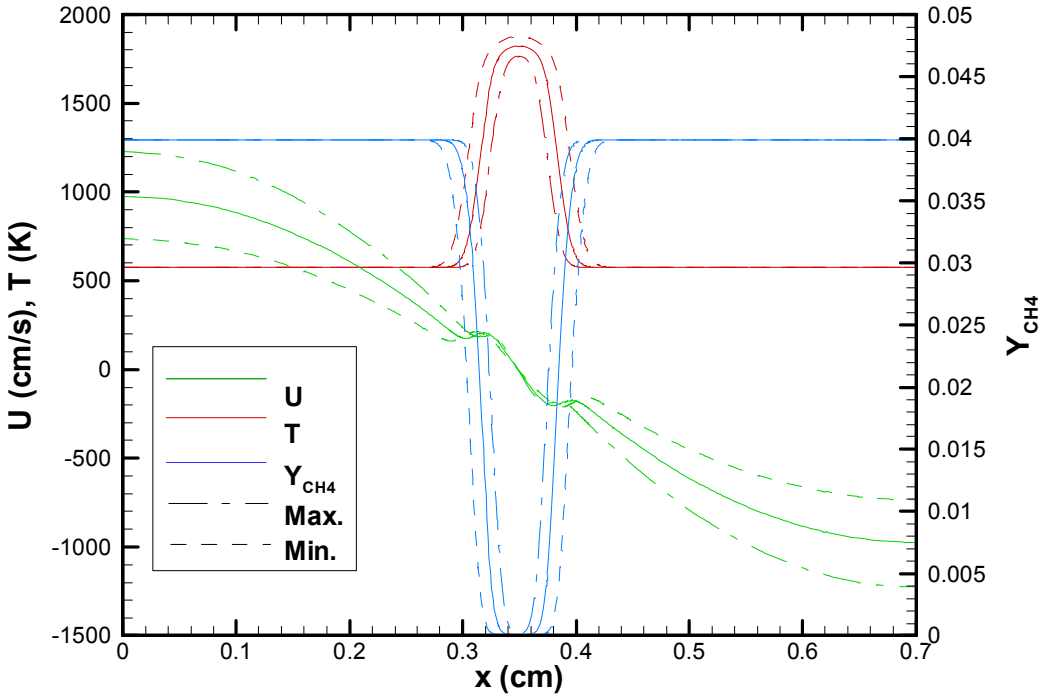

Figure 4.5: Gas temperature, axial velocity and Y_{CH4} values at mean, minimum, and maximum imposed strain at 200Hz with $\phi = 0.75$, $\alpha = 0.05$ and $\kappa_{init}/\kappa_{ext} = 0.80$.

While Figure 4.5 shows the extents of the temperature variations, the full variation in time can be seen in a contour plot of temperature as a function of time and axial distance. This can be seen in Figure 4.6. The contours show that the flame zone remains centered about the stagnation point, but constricts with increasing strain rate. The temperature also decreases with increasing strain during the oscillations. In this case the variations in velocity and temperature are in phase. At higher oscillation frequencies it can be seen that there is a phase shift between the imposed velocity oscillations and the flame response.

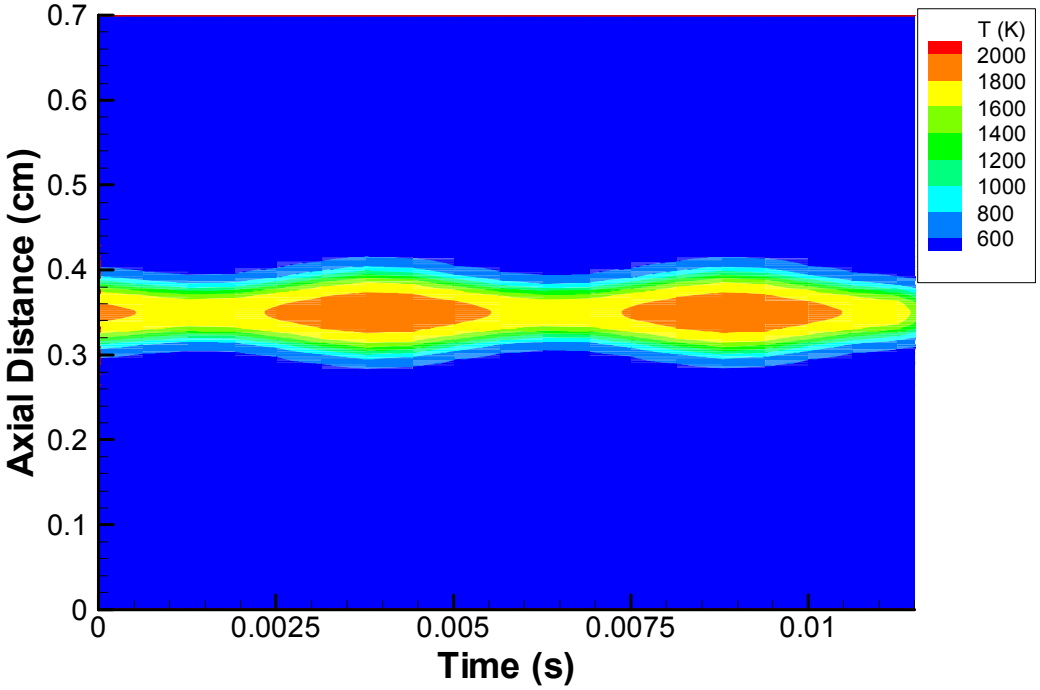

Figure 4.6: Contour plot of the temperature variation between the counterflow nozzles versus time for the example case with $\phi = 0.75$, $\alpha = 0.05$ $\kappa_{init}/\kappa_{ext} = 0.80$ and $f = 400$Hz.

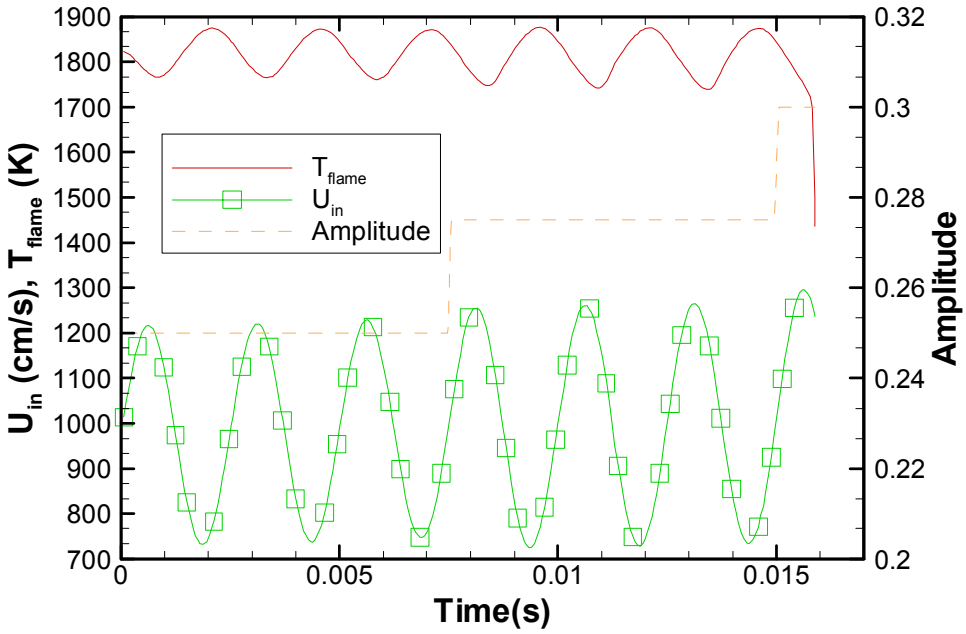

Figure 4.7: Variation of flame temperature and axial velocity with increasing amplitude for $\phi = 0.75$, $\alpha = 0.05$ $\kappa_{init}/\kappa_{ext} = 0.80$ and $f = 400$Hz.

Figure 4.7 illustrates the method used to determine the amplitude of oscillation that causes flame extinction. The variation of flame temperature, inlet velocity and the oscillation amplitude can be seen in the figure. The temperature decreases with increasing velocity. The amplitude of the oscillations is originally $A = 0.20$. After 3 cycles, the amplitude is stepped up to $A = 0.25$. The variation in temperature increases with the increased amplitude. After three cycles, the amplitude is again increased and the final amplitude is $A = 0.30$. Shortly after this final increase in oscillation amplitude, the temperature drops sharply to 1500K. At this point, the flame has extinguished. The extinction amplitude is therefore between $A = 0.25$ and $A = 0.30$.

The earlier figures plotted flame properties as a function of either time or inlet velocity. Counterflow flames are characterized by the κ of the flow field, and combustion properties of different flames may be easily compared by comparing κ's. Therefore, it is useful to plot the transient flame property variation as a function of κ. In Figure 4.8, the temperature variation of the example case is plotted versus the strain rate variation. The black line represents the steady state behavior of T_{flame} respect to κ and the circle marks the initial solution used for the transient integration. The steady state curve ends at the point of maximum steady state strain for the flame, the extinction strain rate κ_{ext}. As κ increases from the initial condition, the T_{flame} begins to decrease. However, the decrease in T_{flame} lags behind the steady state response, causing T_{flame} to diverge from the steady state values. As κ passes its maximum, T_{flame} decreases below the steady state curve. With decreasing κ, T_{flame} begins to rise and eventually increases above the steady state curve. Figure 4.8 shows the flame temperature varying over three similar cycles before the amplitude of the imposed oscillations increases and the temperature

oscillations also increase in magnitude. As seen earlier, after three more cycles the amplitude increases again and the flame extinguishes. It is notable that Figure 4.8 illustrates that the flame persists even with strain rates temporarily greater than the steady state extinction strain rate.

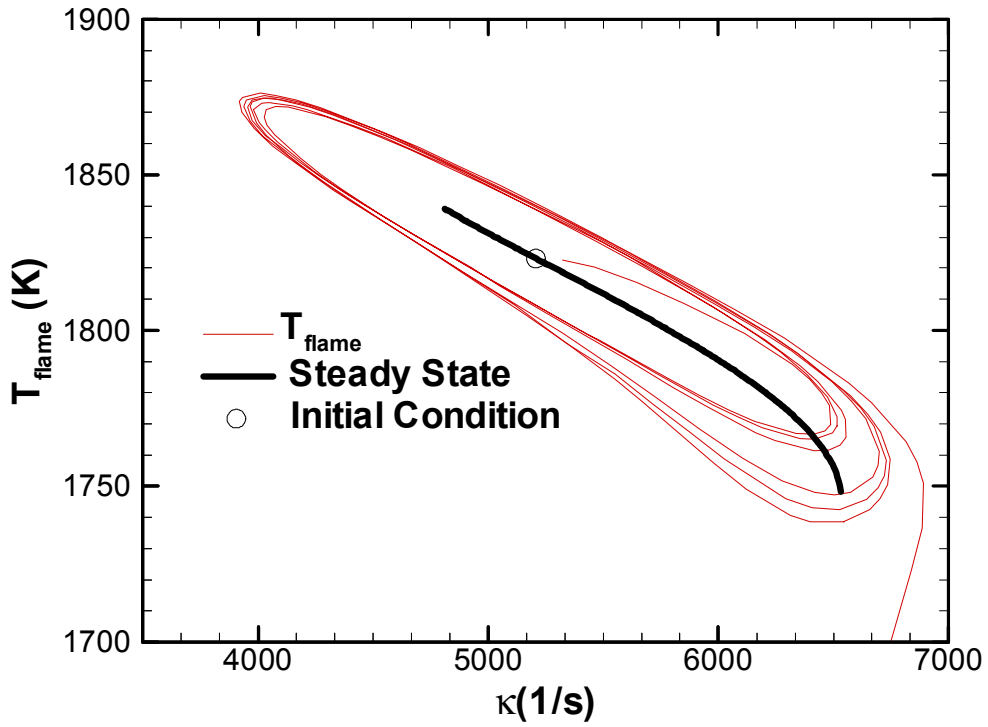

Figure 4.8: Temperature versus strain rate for both the transient oscillations and the steady conditions for the example case of $\phi = 0.75$, $\alpha = 0.05$ $\kappa_{init}/\kappa_{ext} = 0.8$ and $f = 400$Hz.

The numerical model also returns information concerning the variation of species mass fraction. Figure 4.9 is a plot of Y_{CH4} and Y_{CO} at the stagnation plane as functions of strain rate. Again, the steady state values are also plotted for comparison. The initial flame has essentially zero CH_4 remaining at the stagnation plane. As the oscillations are imposed, some CH_4 breaks through the flame up to the stagnation plane. This is an

indication of incomplete combustion. When the flame extinguishes, there is a rapid increase in unburned CH_4. Y_{CO} at the stagnation plane also increases with increasing strain. However, unlike Y_{CH4}, Y_{CO} shows a sharp decrease upon flame extinction. Since CO is generated during by the early combustion reactions, when the flame extinguishes CO generation stops and Y_{CO} drops toward zero.

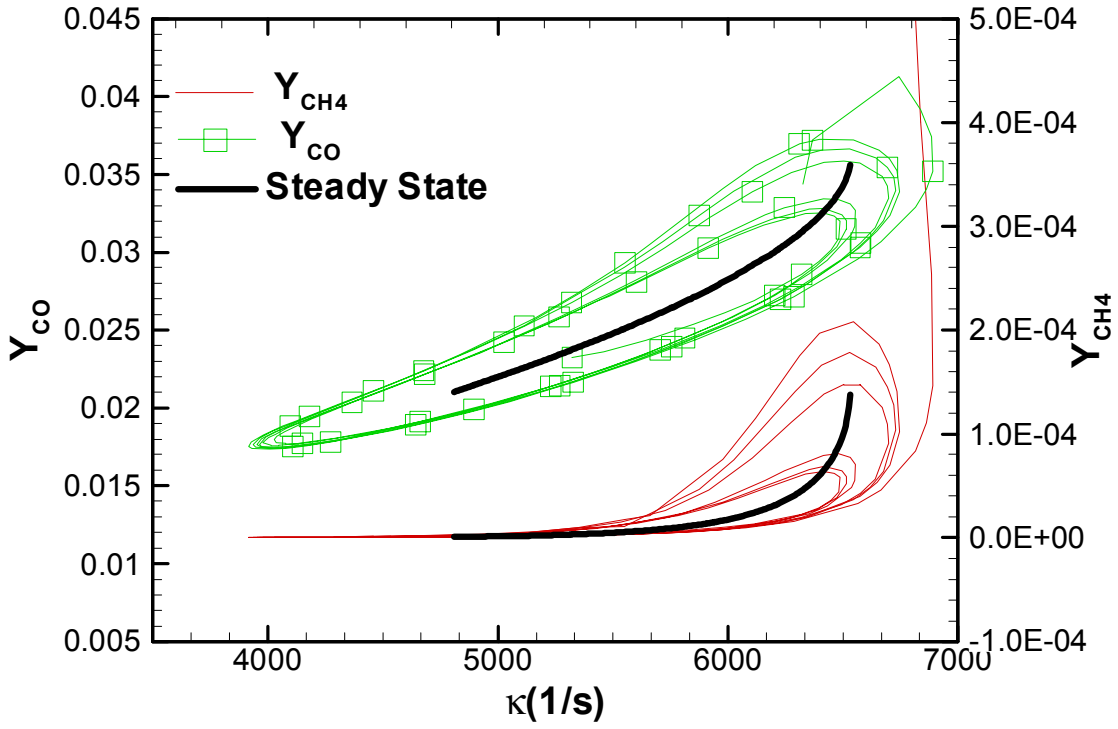

Figure 4.9: Variation of Y_{CO} and Y_{CH4} versus the imposed velocity oscillations compared to the steady state responses for $\phi = 0.75$, $\alpha = 0.05$ $\kappa_{init}/\kappa_{ext} = 0.8$ and $f = 400$Hz.

As discussed previously, the pressure boundary condition used in this modeling effort assumed the transient terms in the Bernoulli equation were negligible. To test this assumption, a test flame with a mixture composition of $\phi = 0.75$, $\alpha = 0.05$ was used in calculations with both the simplified pressure boundary condition presented in this

chapter and a boundary condition which included the transient terms. The initial flame was at a relative strain rate of $\kappa_{init}/\kappa_{ext} = 0.8$ and was oscillated at 100Hz and 1000Hz. The results of this comparison can be seen in Figure 4.10 and Figure 4.11. The computed centerline pressure variations do show changes between the two boundary conditions. At 100Hz, Figure 4.10, including the transient terms leads to a larger variation in the pressure at the centerline throughout the cycle, though the mean pressure values are identical. Furthermore, there is a difference in phase between the two centerline pressures. At 1000Hz, Figure 4.11, the pressure variations are almost identical in magnitude but the phase difference remains. However, the important observation is that for both frequencies, the variation in U_{in} and T_{flame} are identical. Therefore, it may be concluded that neglecting the transient terms in the pressure boundary condition will have a negligible effect on the computational results of T_{flame} and extinction amplitude predictions.

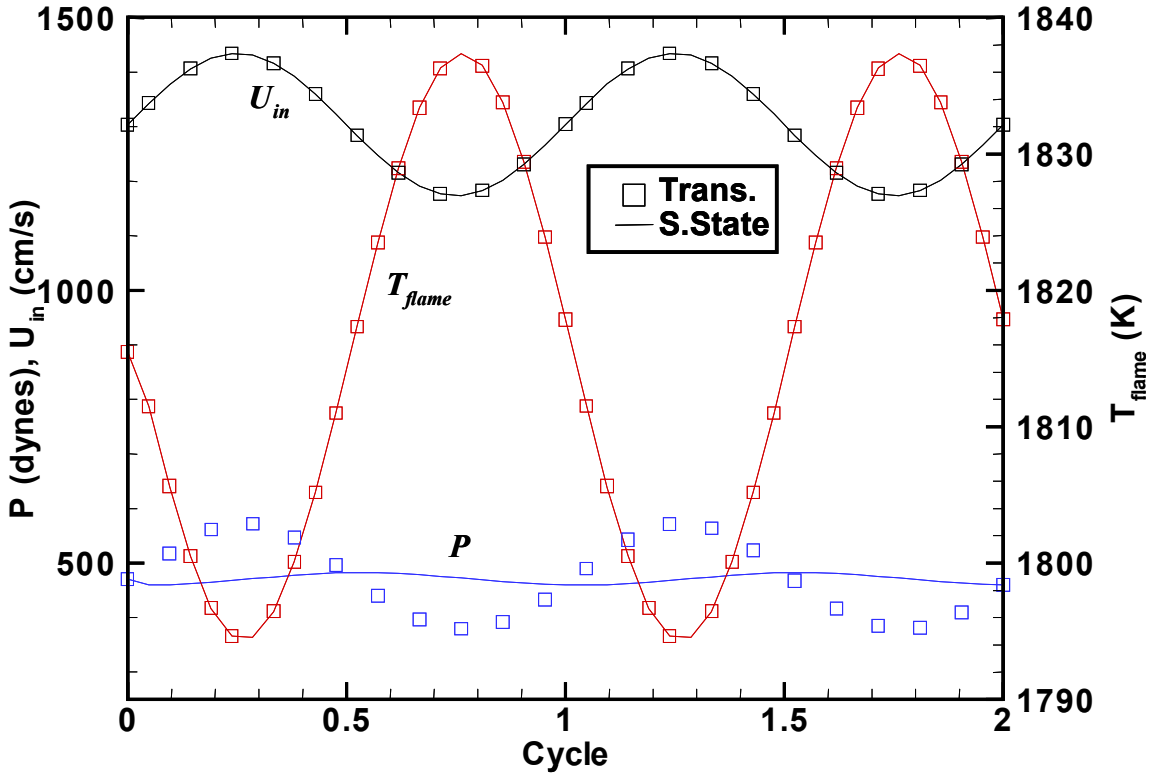

Figure 4.10: Comparison of centerline pressure, U_{in} and T_{flame} for a $\phi = 0.75$, $\alpha = 0.05$, $k_{init}/k_{ext} = 0.8$ flame oscillated at $f = 100$Hz and $A = 0.1$ computed using both pressure boundary conditions.

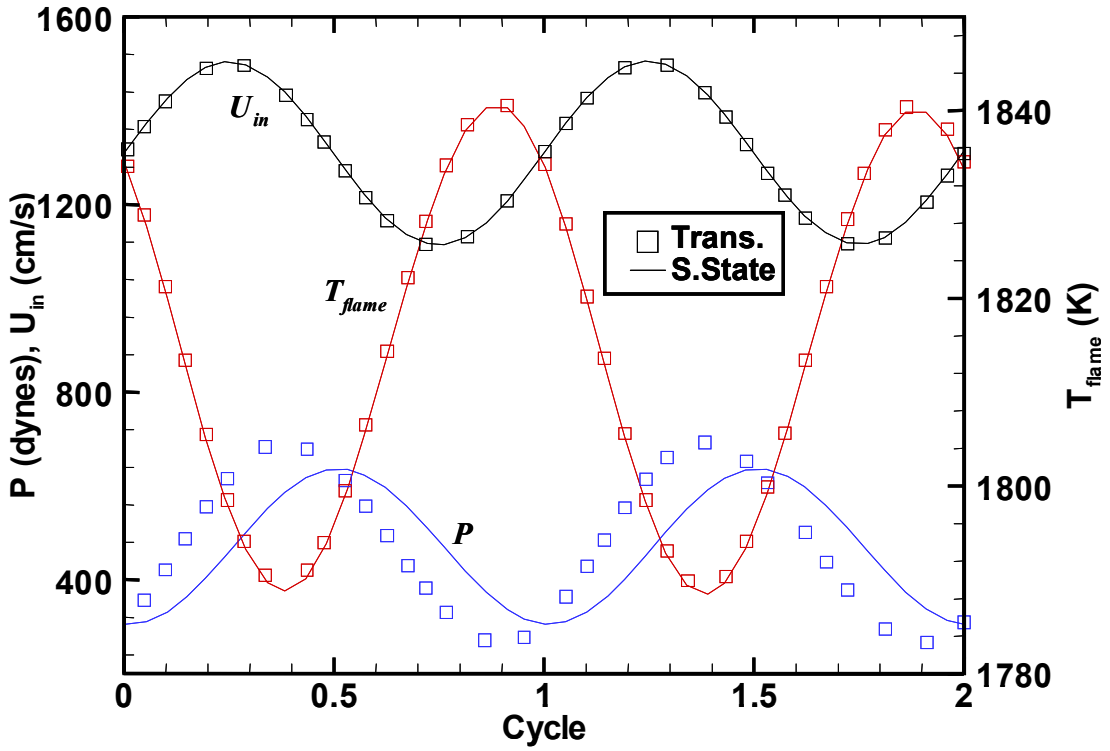

Figure 4.11: Comparison of centerline pressure, U_{in} and T_{flame} for a $\phi = 0.75$, $\alpha = 0.05$, $k_{init}/k_{ext} = 0.8$ flame oscillated at $f = 1000$Hz and $A = 0.15$ computed using both pressure boundary conditions.

4.7 Conclusion

The transient combustion computational model described in the preceding sections simulates one-dimensional counterflow flames. The small domain of the model, a one-dimensional region along the centerline between two opposed nozzles, allows the inclusion of detailed thermodynamics, chemical kinetics and multicomponent diffusion velocities. The detailed results of the code allow the investigation of flame properties such as species mass fractions, flame temperature and global strain rate. The transient nature of the code allows oscillations in the form of a sine wave to be imposed on the boundary conditions. The frequency and amplitude of the oscillations can be modified to

simulate oscillatory conditions relevant to gas turbine combustor design as well as turbulent combustion investigations.

The example results above illustrate some of the complex responses of lean premixed flames to oscillating conditions. The following chapter presents the results of a more complete investigation of these phenomena.

Chapter 5 Transient Modeling Results

5.1 Introduction

The numerical results presented in this chapter were generated using the techniques described in the previous chapter. The computational code TREC was used to investigate the effects of strain rate oscillations on counterflow, lean, premixed hydrocarbon flames. Reactant mixtures of CH_4-air are studied as well as reactant compositions with H_2 added. H_2 doping provides stability benefits under steady state conditions, and this study will investigate the effects of H_2 addition under transient conditions. Counterflow flames with reactant compositions of $\phi = 0.75$ and 0.5 with $\alpha =$ 0.0, 0.05 and 0.10 are used to investigate how flame response is modified by H_2 addition. Also, since $\phi = 0.5$ flames are close to the lean extinction limit and $\phi = 0.75$ are not, comparing the results from the two equivalence ratios demonstrates how flame responses may differ depending on relative flame strength. The results present the macro-scale effects, such as flame temperature, extinction and pollutant production, of strain rate oscillations upon the flame and how the use of multi-component fuels modifies these effects. The computational model will impose velocity oscillations, and their corresponding pressure oscillations, on the counterflow boundaries at frequencies of 100, 200, 400 and 1000Hz. The interactions between the oscillation timescale and the flame timescale create variations in flame response with frequency. This frequency range was selected to provide a broad spectrum of flame behavior and for its similarity to oscillations in physical systems, as described earlier.

To facilitate the comparison of the results from flames of different composition, Table 5.1 was compiled with data on the flame characteristics of the initial flames. It can be seen that the *Ka* of the flames are all greater than 0.1, so the strain rate imposed on the initial flames put the flame response well beyond the linear region modeled in the integral analyses chapters. The inverse of the relative flame timescale ($1/\tau$) is computed from the stretched flame speed divided by the flame thickness, and is provided for comparisons between flames and comparisons to the frequency of the imposed oscillations. It should be noted while the values shown are much higher than the highest imposed frequency of 1000Hz, the flame timescale calculation is based on flame properties at a single standard location assumed to be representative of the flame structure. Choosing slightly a different location within the flame would provide different properties and a different timescale value. Therefore, the values shown may be used for relative comparisons.

Table 5.1: Properties of each initial flame used in the transient computational study.

ϕ	α	$\kappa_{init}/\kappa_{ext}$	κ_{ext} (1/s)	*Ka*	S^0_{flame} (cm/s)	S_{flame} (cm/s)	Flame Thickness (cm)	$1/\tau$ (1/s)
0.50	0.00	95%	1130	0.483	40	95.7	1.71E-02	5596
		90%	1130	0.483	40	93.5	1.71E-02	5468
		80%	1130	0.483	40	89.3	1.71E-02	5222
	0.05	95%	2010	0.567	50	130.7	1.41E-02	9270
		90%	2010	0.567	50	128.2	1.41E-02	9092
		80%	2010	0.567	50	122.4	1.41E-02	8681
	0.10	95%	3270	0.659	60	168.8	1.21E-02	13950
		90%	3270	0.659	60	164.7	1.21E-02	13612
		80%	3270	0.659	60	155.8	1.21E-02	12876
0.75	0.00	95%	4640	0.288	105	200.1	6.51E-03	30737
		90%	4640	0.288	105	197.3	6.51E-03	30307
		80%	4640	0.288	105	189.9	6.51E-03	29171
	0.05	95%	6540	0.325	120	241.4	5.60E-03	43138
		90%	6540	0.325	120	236.8	5.60E-03	42316
		80%	6540	0.325	120	226.2	5.60E-03	40422
	0.10	95%	8830	0.361	135	283.1	5.52E-03	51286
		90%	8830	0.361	135	278.1	5.52E-03	50380
		80%	8830	0.361	135	266.1	5.52E-03	48207

5.2 Effects of Frequency

5.2.1 Temperature

The variation of flame temperature, T_{flame}, in response to oscillations for a reactant mixture of CH_4-air is investigated first. Figure 5.1 is a plot of the T_{flame} response of a ϕ = 0.5, α = 0.0 flame with an initial strain rate of $\kappa_{init}/\kappa_{ext}$ = 0.8, exposed to oscillations at each frequency level. Each curve shows the flame temperature response over several cycles at the amplitude just prior to the extinction amplitude, A_{ext-1}, for the given frequency. As can be seen, increasing the oscillation frequency increases the variation from the steady state conditions for the instantaneous κ. The 1000Hz curve is an ellipse almost normal to the steady state curve. All the flames persist for portions of the cycle that are beyond the steady state extinction temperature.

In Figure 5.1, the flame response for the 100 and 200Hz oscillations vary about the initial flame position. The imposed oscillations always vary about the initial inlet velocity, so the initial velocity is the same as the mean velocity. For the low frequency cases, the relationship between imposed strain and inlet velocity is essential linear. Therefore, because the mean of the inlet velocity is the same as the initial velocity, κ_{mean} is equal to κ_{init}. However, for the 400 and 1000Hz cases, the relation between inlet velocity and κ exhibits increasing non-linearity with increasing frequency. Even though the mean inlet velocity is still the same as the initial inlet velocity, κ_{mean} is not necessarily κ_{ext}. For this reason, the oscillating results shown here will be reported as $\kappa_{init}/\kappa_{ext}$.

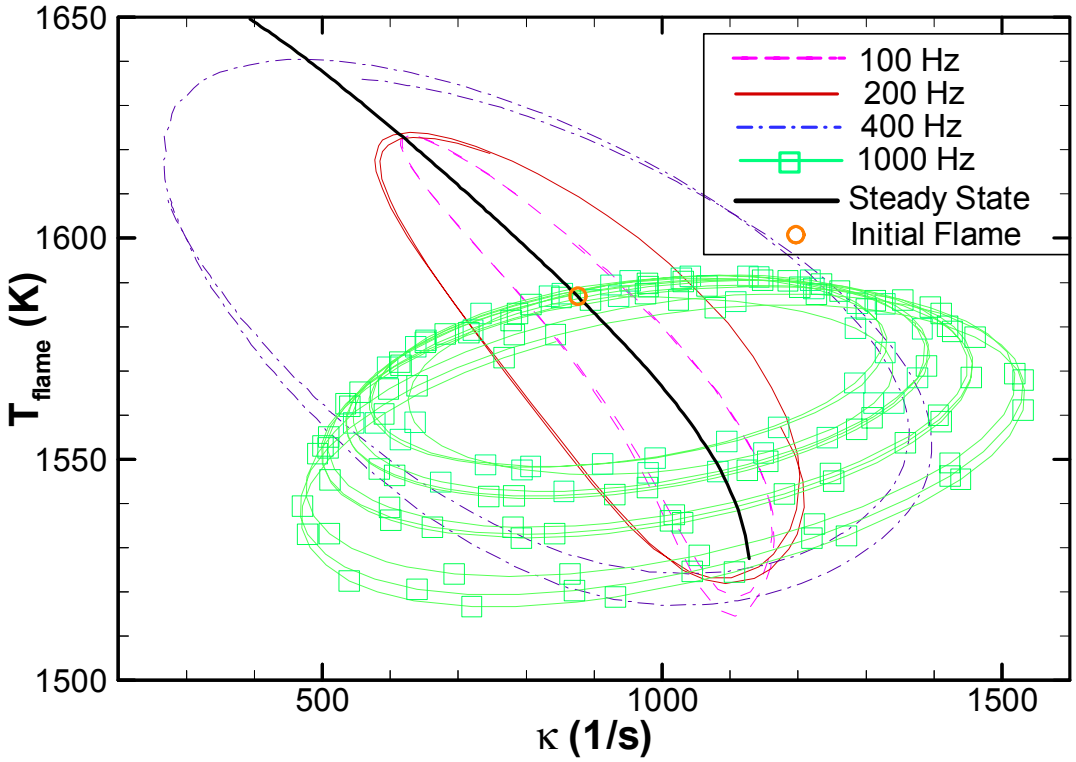

Figure 5.1: Temperature versus strain for several frequencies for $\phi = 0.5$, $\alpha = 0.0$ and $\kappa_{init}/\kappa_{ext} = 0.8$ and the steady state response.

Figure 5.2 shows similar results for $\phi = 0.75$, $\alpha = 0.0$, $\kappa_{init}/\kappa_{ext} = 0.8$ case. Even though the flames in Figure 5.1 and Figure 5.2 are both at $\kappa_{init}/\kappa_{ext} = 0.80$, the absolute magnitude of the imposed oscillations is greater for the $\phi = 0.75$ flame since the κ_{ext} is 4644 1/s versus 1128 1/s for the $\phi = 0.50$ flame. There is a general trend of increased variation from steady state with increased frequency, with the 1000Hz case able to withstand large amplitudes and large changes in strain rate without extinguishing. For this equivalence ratio, only the 1000Hz oscillations are able to drive the flame below the steady state extinction temperature without extinguishing the flame. It can be seen that even for the 1000Hz case, T_{flame} remains above the extinction temperature for the

majority of the cycle. This may allow the flame to recover from its brief excursions beyond the steady state extinction limits.

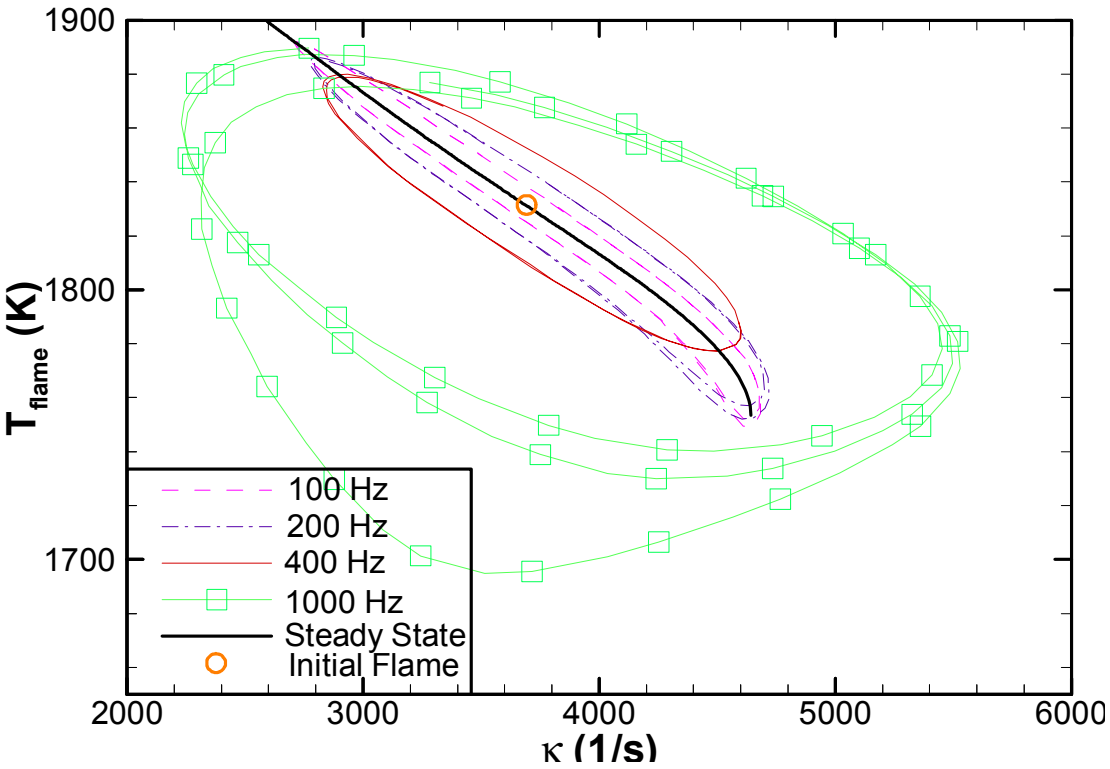

Figure 5.2: Temperature versus strain at several frequencies for $\phi = 0.75$, $\alpha = 0.0$ and $\kappa_{init}/\kappa_{ext} = 0.8$ and the steady state response.

In Figure 5.3 the temperature variations for 100Hz velocity oscillations are plotted versus the scaled strain rate κ/κ_{ext}. This allows for easier comparisons of property variations between different flames. The $\phi = 0.5$ flame exhibits larger variations from steady state before extinction, even though the magnitude of the $\phi = 0.75$ oscillations are larger. This again indicates that the $\phi = 0.5$ flame is more susceptible to the oscillations due to its weaker initial condition. The higher initial T_{flame} for the $\phi = 0.75$ flame causes

faster chemical kinetics, which allowing the flame to respond to the oscillations faster than the $\phi = 0.5$ flame with a lower initial T_{flame}.

Finally, steady state flames of a given ϕ extinguish at similar T_{flame}. While it easily seen that oscillations allow the flame to persist with the T_{flame} momentarily below the T_{ext}, a notable result is that the magnitude maximum difference between T_{ext} and the instantaneous T_{flame} varies with the velocity oscillation frequency.

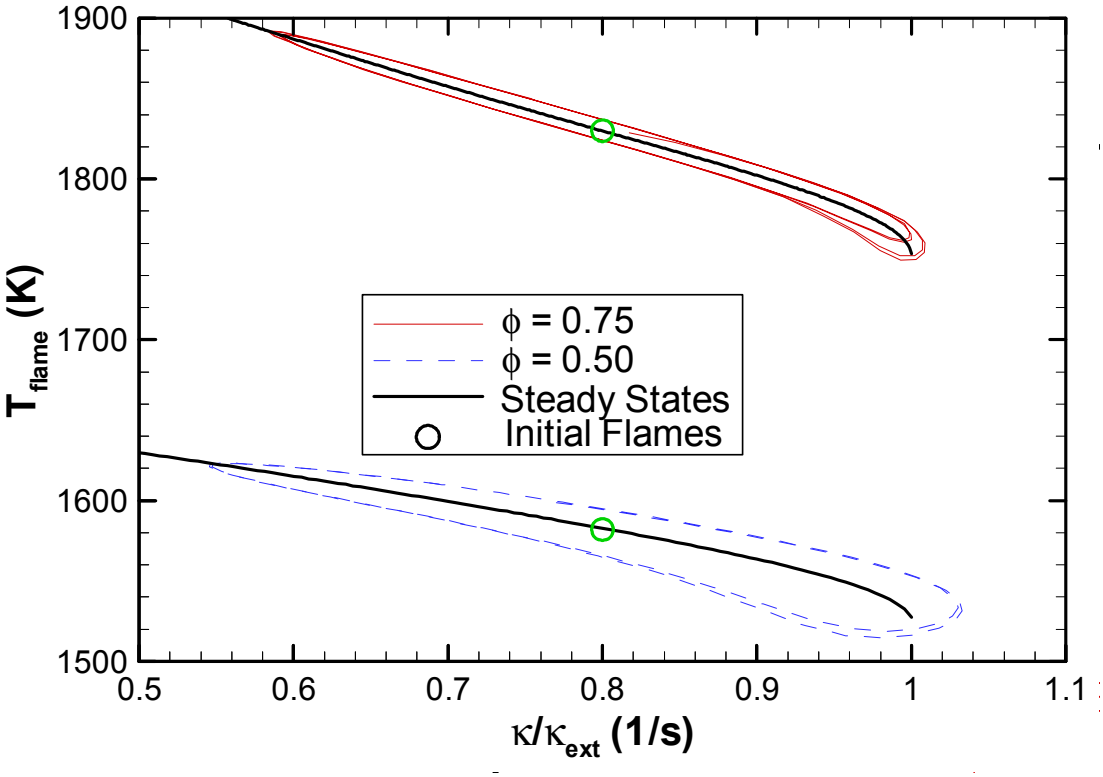

Figure 5.3: Temperature versus κ/κ_{ext} for $\alpha = 0$ and both $\phi = 0.5$ and 0.75 oscillated at 200Hz and $A_{ext\text{-}1}$.

5.2.2 Mass fractions

Figure 5.4 and Figure 5.5 show the mass fractions of CO, CH_4 and NO at the counterflow stagnation plane for $\phi = 0.5$ and $\phi = 0.75$ flames, respectively. These three species were investigated as indicators of flame conditions. Increasing Y_{CH4} at the stagnation plane indicates a decrease in combustion efficiency. Y_{CO} and Y_{NO} indicate the production of pollutants in the combustion process and are of interest in combustion applications. Curves are plotted for both 200 and 400Hz oscillations. Figure 5.4 shows that the mass fraction variations momentarily exceed the values at the steady state extinction limit during the peak strain portion of the imposed oscillations. Furthermore, the magnitude the mass fractions exceed the steady state limits is generally greater for the 200Hz oscillations than for the 400Hz oscillations. The higher frequency oscillations cause wider variations from the steady state values throughout the cycle, but the maximum values do not go far beyond the steady state extinction limit. The exception to this is Y_{CH4} at 400Hz for the $\phi = 0.50$ flame. It is theorized that for this case the oscillation amplitude was closer to A_{ext} than the other cases shown, so Y_{CH4} is exhibiting a sharp near-extinction increase in unburned CH_4. The increase in unburned CH_4 shows a decrease in combustion efficiency under oscillations. While there is a large variation in Y_{CH4}, Y_{CO} varies less from the steady state results. The large increase in Y_{CH4} as the flame moves beyond κ_{ext}, indicates the rapid decrease CH_4 oxidation reactions during this time. The smaller variation in Y_{CO} indicates that the late reactions consuming CO are less affected by the oscillations and are still occurring at rates similar to the steady state flame.

Figure 5.5 shows similar results, though once again the $\phi = 0.75$ flame exhibits less variation from steady state than the weaker $\phi = 0.5$ flame shown in Figure 5.4. Figure 5.5 also shows the mass fraction behavior at extinction. At the extinction point, Y_{CH4} increases sharply to reach the inlet value. Y_{NO} drops towards zero as the temperatures are no longer high enough to support the reactions producing NO. Y_{CO} initially increases as the flame extinguishes and the flame combustion efficiency drops, and then decreases towards zero as the CO producing reactions stop. A further indicator of the relatively limited response of the CO consuming reactions to the imposed oscillations is that Y_{CO} does not exceed the steady state values until flame extinction occurs, while Y_{CH4} exceeds the steady state even at an amplitude at which the flame sustains itself.

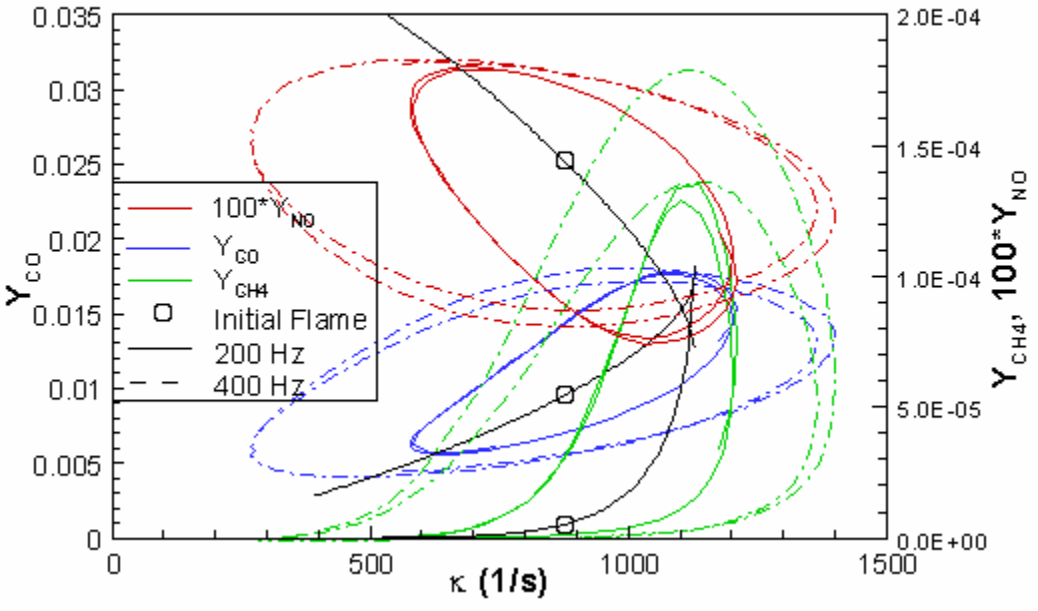

Figure 5.4: Species mass fractions versus strain rate for $\phi = 0.5$, $\alpha = 0.0$, $\kappa_{init}/\kappa_{ext} = 0.8$ oscillated at $f = 200$ and 400Hz.

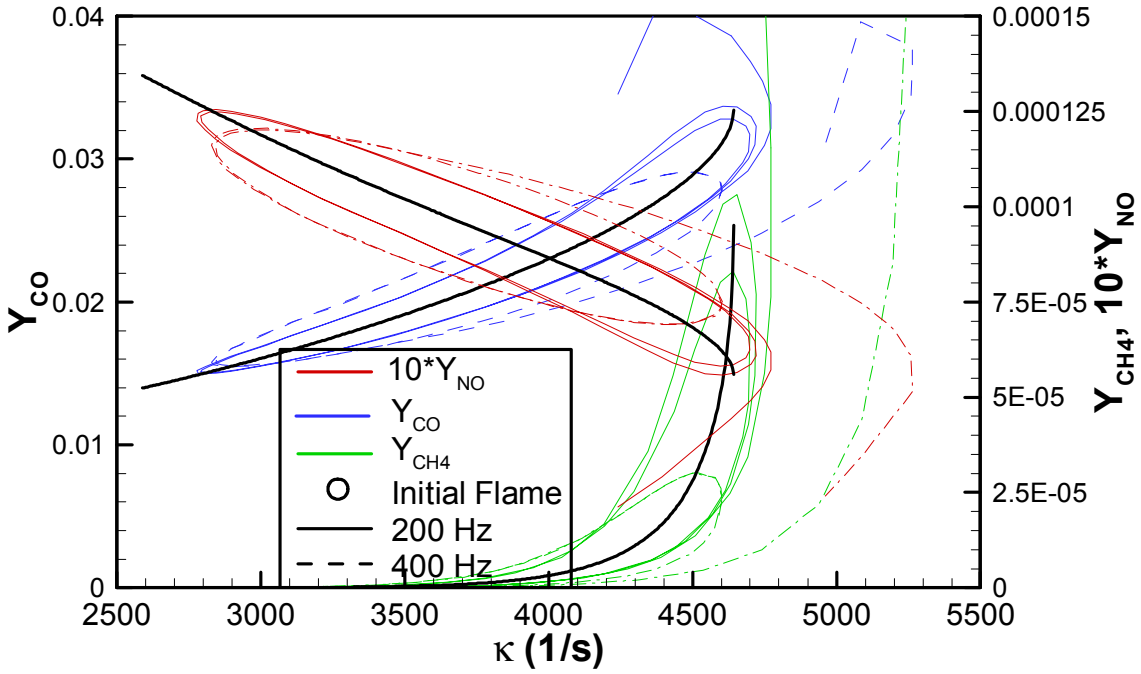

Figure 5.5: Species mass fractions versus strain for $\phi = 0.75$, $\alpha = 0.0$, $\kappa_{init}/\kappa_{ext} = 0.8$ oscillated at $f = 200$ and 400Hz.

5.2.3 Flame motion

Another interesting feature of the flame response to oscillations is flame position. A counterflow flame is free to move within the flow field to adjust to changes in imposed strain. Figure 5.6 is a plot of the flame position versus strain rate for all four frequencies at $A_{ext\text{-}1}$. The flame position is determined as the location of the largest temperature gradient. It can be seen that the 100 and 200Hz oscillations cause the flame zone to move a similar magnitude, while the 400Hz oscillations cause larger oscillations of flame position. However, for the 1000Hz flame moves less than the other frequencies while the center of motion is closer to the stagnation plane than for the initial steady state case.

These results point to two aspects of the 1000Hz case. First, the 1000Hz oscillations at the high amplitude seem to cause the flame to oscillate about a weaker mean flame value compared to the initial flame. Second, the timescale of the imposed oscillations are now on the same order of the flame timescales, so the flame cannot adjust to the varying flow field as easily as it can at the lower frequencies.

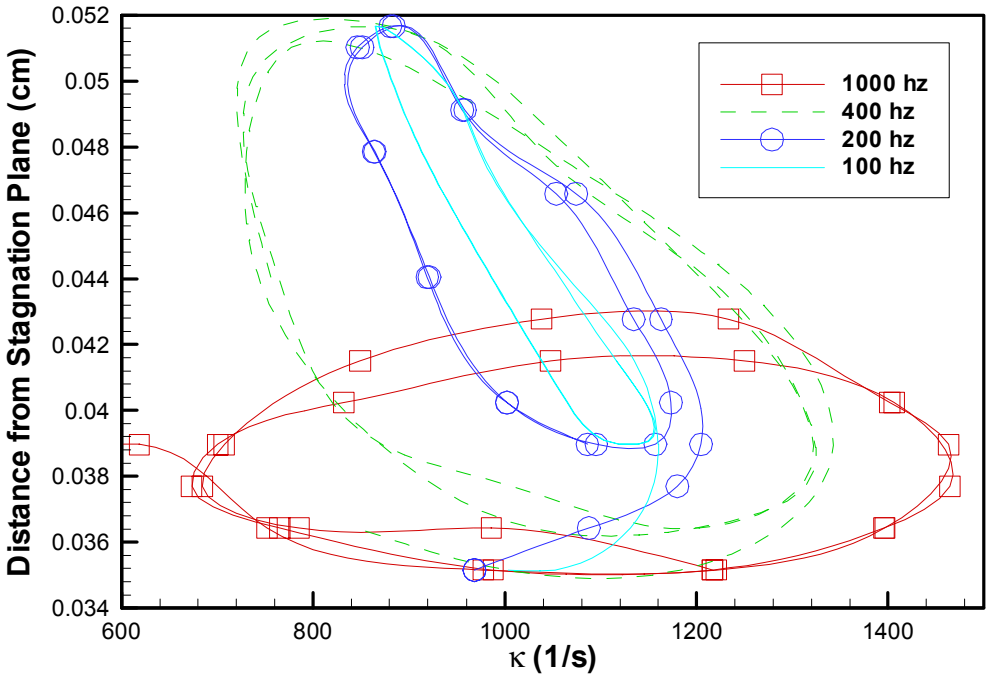

Figure 5.6: Flame position versus strain for $\phi = 0.5$, $\alpha = 0.0$, $\kappa_{init}/\kappa_{ext} = 0.9$ for four frequencies.

5.3 Effects of Initial $\kappa_{init}/\kappa_{ext}$

5.3.1 Temperature

The effect of the initial flame's strain rate, κ_{init}, on the flame response to oscillations was also investigated. A flame's κ_{init} was scaled by the steady state

extinction strain rate, κ_{ext}, for that particular reactant composition. The scaled value $\kappa_{init}/\kappa_{ext}$ allowed the comparison of several different initial flames. It was anticipated that flames with $\kappa_{init}/\kappa_{ext}$ near 1.0, would be more susceptible to imposed oscillations than flames with lower $\kappa_{init}/\kappa_{ext}$.

Figure 5.7 shows the temperature response of a $\phi = 0.5$, $\alpha = 0.0$ flame subject to 200Hz oscillations. The three curves are for the three initial flame strain rates of $\kappa_{init}/\kappa_{ext}$ = 0.8, 0.9 and 0.95. Again, only the cycles of amplitude $A_{ext\text{-}1}$ are plotted. The curves show that the flame properties tend to oscillate about the initial, mean flame temperature. With increasing $\kappa_{init}/\kappa_{ext}$, the maximum strain the flame can withstand decreases. Flames starting further from the steady state extinction strain rate are able to push further beyond this limit. Another notable aspect of Figure 5.7 is that the minimum temperature for the $\kappa_{init}/\kappa_{ext} = 0.95$ case drops significantly below the other cases even with a lower relative strain. The $\kappa_{init}/\kappa_{ext} = 0.95$ case oscillates about a mean temperature less than its initial temperature.

The temperature response for the $\phi = 0.75$ case is shown in Figure 5.8. Compared to the results in Figure 5.7, the variations from steady state are much less for the richer ϕ = 0.75 flame, even though the magnitude of the strain variations are larger than those for $\phi = 0.5$. Furthermore, none of the temperature oscillations are able to go below the steady state extinction temperature.

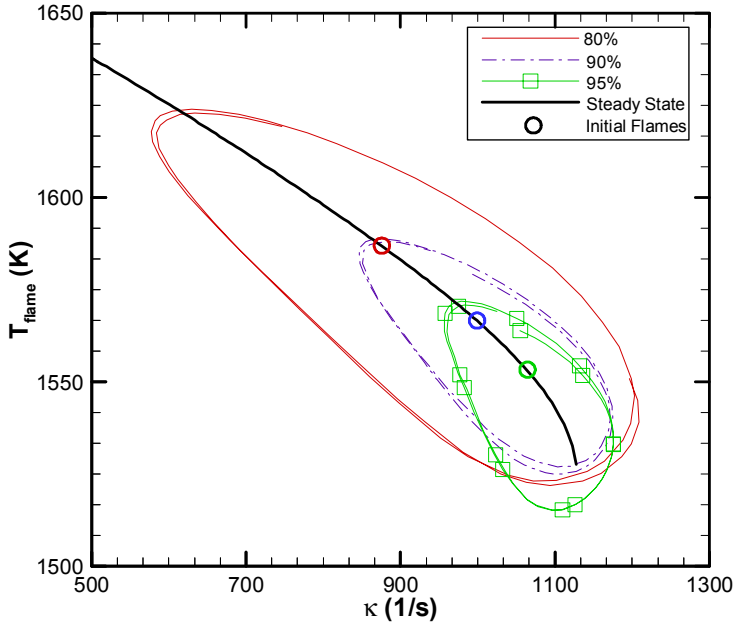

Figure 5.7: Temperature versus strain for three initial strain rates and $\phi = 0.5$, $\alpha = 0.0$ and $f = 200$Hz.

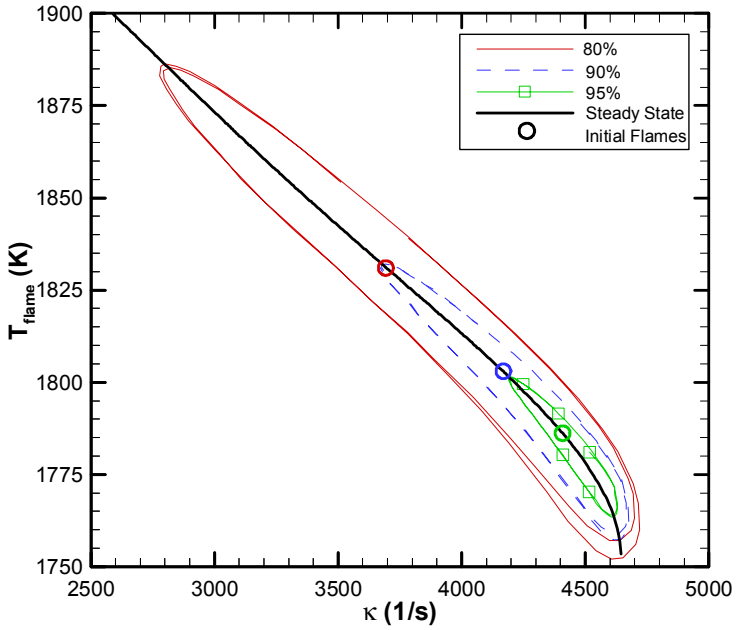

Figure 5.8: Temperature versus strain for three $\kappa_{init}/\kappa_{ext}$ values, $\phi = 0.75$, $\alpha = 0.0$ and $f =$ 200Hz.

5.3.2 Mass fractions

As before, the mass fractions at the stagnation plane were studied to determine the effect of initial strain rate on the flame response to oscillations. In Figure 5.9 Y_{NO}, Y_{CO}, and Y_{CH4} at the stagnation plane for a $\phi = 0.75$ flame are plotted for both 200Hz oscillations and steady state responses for $\kappa_{init}/\kappa_{ext} = 0.8$ and 0.95. Like the previous results for mass fractions, only Y_{CH4} goes beyond its respective steady state extinction value. The results for Y_{CH4} exceed the steady state extinction value just prior to extinction, increase to the inlet value upon extinction, and generally show a greater sensitivity to the oscillations than Y_{CO} and Y_{NO}. This is a further indication that CO burnout is less affected by the oscillations as Y_{CH4} increases from increased unburned CH_4 while Y_{CO} remains closer to steady state values. NO formation shows less sensitivity to the oscillations.

The fact that the Y_{CO} seems less sensitive to the oscillations may be due to the fact that the imposed flow field oscillations decrease in magnitude approaching the stagnation plane. The late CO consuming reactions take place closer to the stagnation plane than the earlier CH_4 consuming, chain branching reactions. Therefore, the CO reactions would exhibit less variation. Another possible explanation is that increasing strain inhibits the breakdown of CH_4, producing less CO, so the CO consuming reactions may be inhibited as well, but plotting Y_{CO} merely shows the decrease in CO production earlier in the flame zone.

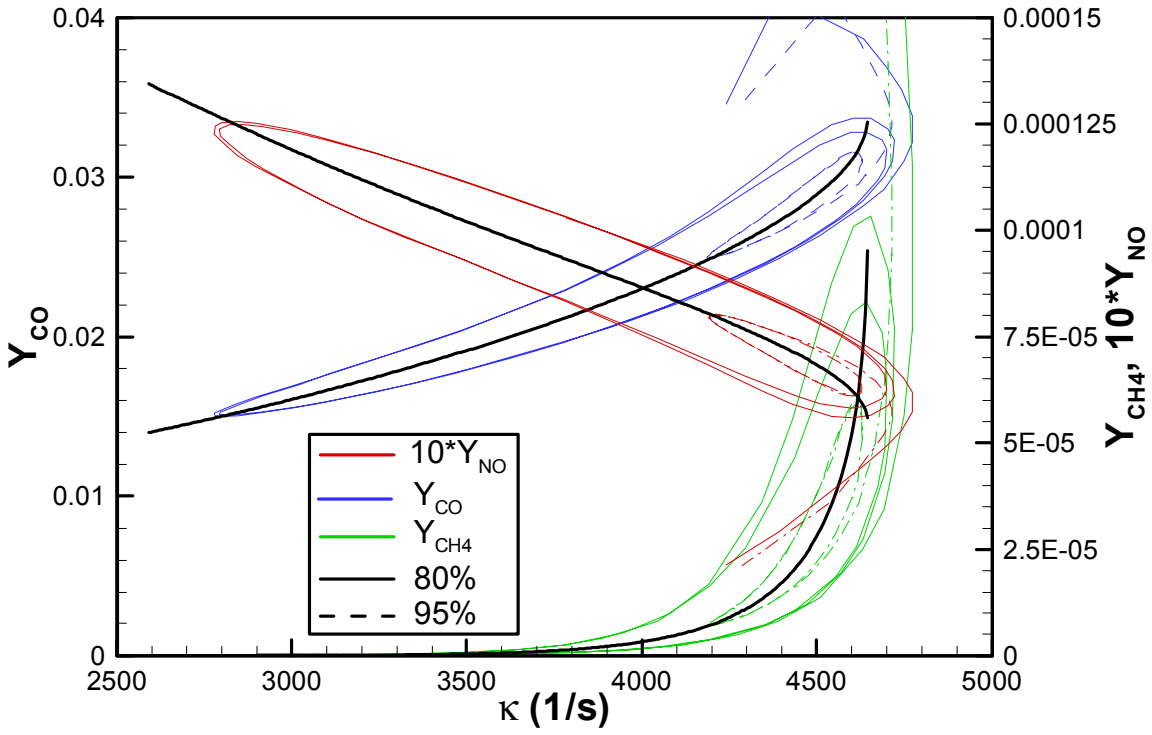

Figure 5.9: Species mass fractions versus strain for two initial strain rates, $\phi = 0.75$, $\alpha = 0.0$ and $f = 200$Hz.

5.3.3 Flame motion

The flame motion for a $\phi = 0.75$, $\alpha = 0.0$ flame for two initial strain rates and two oscillation frequencies are plotted in Figure 5.10. It can be seen that the flame motion is similar for the two frequencies at the lower initial strain rate, with the higher frequency oscillation simply causing oscillations of larger magnitude. As the initial strain increases, the flame motion becomes very different. When the initial flame is closer to the steady state extinction strain rate, the flame motion becomes more erratic and varies significantly from the steady state results. This is most likely caused by the weakness of the initial flame.

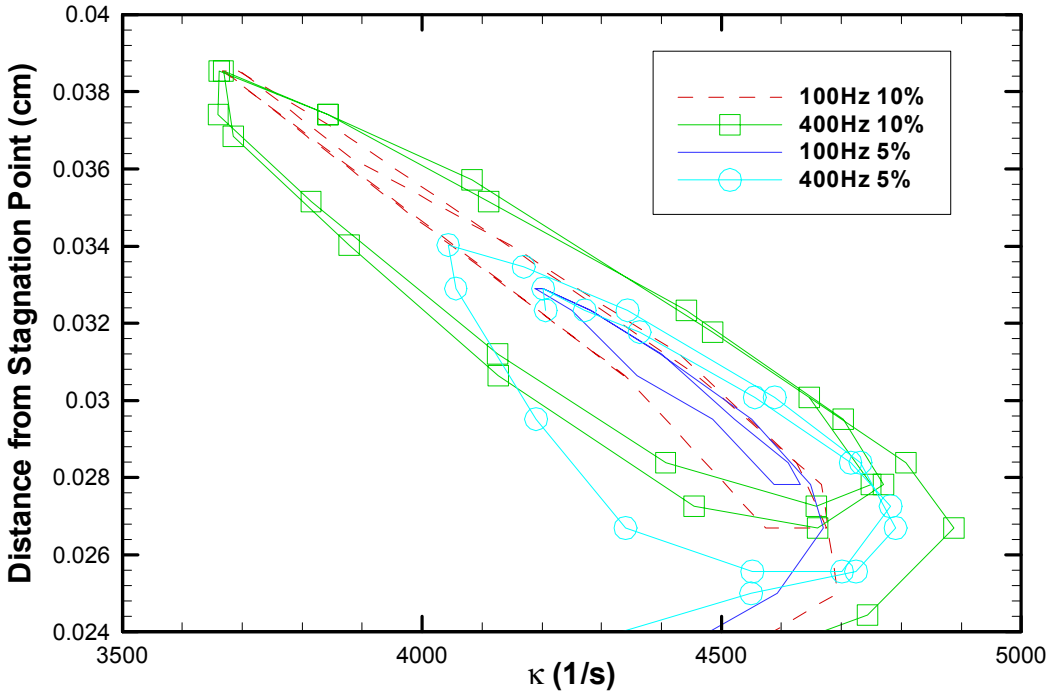

Figure 5.10: Flame position versus strain for $\kappa_{init}/\kappa_{ext} = 0.9$ and 0.95, and $f = 200$ and 400Hz.

5.4 Effects of H_2 Addition

The results presented to this point discussed the response of pure CH_4 flames to strain rate oscillations. The following results discuss how the addition of H_2 to the fuel alters the response to oscillations. Based on the effects of H_2 addition to flame stability in steady state cases, it was assumed that the H_2 would significantly affect the flames transient response.

5.4.1 Temperature

The black curves in Figure 5.11 are the steady state flame temperatures for flames of $\phi = 0.5$, $\alpha = 0.0$, 0.05, 0.10. The cycles plotted are for 400Hz oscillations for each flame starting with $\kappa_{init}/\kappa_{ext} = 0.8$. It can be seen that the steady state extinction occurs at

approximately the same temperature regardless of the amount of H_2 present. Therefore, for this narrow range of mixture fuel compositions, the steady state extinction temperature depends more on equivalence ratio than on fuel composition. The increased diffusion of H_2 into the flame zone contributes to the decrease in magnitude of the steady state slope and the increased reaction rates for H_2 oxidation cause the increase in strain rates for fixed flame temperatures. For all compositions in the figure, increases in the strain rate lead to gradual movement of the flame closer to the stagnation plane, limiting the residence time of the reactants in the flame zone. The relatively faster H_2 combustion process is able to sustain the flame through higher strain rates and smaller flame zones. As the H_2 content increases, higher strain rates are required to extinguish the steady state flame. The decreased slope is also evident for the transient cycles, as the temperature cycles follow the steady state temperature versus strain curves.

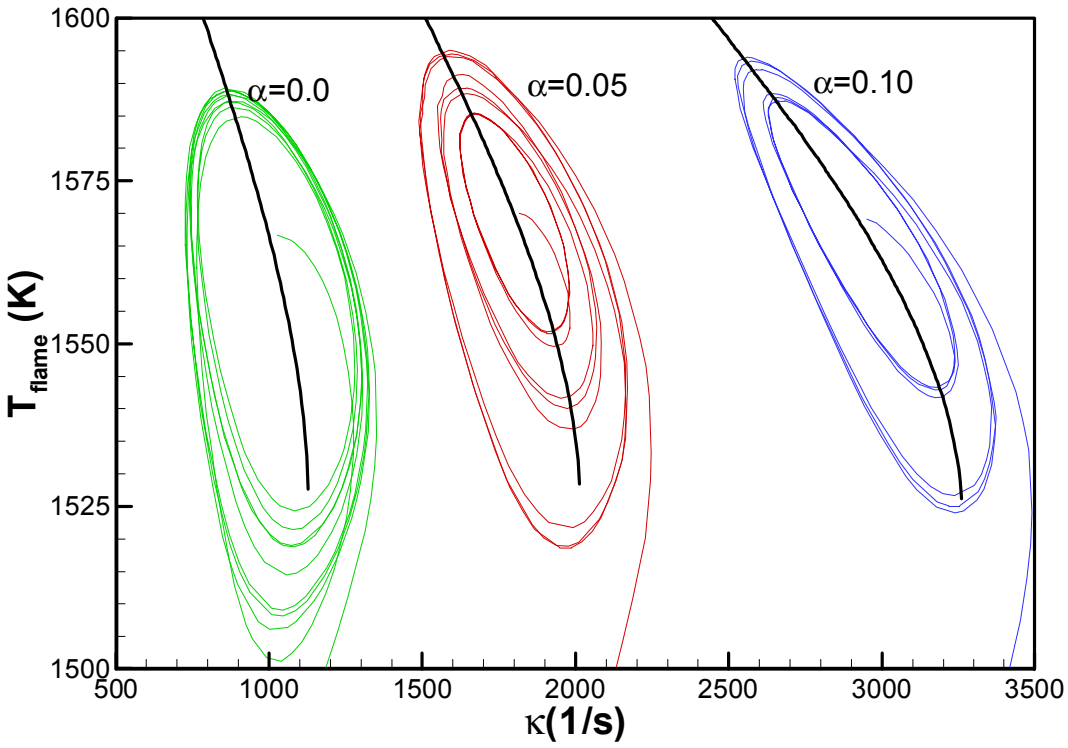

Figure 5.11: Flame temperature versus strain for $\alpha = 0.0$, 0.05, and 0.10 with $\phi = 0.5$, $\kappa_{init}/\kappa_{ext} = 0.8$ and $f = 400$Hz.

Comparing the cycle curves for the three cases shows that the magnitude of the strain rate variation increases with increasing α. This is because higher α cases have larger initial strain rates. Therefore, multiplying the higher initial strain rate by the oscillation amplitude yields a greater total variation in magnitude. However, the variation in temperature decreases with increasing α, because the higher reaction rates with increased H_2 content allow the flame to approach the quasi-steady conditions for a given f more rapidly. This, of course, also explains the more rapid extinction for oscillations beyond the steady state extinction strain rate with increasing α. When $\alpha = 0.10$, the temperature barely drops below the steady state extinction point before the transient flame extinguishes.

Figure 5.12 illustrates the results of H_2 addition to a flame with an initial strain rate closer to extinction. The results in Figure 5.12 are for a $\kappa_{init}/\kappa_{ext} = 0.95$, $\phi = 0.5$ flame with 400Hz oscillations. It can be seen that the variation in temperature with the oscillations again decreases with increasing α, although the difference in less pronounced for this flame. The difference between Figure 5.12 and Figure 5.11 is due to the increase in initial strain rate and the corresponding decrease in initial T_{flame} which makes the $\kappa_{init}/\kappa_{ext} = 0.95$ flames more susceptible to the oscillations.

When the strain rate is oscillated at 1000Hz, the flame temperature does not behave the same as for lower frequencies. Figure 5.13 and Figure 5.14 are plots of the temperature variations for 1000Hz oscillations. Figure 5.13 shows the results for a $\phi = 0.5$, $\kappa_{init}/\kappa_{ext} = 0.8$ and $\alpha = 0.0$, 0.5, 0.10, while Figure 5.14 is for $\phi = 0.75$, $\kappa_{init}/\kappa_{ext} = 0.95$. For both the cases, the plots show that larger oscillations are possible for the $\alpha = 0.10$ case than for the other frequencies. Furthermore, the temperature cycles tend to vary about a temperature less than the initial mean temperature indicating the combustion is persistently weaker than the initial flame at 1000Hz. These changes in flame behavior at 1000Hz indicate the oscillation timescale is now of the same order as the combustion timescale.

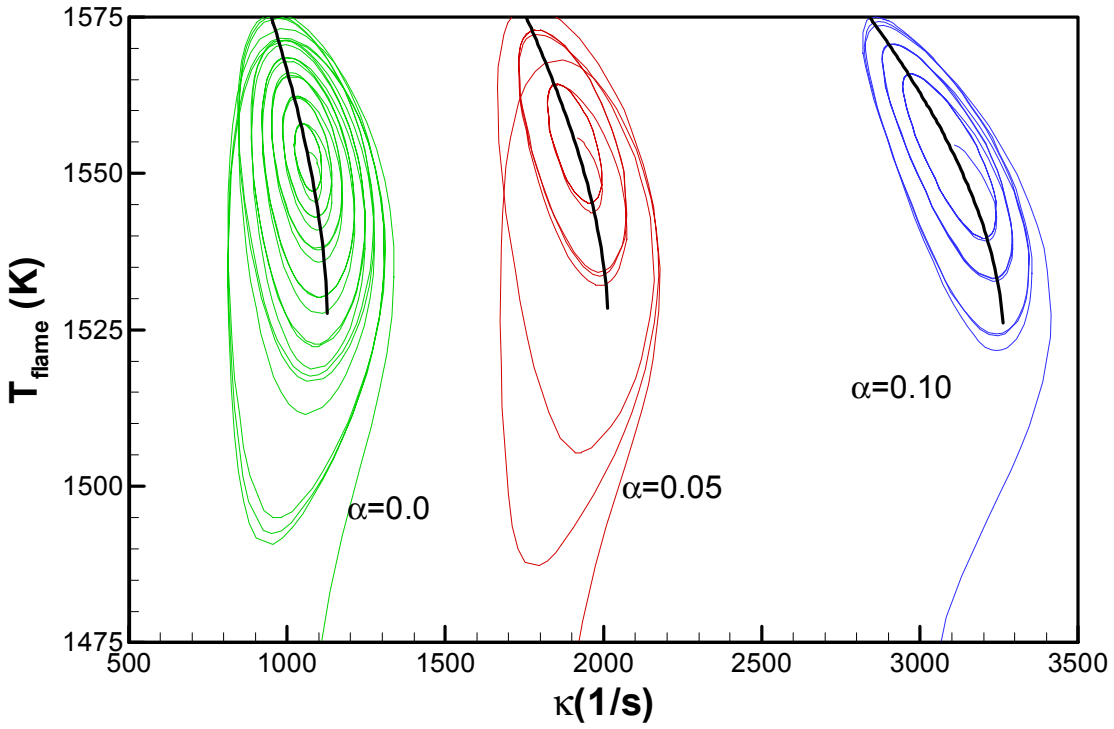

Figure 5.12: Flame temperature versus strain for $\alpha = 0.0$, 0.05 and 0.10, $\phi = 0.5$, $\kappa_{init}/\kappa_{ext} = 0.95$ and $f = 400$Hz.

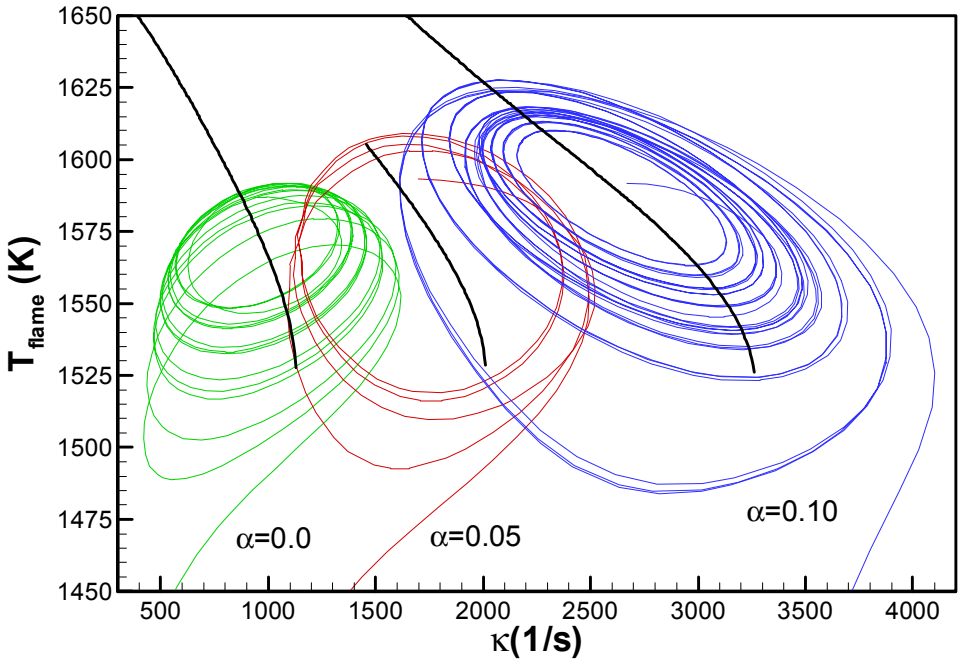

Figure 5.13: Flame temperature versus strain for $\alpha = 0.0$, 0.05, and 0.10, $\phi = 0.5$, $\kappa_{init}/\kappa_{ext}$ = 0.8 and f = 1000Hz.

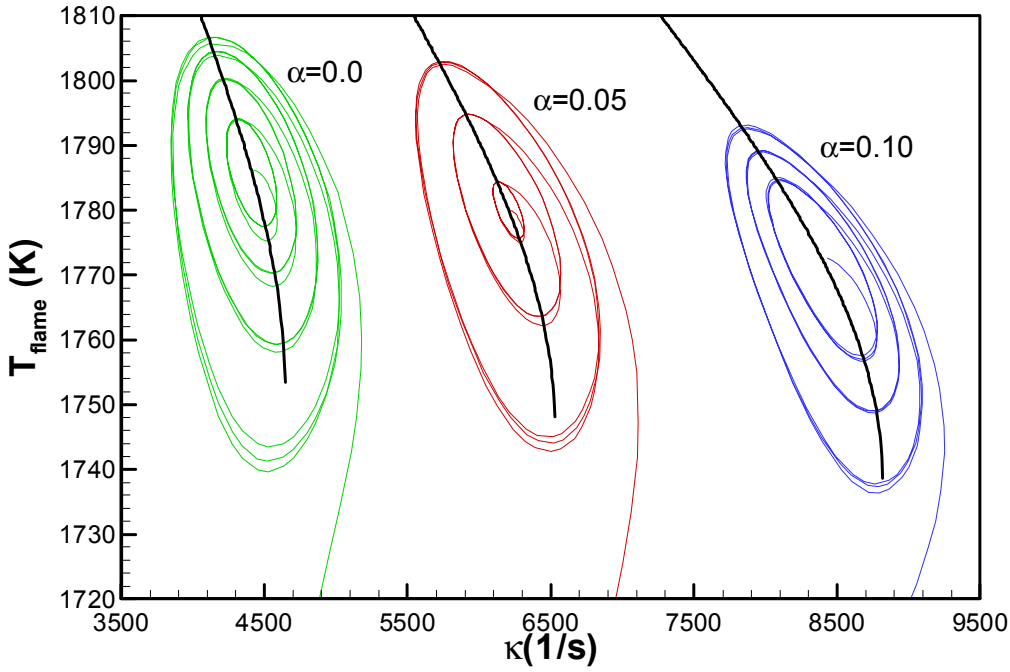

Figure 5.14: Flame temperature versus strain for $\alpha = 0.0$, 0.05, and 0.10, $\phi = 0.75$, $\kappa_{init}/\kappa_{ext}$ = 0.95 and for f = 1000Hz.

5.4.2 Mass fractions

H_2 addition also has an affect on the species mass fractions of CO, CH_4 and NO at the flame stagnation point. Comparing Figure 5.15 with Figure 5.9 shows that the oscillations force much larger variations from steady state for cases with $\alpha = 0.0$. The strain rate variation exhibited in Figure 5.15 is almost twice that in Figure 5.9. However, the magnitude of the mass fraction variations are very similar, with the cycles staying closer to the steady state curves for the $\alpha = 0.10$ case. This shows that the mass fractions are much less susceptible to oscillations with H_2 addition to CH_4 premixed flames. Another similarity between the cases is that only the mass fraction of CH_4 exceeds the steady state limit. H_2 addition does not change this behavior. Furthermore, Y_{CO} again varies less from the steady state curve than Y_{CH4}, supporting the idea that CO burnout reactions are less affected by the oscillations.

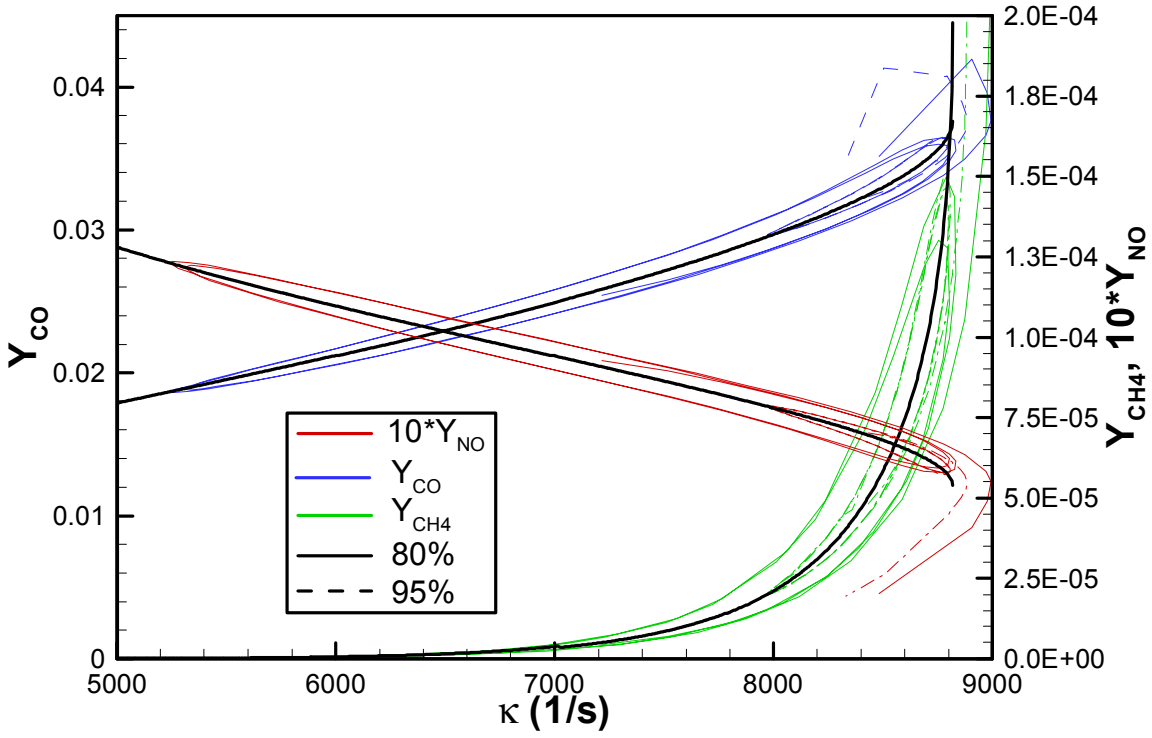

Figure 5.15: Species mass fractions versus strain for $\kappa_{init}/\kappa_{ext} = 0.8$ and 0.95, $\phi = 0.75$, $\alpha = 0.10$ and f = 200Hz.

5.4.3 Flame zone motion

Figure 5.16 is a plot comparing the motion of the flame zone for $\alpha = 0.0$ and $\alpha = 0.1$ with $\phi = 0.75$ subject to 400Hz oscillations. It can be seen that both flame zones move a similar magnitude, but with H_2 the phase lag is less than without H_2. The decrease in the phase lag is evident in the cycle curves staying closer to the steady state flame motion. This shows that the H_2 addition has decreased the flame characteristic timescale, enabling the flame to respond more quickly to the oscillations and follow the quasi-steady state behavior. This behavior indicates that using steady state flamelet theory for modeling turbulent combustion would be a reasonable approximation for

flames with H_2 but may not provide reasonable results for flames which exhibit significant phase lag and significant variation from quasi-steady state values.

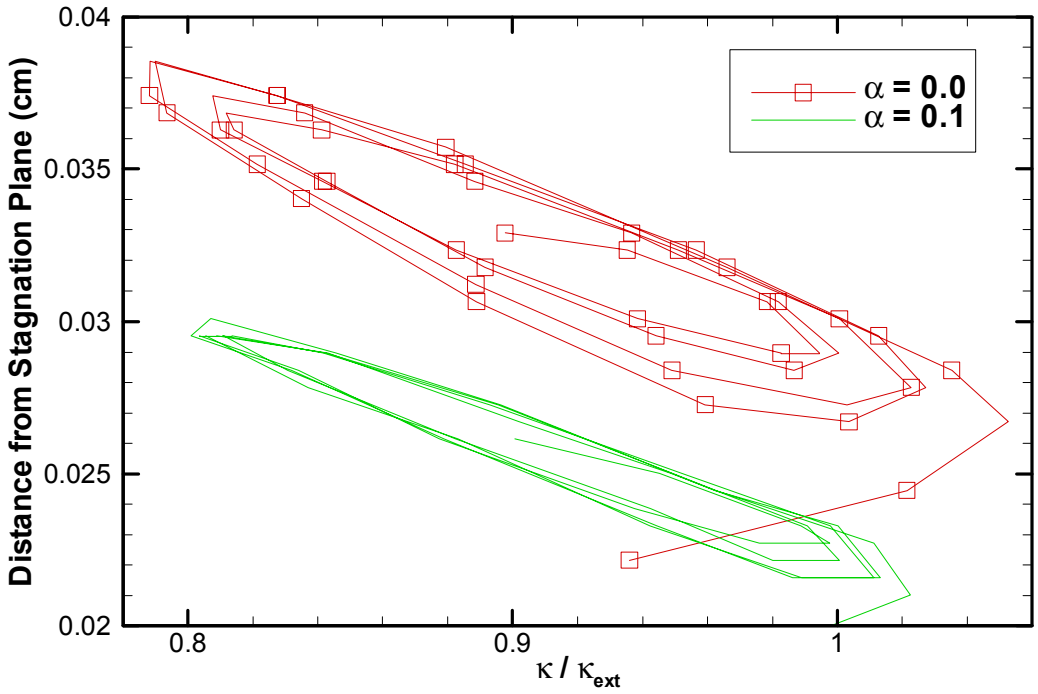

Figure 5.16: Flame position versus κ/κ_{ext} for $\alpha = 0.0$ and 0.10, $\phi = 0.75$, $\kappa_{init}/\kappa_{ext} = 0.9$ and $f = 400$Hz.

5.5 Mass Fraction Profiles

5.5.1 CO burnout

To determine the behavior of CO in the flame zone during oscillations, the species profiles through the flame zone were plotted for two flames. Figure 5.17 shows the temperature and Y_{CO} profiles through the counterflow region for a $\phi = 0.5$, $\alpha = 0.0$, $\kappa_{init}/\kappa_{ext} = 0.9$ flame subject to 200Hz oscillations. Figure 5.18 is a similar plot for a flame with $\alpha = 0.10$. The profiles are plotted at the minimum and maximum strain rates

at the amplitude $A_{ext\text{-}1}$, as well as at A_{ext}. The temperature profiles at the extinction amplitude, A_{ext}, are below the minimum temperature profile at $A_{ext\text{-}1}$ for both cases, which is as expected. The temperature at extinction should be lower than the temperature during a cycle that does not cause extinction.

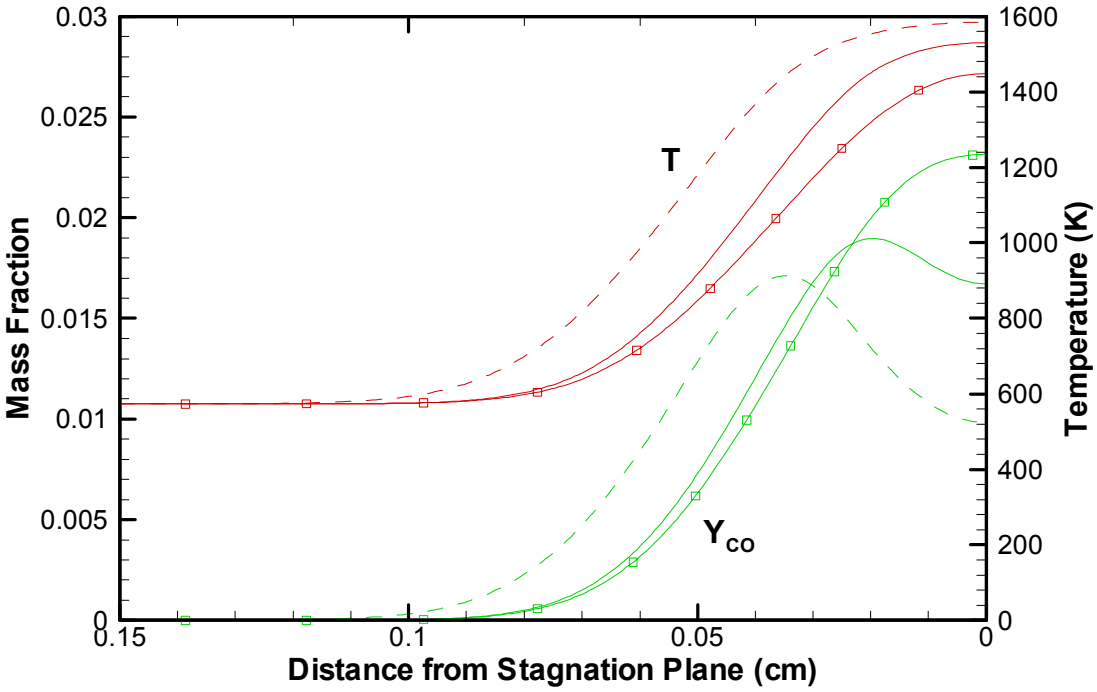

Figure 5.17: Temperature and Y_{CO} versus distance from the stagnation plane for $\phi = 0.5$, $\alpha = 0$, $\kappa_{init}/\kappa_{ext} = 0.9$ and $f = 200$Hz.

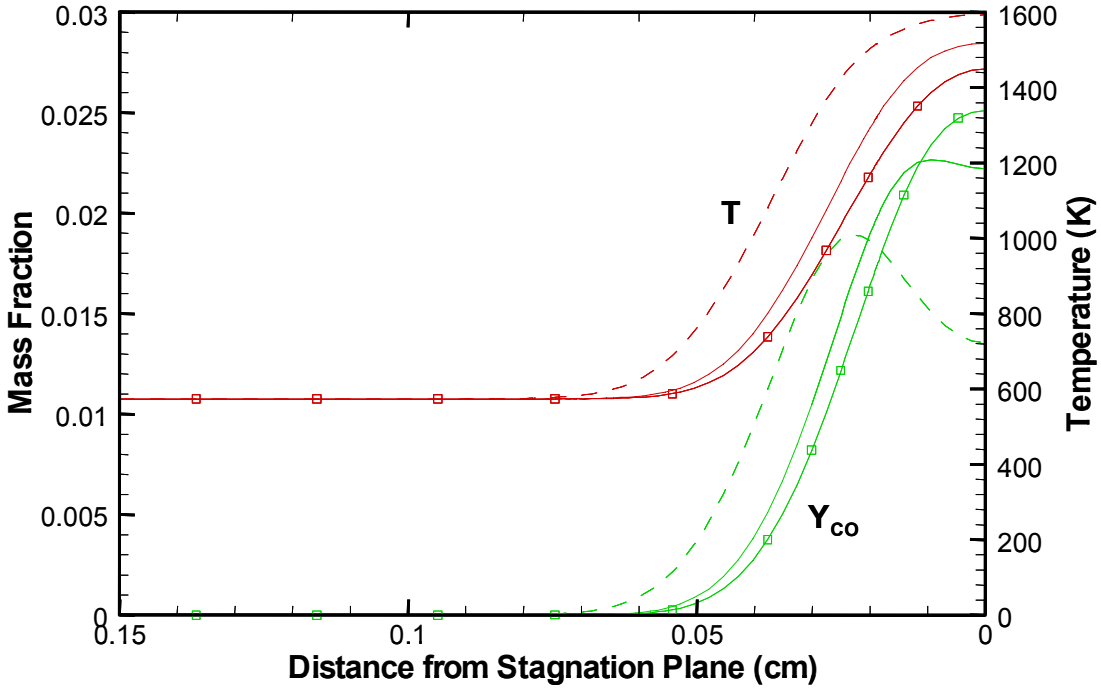

Figure 5.18: Temperature and Y_{CO} versus distance from the stagnation plane for $\phi = 0.50$, $\alpha = 0.10$, $\kappa_{init}/\kappa_{ext} = 0.90$ and f = 200Hz.

In both plots, Y_{CO} decreases towards the stagnation point, indicating consumption of CO late in the flame. This is referred to as CO burnout. The energy released during the consumption of CO adds to the overall energy release of the flame. The Y_{CO} profiles show that CO is consumed late in the flame with the exception of the profiles right at extinction. At extinction, the CO consuming reactions cannot be maintained and the Y_{CO} increases. These profiles indicate that the CO burnout reactions are not as susceptible to oscillations as other flame properties investigated here.

5.5.2 Diffusion zones

The temperature and mass fraction profiles of H_2 and CH_4 for a $\phi = 0.5$, $\alpha = 0.10$ flame with an initial strain rate of $\kappa_{init}/\kappa_{ext} = 0.9$ oscillated at 200Hz are plotted in Figure 5.19 as a function of the distance from the stagnation plane. The three flame properties are plotted at the minimum and maximum strain of the amplitude A_{ext-1} as well as at the point of flame extinction. The H_2 profiles clearly show the diffusion of H_2 into the flame zone ahead of CH_4. Y_{H2} begins to decrease before there is an increase in temperature, so no reactions are consuming H_2. Therefore, H_2 must be diffusing ahead of the bulk flow. The different mass diffusion lengths shown in Figure 5.19 illustrate the need for the multicomponent integral analysis conducted earlier to capture the effects of multiple fuel species. Furthermore, the forced oscillations cause the edges of the thermal and mass diffusion zones to move. This means that the diffusion zone lengths defined in the integral analysis section are not constant for an oscillating flame and the application of the integral analysis to oscillating flames would require modifying the definition of the diffusion zones. Finally, Figure 5.19 indicates that H_2 is not fully consumed in the reaction zone. This is because the initial flame is very near extinction, $\kappa_{init}/\kappa_{ext} = 0.9$, the H_2 produced within the reaction zone 'breaks through' unburned.

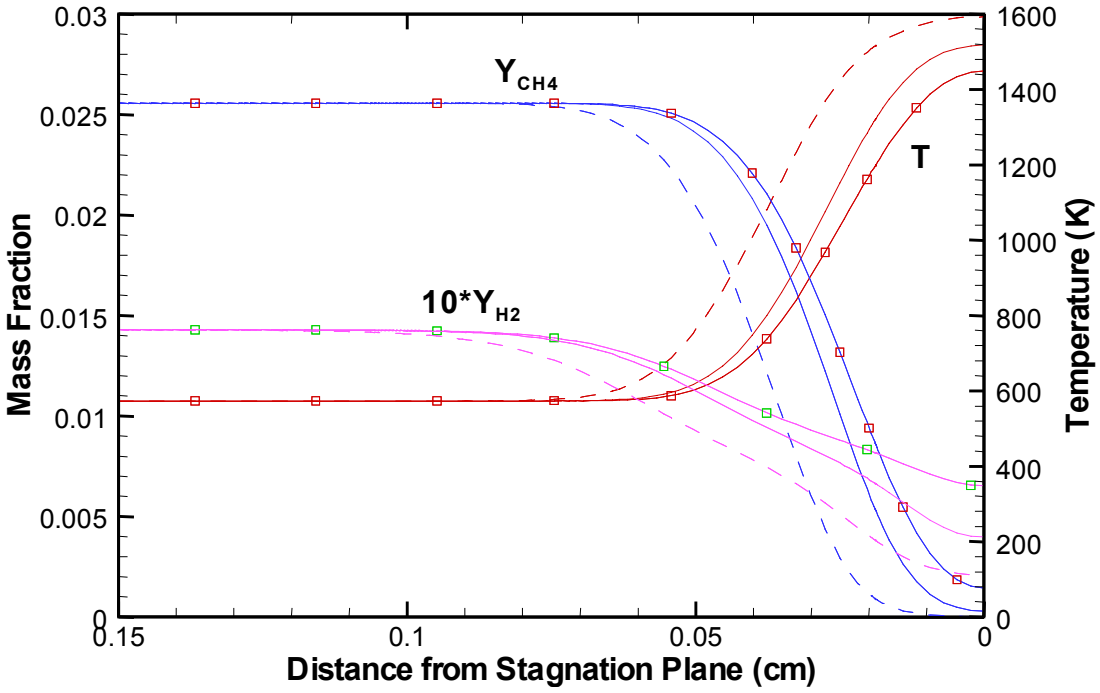

Figure 5.19: Temperature, Y_{CO} and Y_{H2} at minimum and maximum strain rates versus distance from stagnation plane for $\phi = 0.5$, $\alpha = 0.10$, $\kappa_{init}/\kappa_{ext} = 0.9$ and $f = 200$Hz.

5.6 Extinction Amplitudes

The extinction amplitudes for each fuel mixture studies were determined through modeling. As explained earlier, the exact extinction amplitude is difficult to determine because the amplitude was increased in steps during the numerical simulation. Therefore, the extinction amplitude may be between two amplitude steps. Figure 5.20 is a plot of the extinction amplitudes for the $\phi = 0.75$ cases plotted versus the amplitude frequency. Generally, the extinction amplitudes increase with increasing frequency and with decreasing α. Furthermore, as $\kappa_{init}/\kappa_{ext}$ approaches 1.0 the extinction amplitude decreases. In Figure 5.20, the differences between the flames of a given initial strain rate

are not very apparent until the oscillations reach 400Hz. At 400Hz the oscillation effects are becoming dominant, as the oscillation timescale 0.025s for 400Hz is now in the range of the flame's combustion timescale.

Figure 5.21 shows similar results for $\phi = 0.5$, but the curves are not as smooth as for $\phi = 0.75$. The initial $\phi = 0.5$ flames are near their lean steady state extinction limit and are substantially weaker flames than the $\phi = 0.75$ flames. Therefore, the extinction amplitudes were much more difficult to accurately determine. However, even with the difficulties, the trends found in the $\phi = 0.75$ flames are also true for $\phi = 0.5$.

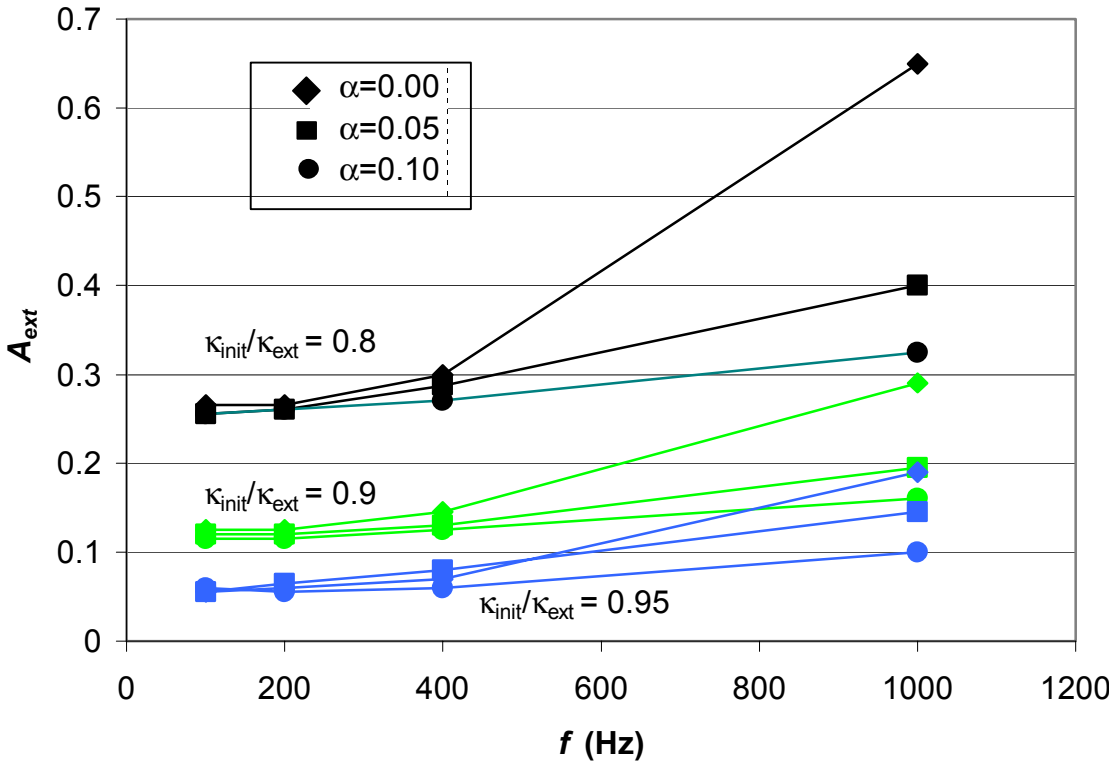

Figure 5.20: Numerical extinction amplitudes versus frequency for all $\phi = 0.75$ flames.

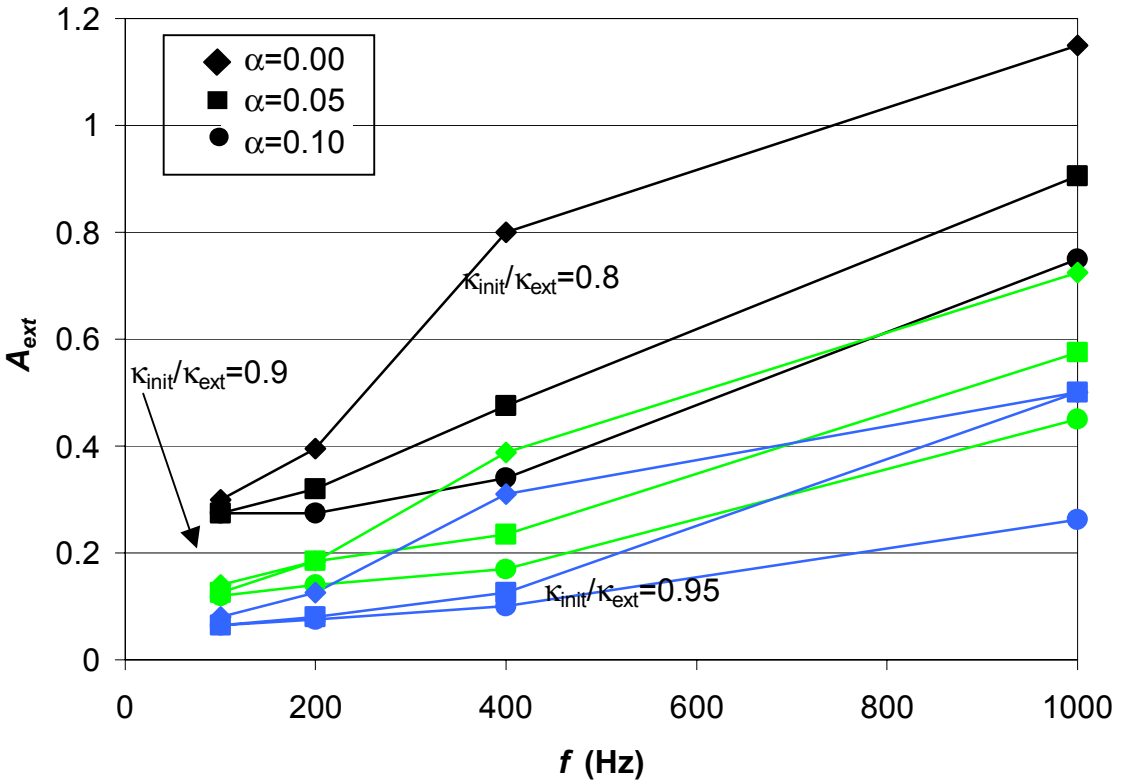

Figure 5.21: Numerical extinction amplitudes for all $\phi = 0.5$ flames.

When the extinction amplitudes for both ϕ's are plotted versus a non-dimensional frequency, f/κ_{init}, three distinct groups are found. These results are plotted in Figure 5.22. The three groups correspond to the three initial values of $\kappa_{init}/\kappa_{ext}$. The fact that the effects of H_2 on the extinction amplitude can be captured through the change in κ_{init} implies that the dominant aspects of the extinction deal more with the flow field than the chemistry.

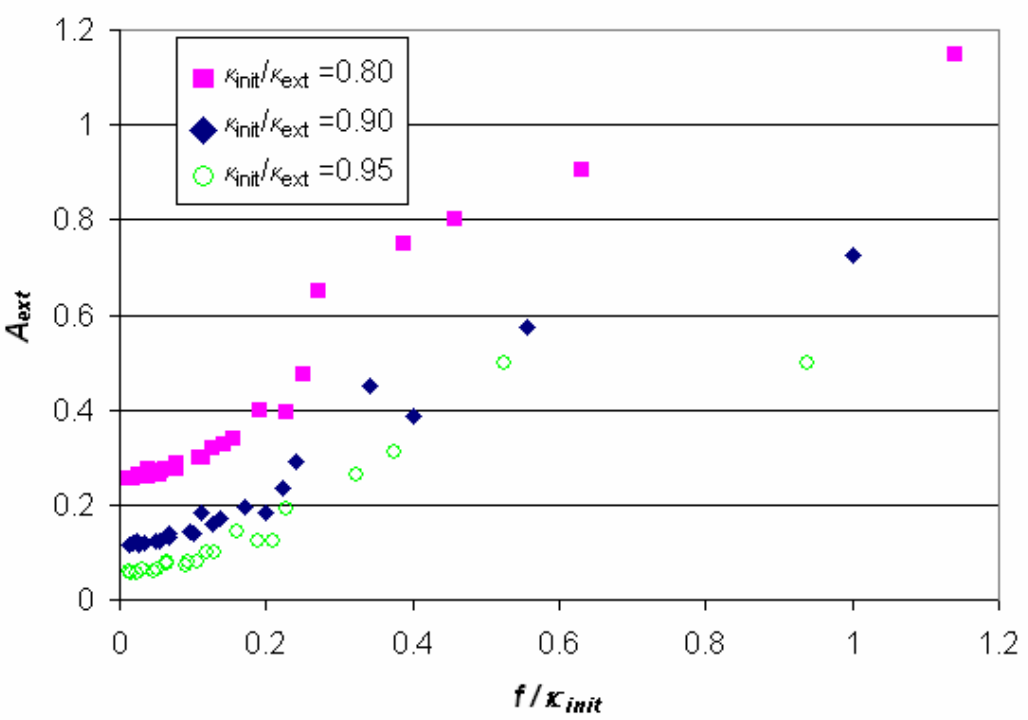

Figure 5.22: Numerical extinction amplitudes of all flames versus non-dimensional frequency.

5.7 Combustion Products

Mass fractions of three notable combustion products at the stagnation plane were integrated over several cycles of oscillation to determine their relative increase or decrease in production with respect to the steady state flame. The species of interest are NO and CO, to investigate pollutant production, and H_2 to investigate relative combustion completeness or efficiency. The mass fractions were integrated at the stagnation plane over several cycles at $A_{ext\text{-}1}$ and divided by the integrated values of the steady state flame.

The relative production of NO is plotted in Figure 5.23. It can be seen that increasing the frequency decreases the production of NO. As frequency increases, $A_{ext\text{-}1}$

increases, leading to larger oscillations in temperature and a weaker flame. NO producing reactions require high temperatures, so the weaker flame produces less NO. The NO production for $\phi = 0.5$, $\alpha = 0.0$ flames with initial strains of $\kappa_{init}/\kappa_{ext} = 0.9$ and 0.95 are very similar. This shows that the initial strain rate does not have much of an effect on NO production. However, the fact that the NO production is slightly lower for the $\kappa_{init}/\kappa_{ext} = 0.95$ case shows that the flame weakens relative to the initial state during oscillations. H_2 addition increases NO production, or brings the NO production closer to the steady state rate. This is similar to other results that show H_2 addition reduces variations from steady state results. The reduced variation in NO production is also true for the $\phi = 0.75$ cases. Finally, the variation from steady state production is larger for the $\phi = 0.5$ flames than the $\phi = 0.75$ flames. This indicates that the initial $\phi = 0.75$ flames are stronger less susceptible to oscillation induced variations.

The relative CO production is plotted in Figure 5.24. These results are similar to the NO results with the magnitude inverted. CO production increases with increased frequency and amplitude. Again, the initial strain rate has a small effect. H_2 addition has a large effect on CO production by decreasing the variation from the steady state values. The non-linearity seen at 200Hz is due to the step increases used while computing the extinction amplitudes. The responses for both CO and NO are not linear with respect to frequency. The magnitudes of the slopes for both species decreases with increasing frequency. This is an indication that with increasing frequency flame cannot maintain quasi-steady state behavior and the flame response to oscillations attenuates. Furthermore, the increase in CO breakthrough shows that the flame is consuming less CO than the steady state.

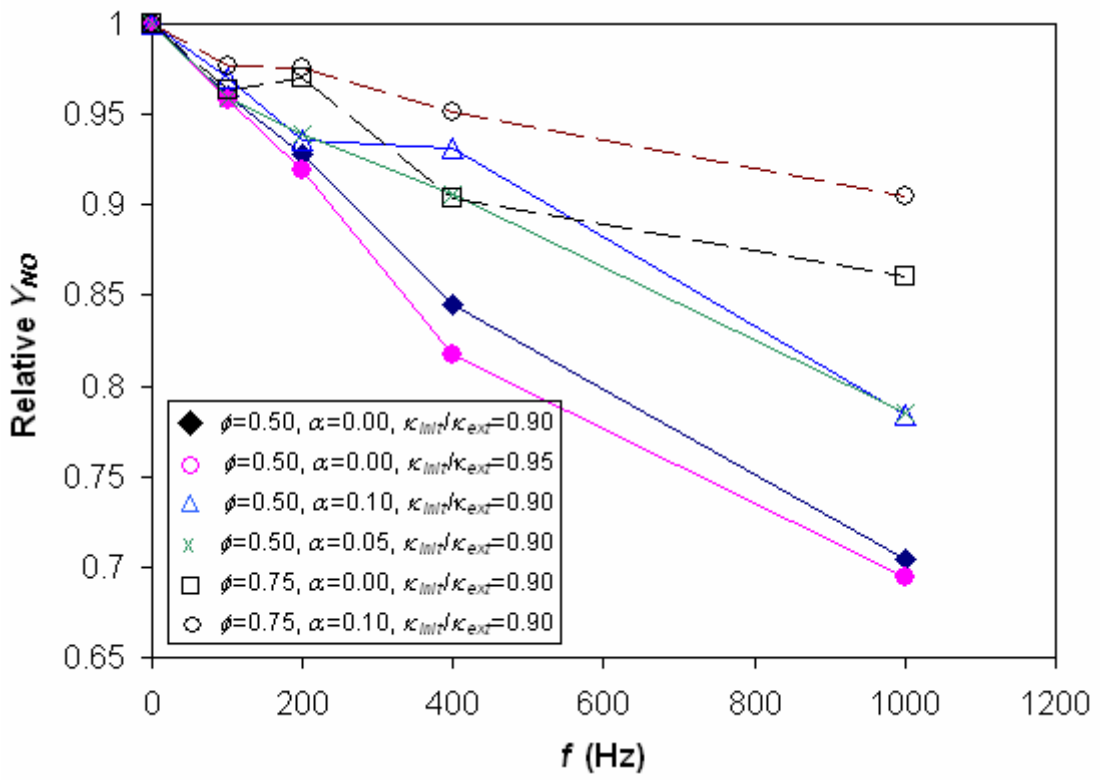

Figure 5.23: Production of NO relative to the production from the initial steady state flame versus frequency for several initial flames.

Finally, the concentration of H_2 in the reaction products is an indication of the combustion efficiency. Figure 5.25 is a plot of the integrated H_2 concentrations relative to steady state. It can be seen that all the oscillating cases produce some H_2, even the cases with $\alpha = 0.0$. The H_2 in those flames is produced through the chain branching reactions breaking down CH_4. The H_2 at the centerline increases with increasing oscillation amplitude as the flame oscillates about a mean flame condition closer to the extinction point. When comparing flames at the same ϕ but different α in Figure 5.25, the relative amount of H_2 at the stagnation plane is approximately the same. H_2 addition does not improve the combustion efficiency of a flame subject to oscillations. This

indicator of relative global combustion efficiency shows that the global flame response is not strongly dependent upon α.

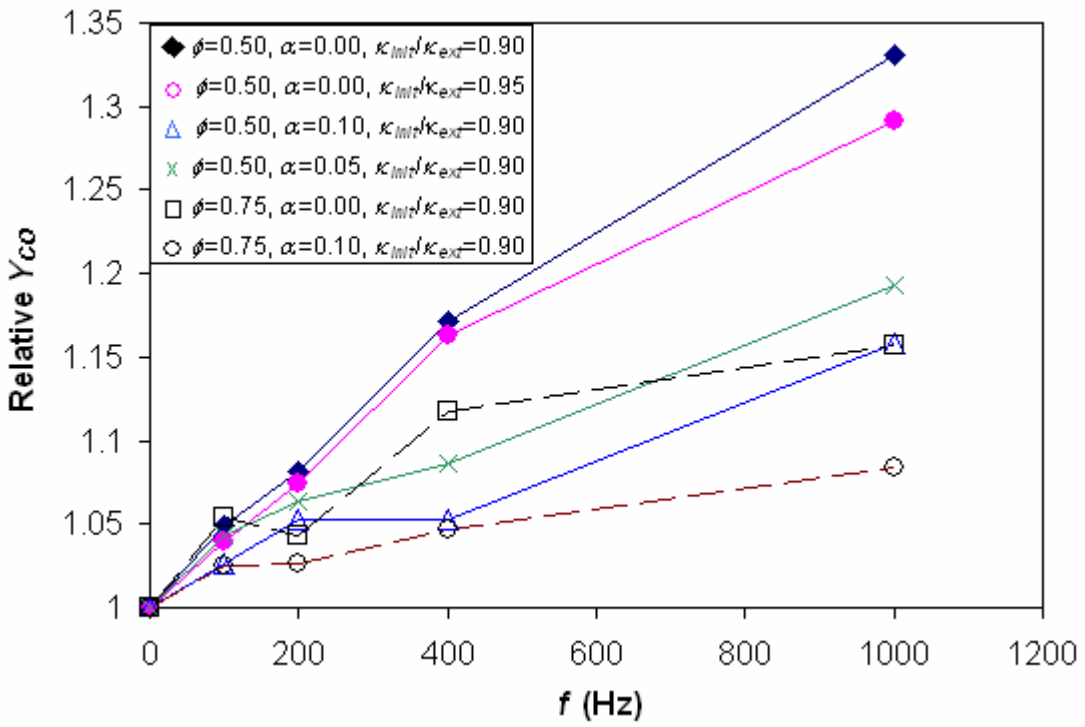

Figure 5.24: Integrated Y_{CO} at the stagnation plane relative the initial steady state flame versus frequency for several initial flames.

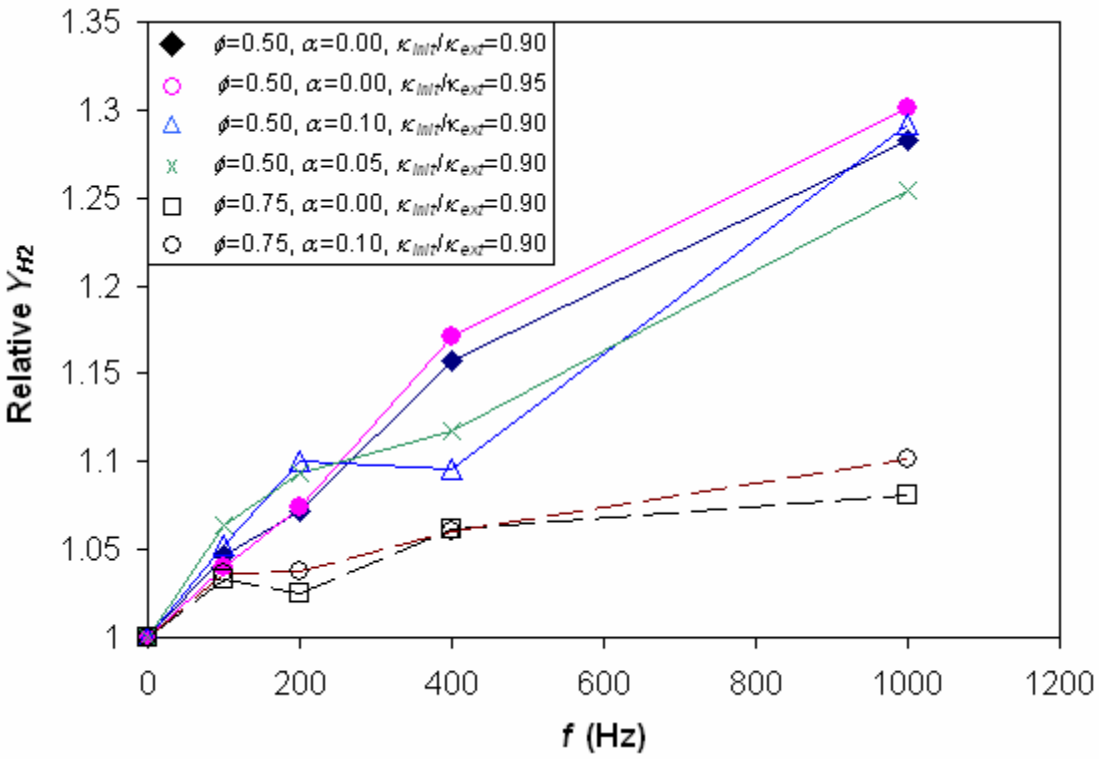

Figure 5.25: H_2 in combustion products at stagnation plane relative to the initial steady state flame versus frequency for several initial flames.

5.8 Conclusion

In this chapter, the numerical code TREC was used to investigate the behavior of lean CH_4-air flames exposed to transient boundary conditions. The results uncovered interesting behaviors. A_{ext} decreases with increasing ϕ and α, and increases with increasing f. Furthermore, the flame responses attenuate with increasing f. This behavior was seen in the results of T_{flame}, flame position and several species mass fractions at the stagnation plane.

The increase in flame property variations with increasingly rich flames indicate that flamelet models may not capture the correct physics when steady state flame responses are assumed. For transient conditions with neat extinction flames, transient

flame responses may help predict the turbulent flame behavior with respect to extinction and pollutant production.

Chapter 6 Experimental Configuration

6.1 Introduction

The counterflow experiments were conducted to gain experimental data to help validate the flame behaviors found using the transient computations. The experiments were performed using an opposed nozzle counterflow test rig with speakers positioned upstream to apply pressure oscillations to the nozzle exit flows. By imposing pressure oscillations, and the corresponding velocity oscillations, extinction amplitudes were measured and compared with predictions from the numerical model. Laser Doppler Anemometry was employed to measure fluctuating velocity profiles in the counterflow flames exposed to the speaker driven oscillations. These velocity profiles were compared to predicted profiles to examine effects of oscillations and how hydrogen addition modifies the flow field.

6.2 Experimental Rig Components

The counterflow experimental rig was designed and constructed over several iterations. The original use of the rig was to generate steady state premixed counterflow flames. Through extensive modifications, the rig was improved to provide better flow properties, allow for LDV measurements and impose transient conditions. The data acquisition and control system also required work to ensure that all the components worked together well. The efforts resulted in a robust system that produces a uniform, stable counterflow flame.

The basic construction of the experimental rig is the same as described in earlier work [43]. A partial schematic of the rig can be seen in Figure 6.1. Air is provided by a

compressed air system. The airflow is split and sent through two electronic mass flow controllers (MFC). Two separate calibrated MFC's are used to ensure that the air flows are balanced between the top and bottom opposed jet nozzles. The top and bottom air flows are each split through a cross fitting to provide three streams for each nozzle. The streams are balanced via needle valves to control the backpressure. The principal fraction of the air streams go to the main air preheaters. The two bypass air flows for each nozzle are used for cooling air for the flow excitation speakers, and for the carrier air in the fluidized bed seeders. These bypass air flows rejoin the main flow upon entering the opposed jet nozzles as discussed later.

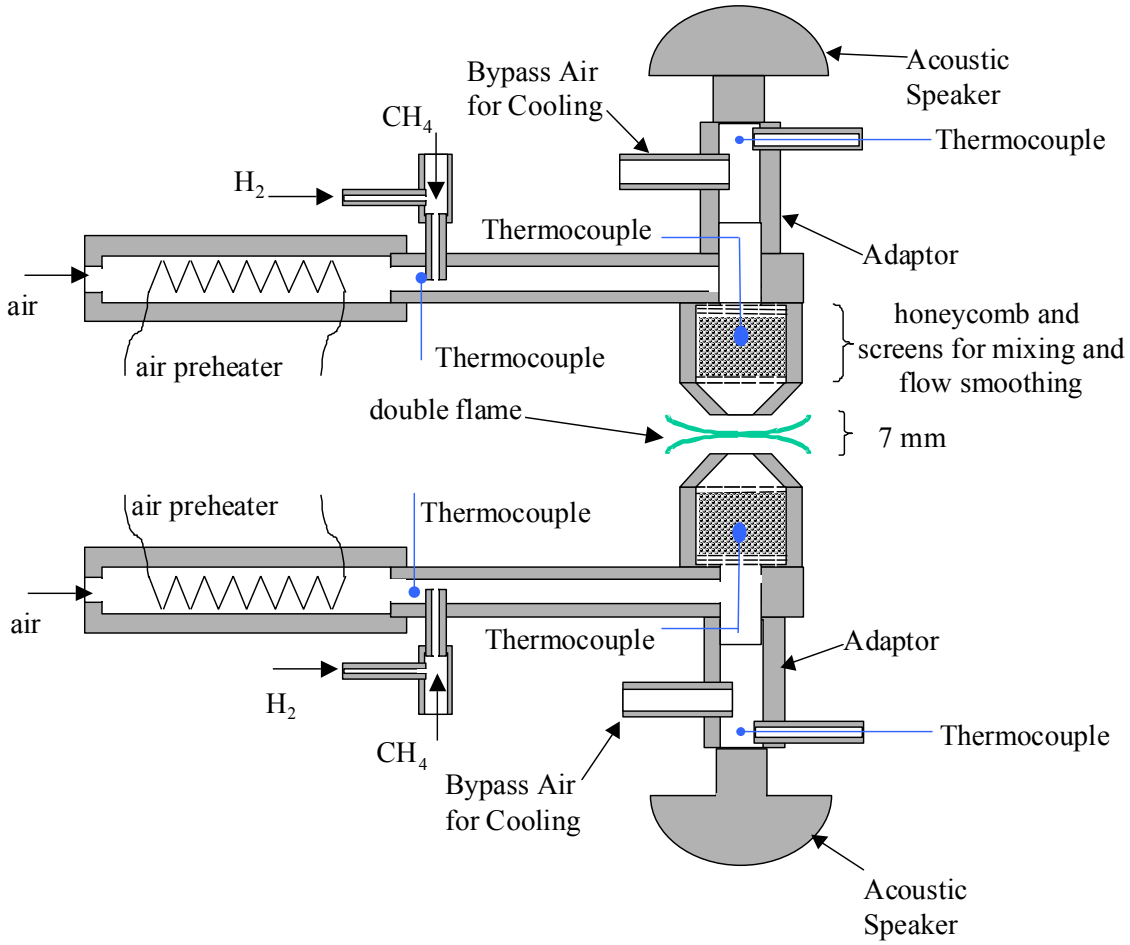

Figure 6.1: Schematic of the nozzle gas feeds for the counterflow flame test rig including the speakers used to impose the nozzle exit pressure oscillations.

Triple pass flow heaters (from Convectronics with up to 3600W maximum heating) used to provide high temperature primary airflows. The heaters were controlled using AC variacs to set nozzle exit temperatures to desired values (up to 300ºC in this study) while compensating for thermal losses. Experimental conditions were maintained such that the measured heater exit air temperatures remained below 700 ºC. The desired elevated nozzle exit temperatures distinguish this study from previous counterflow premixed flame studies on fuel mixtures [44], and these temperatures allow premixed flames to remain stable at much higher strain rates than with flames using room

temperature nozzle flows. The higher strain rates, with corresponding higher velocities, reduces the significance of buoyancy forces induced by the large temperature gradients by increasing viscosity and allowing for higher flow throughputs, thereby increasing the Reynold's number and reducing the Grashof number associated with the temperature difference.

The fuel gases are provided from high pressure cylinders of H_2 and CH_4. One MFC is used for each fuel. A MFC meters the total mass flow rate of the fuel required for both top and bottom nozzles. Each fuel component flow is then split through identical 2-tube rotameters, which send balanced fuel flow rates to both of the nozzles. The matching of the split fuel flows is estimated to be within ±5% of the total component flow. For the experiments reported in this study, CH_4 and H_2 are the fuel components fed to the splitting rotameters, and the two fuel components are mixed together before they are injected into the preheated airflow just upstream of the nozzles.

The nozzles were designed to provide a nearly uniform velocity profile across the exit plane. The nozzle contour was designed using the computational fluid dynamics (CFD) code FLUENT. An initial nozzle curve was determined using the Schwarz-Christoffel transformation for planar flows [53]. This method produced a nozzle contour that would provide a uniform exit velocity profile for a 2-D planar nozzle, and this was then used as an initial design in the FLUENT model for the desired axisymmetric nozzle. Several design iterations were conducted using the CFD code to improve the design before the final axisymmetric nozzle contour was determined, as shown in Figure 6.2. The final design has an exit diameter of 8.5mm and was cut from stainless steel using a

CNC lathe. These nozzles provide a much improved velocity profile over the original counterflow nozzles [54].

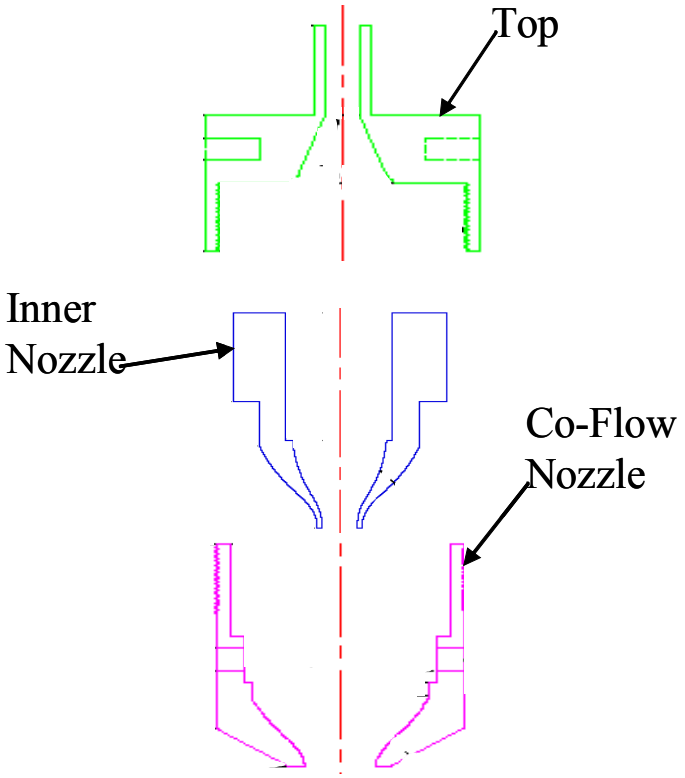

Figure 6.2: Blown-up drawing of the three part nozzle design. The curves of the inner and outer nozzles are defined by numerical data.

A previous study characterized the velocity at the nozzle exit using incense particles with the LDA system. The results of this analysis showed that the nozzles provide an exit flow with an axial velocity within 5% of the core velocity within a radius of 4mm from the centerline. Further, the radial velocity is zero at the centerline, as assumed in the numerical models [43].

The nozzles were designed in three pieces for ease of assembly. Mounting plates were fabricated to hold the nozzles vertically aligned at a separation distance of about

7mm. The nozzles were mounted through the center of the plates and the plates were maintained in vertical alignment by mounting them on 3 steel rods. There is a very tight fit between the nozzle and the mounting plate to help ensure alignment of the nozzles. The space between the inner and outer nozzles forms an annular region designed to provide a co-flow surrounding the primary central flow to reduce buoyancy effects at the outer radial edges of the counterflow flame. This co-flow air was found to be unnecessary in the current study because the elevated nozzle exit temperatures resulted in relatively high velocity outlets and inertial forces overwhelmed buoyancy forces near the central 2cm core diameter of the flame.

Within the central flow nozzles, three layers of steel honeycomb serve as both a flow straightener to reduce turbulence upstream of the nozzle convergence, and as a thermal mass to damp out temporal variations in temperature. A shielded K-type thermocouple, with 0.40cm O.D. shield, is positioned within the honeycomb layers to measure the flow temperature exiting the nozzle.

Acoustic speakers mounted upstream and in-line with the nozzles impose the transient oscillations. The speakers are cone speakers, originally designed for use with emergency vehicle sirens. Each speaker connects to a nozzle through a threaded cone machined from aluminum. The cones are needed to reduce the flow diameter at the speaker exit, 1.0in, to connect to the diameter at the bottom of the nozzles, 0.25in. The bypass speaker cooling air mentioned above enters this cone through a tap on its side, and the speaker temperature is monitored using a thermocouple inserted in the cone adjacent to the speaker diaphragm. The speakers were not designed for a high temperature

environment and therefore, it was decided to limit the speaker operating temperature to 50°C.

One speaker is used for each nozzle, and the speaker excitation imposes both pressure and velocity oscillations on the nozzle flow. A sine wave, generated by a signal generator and amplified to a range of 1 to 16VAC, controls the speakers. The actual AC amplitude sent to the speakers is measured by a multimeter. In offline tests, the strength of the oscillations imposed by a speaker through the nozzles was characterized by a piezoelectric pressure transducer. The details of this calibration are discussed in the following chapter.

Figure 6.3 is a picture of the full counterflow test rig. The nozzles can be seen connected to the mounting plates and the speakers are located above and below the top and bottom nozzles, respectively. When operating, the counterflow flame is located near the stagnation point between the two nozzles. Figure 6.4 is a picture of a flame generated by the test rig. The counterflow nozzles can be seen with the blue planar flame located between them. The strength of the flame shows that it is a flame far from extinction.

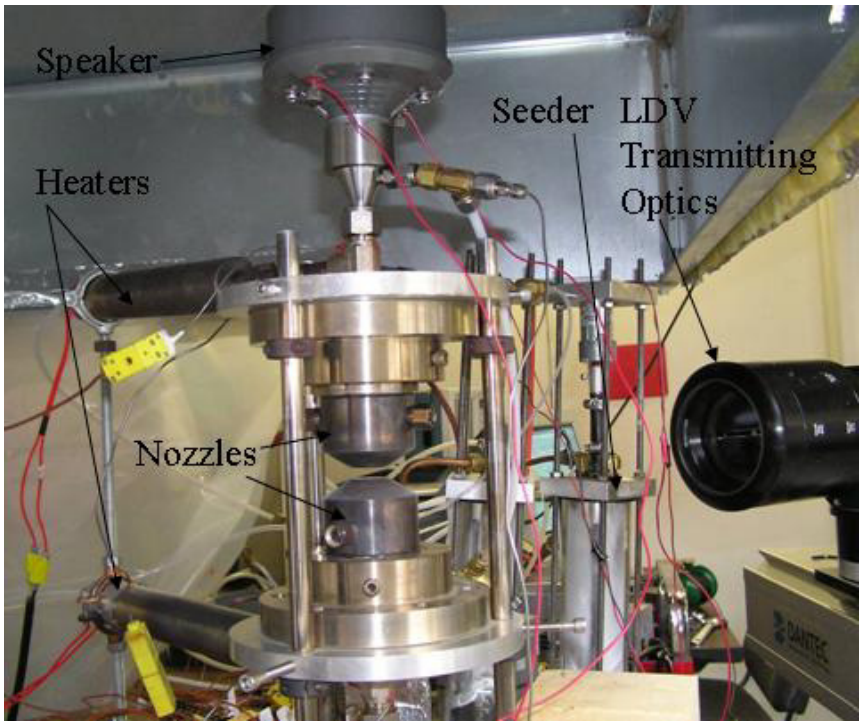

Figure 6.3: Picture of the counterflow flame test rig with some major components labeled. The rig is situated under a ventilation hood.

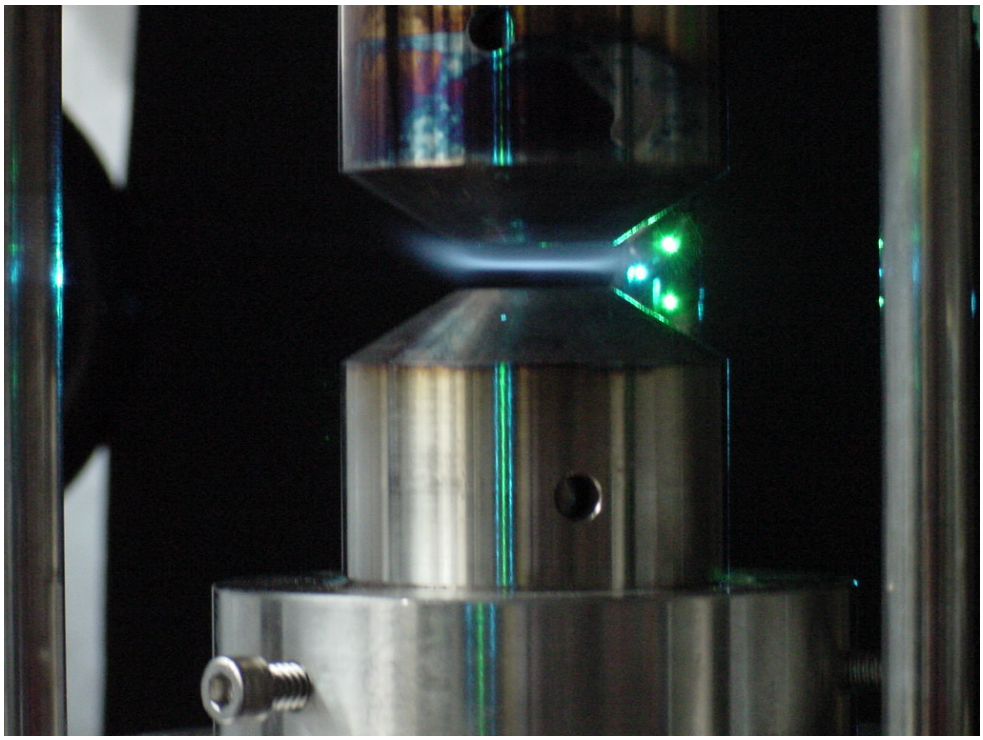

Figure 6.4: Picture of the counterflow flame rig in operation with a flame.

6.3 Data Recording

A National Instruments LabView Virtual Instrumentation (VI) data acquisition system running on a computer controls the test rig. The VI controls and records the MFC measurements and records the temperatures from the thermocouples. Temperatures are recorded at several locations on the rig. There is one thermocouple within each nozzle to measure the nozzle exit temperature. One thermocouple is located at the exit of each of the heaters to monitor the heater temperature, and each speaker has a thermocouple positioned just above its diaphragm to monitor the speaker temperatures. The nozzle temperature is used to compute the nozzle exit velocity. The speaker and heater temperatures are monitored to make sure they do not overheat during a test.

The LabView VI requires input settings from the experimenter for the desired ϕ, α and nozzle exit velocity. The controller computes the required mass flow rates of each gas to match the desired fuel composition and velocity at the current nozzle exit temperature. The MFC's are then continuously adjusted to match the required mass flow rate. The user inputs, measured mass flow rates, commanded mass flow rates and monitored temperatures are all displayed on the computer monitor and may be saved to a data file.

6.4 Laser System

A Laser Doppler Anemometry system (LDA) manufactured by DANTEC was used to measure the flow velocity in the counterflow region with minimal affect to the flow field. The LDA system is composed of a dual Spectra Physics argon-ion laser (488nm and 514nm wavelength), a Bragg cell, a fiber optic coupling to transmitting and

receiving optics, and a computer-controlled traverse for the optics with 2-D positioning. The entire system, except for the laser power and focusing, was controlled with the DANTEC provided software. The argon-ion laser-beam passed through a Bragg cell, which splits the beam and shifts the frequency of one beam by approximately 40MHz. The two beams are then sent through fiber optic cables to the transmitting optics, where they are split again and passed through a lens which focuses the two pairs of beams on a small probe volume positioned in the region of interest along the centerline of the opposed jet flow field. One of the beam pairs is split in the horizontal direction and is used to measure horizontal velocities, whereas the second beam pair is split in the vertical direction to measure vertical flows. In this study, only the vertical velocity component are of interest and only the beam pair used for vertical measurements are used.

The LDA system measures the velocity of particles as they pass through the probe volume of approximately 0.1-0.2mm in diameter and 0.3-0.6mm in length [55]. Within the probe volume, the intersecting laser beams create a series of fringe patterns due to alternating constructive and destructive interference. Velocities to be measured in the counterflow regime are in the vertical direction, so the beams are configured to create the fringes normal to the velocity direction. The frequency difference between the two beams, created by the Bragg cell, causes the fringe patterns to 'roll' vertically through the probe volume. If the intersecting beams were of the same frequency, the static fringe pattern would allow the measurement of the magnitude of the particle velocity, but not the direction. The rolling fringes allow for the direction to be determined as well, by timing the speed of the fringe rolling.

The width of an individual fringe can be computed from the geometric angles of the intersecting beams, the original laser wavelength and the frequency shift between the two beams. As a particle passes through the probe volume, and through the fringe patterns, the incident laser light is scattered with alternating lower and higher intensity. The receiving optics detect this fluctuating intensity and the computer determines the frequency of the variation, the beat frequency. The beat frequency relates how fast the particles pass through an individual fringe, and using this together with the width of the fringes, the particle speed may be determined. The particle speed can then be found by measuring the frequency of the light scattered by the particle as it passes through the fringes using the following equation

$$f_D = f_o + \frac{2\sin\left(\theta/2\right)}{\lambda} u_x \ , \tag{6.1}$$

where f_D is the measured frequency of the scattered light, f_o is the frequency shift between the two beams, λ is the laser wavelength, θ is the angle between the two incident beams and u_x is the velocity component normal to the interference fringe pattern.

The transmitting and receiving optics are mounted on a traverse capable of moving in two dimensions. The traverse is controlled by the computer and was programmed to move through a vertical grid of measurement locations along the centerline between the nozzles. The LDA system was set to remain at a specified point until either it had measured the velocity of 30,000 particles or ten minutes had elapsed. The traverse then moved to the next location. The velocity at a given point was later computed as the average of all the measured particle velocities at that location.

In this study, the velocity measurements were used to investigate the axial velocity variation over one cycle of the imposed oscillations. Since the excitation

oscillations from the speakers were cyclic sine waves, velocity measurements could be taken over many cycles and averaged to obtain an accurate measurement. This is accomplished by tagging each particle velocity measurement with the time the particle arrived at the probe volume. The signal generator used to generate speaker signal also sends a TTL reset signal to the LDA computer at the beginning of each cycle. The particle arrival time is measured with respect to the most recent TTL reset signal, helping ensure a good match between the tagged particle arrival time and the oscillating signal sent to the speakers. The full cycle of 360 degrees was divided into 180 bins, each spanning 2 degrees. A FORTRAN code was written to sort each particle into the correct bin according to its arrival time with respect to the measured cycle.

6.5 Particle Seeding

It is important to note that the LDA technique described above does not measure the gas velocity. It measures the velocity of particles moving with the flow. Therefore, particle seeders are needed to provide the small particles within the flow for the LDA system to measure. It is a challenge to find particles that perform well in the counterflow combustion environment, where the high strain rates and rapid acceleration in the flame zone require very small particles. Furthermore, these particles must be non-reactive to survive the high temperature reactive environment of the flame.

The Stokes number is a non-dimensional ratio between the timescale of the fluid motion and the timescale of the particle motion. Flow regions with large gradients in velocity have small timescales and smaller particles are needed to follow the flow. A particle with a Stokes number much less than one for the given conditions can generally follow the flow well. The Stokes number is defined by

$$St_v = \frac{\tau_v}{\tau_f} = \frac{\rho_c D^2}{18\mu} \cdot \frac{1}{\tau_f} \tag{6.2}$$

where the ρ_c is the density of the fluid, μ the viscosity of the fluid, D the particle diameter, and τ_f the timescale of the fluid domain. Figure 6.5 shows the Stokes number versus particle diameter for an example case. The fluid timescale was assumed to be the inverse of the counterflow strain rate. For Figure 6.5, the extinction strain rate for a ϕ = 0.75, α = 0.10 flame was used for the fluid timescale. The viscosity of air at 600°C was used along with the density of Al_2O_3.

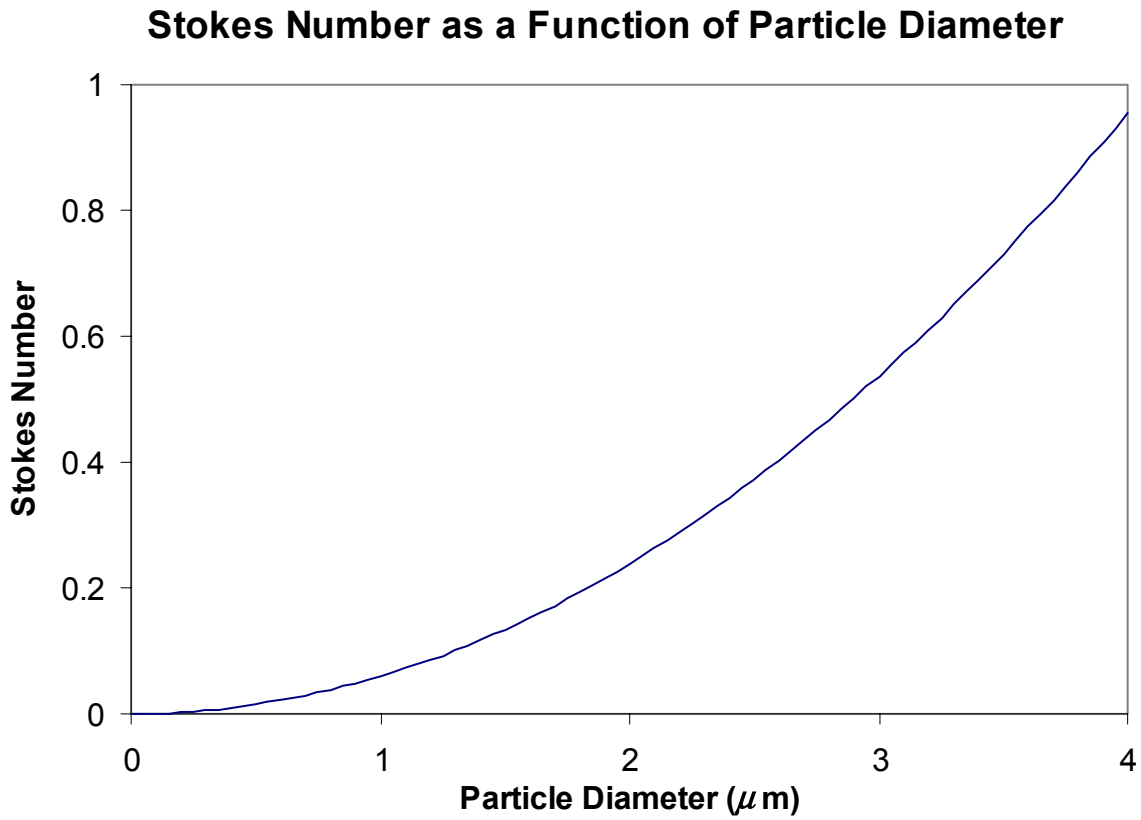

Figure 6.5: Stokes number versus particle diameter for a counterflow regime with a strain rate of 8826 1/s, near the steady state extinction limit for a ϕ = 0.75, α = 0.10 CH_4-air flame.

The results in Figure 6.5 show that for a particle to follow this flow well, requiring a $St_v << 1$, the particle diameter must be < 2μm. One possible source of uniform seeding rates of particles of this size is smoke particles from burning incense. However, incense cannot be used because it would not survive the reacting environment. Oil droplets cannot be used for similar reasons. These types of particles would only provide flow velocity measurements before the flame in the counterflow configuration. The current study is interested in the flow all the way to the stagnation point through the flame. Therefore, a solid, non-reactive particle smaller than about 0.5μm is required such that mild particle agglomeration in the seed flow will not invalidate the Stokes number requirement discussed above.

The large temperature gradient in the flow generates significant thermopheretic forces on particles in this size regime. Thermopheretic forces occur when there are large temperature gradients in the gas from one side of a particle to the other. The higher temperature gas has more energetic molecules and, therefore, more energetic impacts with the particle, causing the particle to move away from the higher temperatures. It has been shown that for a counterflow flame, particles smaller than 1 μm experience significant thermopheris [43, 56]. The experiments in this study are interested in the velocity profiles within the thermal expansion zone where there are large temperature gradients, so thermopheretic effects can become significant in the desired measurements. Given these particle requirements, it was decided to use Al_2O_3 particles. With a density of approximately 3720kg/m^3, the nominal single particle size of 0.05 μm before particle agglomeration gives a Stokes number of 0.000015 for the conditions described above.

However, it is evident from particle visualization that these particles agglomerate into much larger particles on the order of 1μm.

The particle seeders for the seeder bypass flow to each nozzle have two separate components. The first section is a glass-lined fluidized bed 19.6cm tall. The bed is filled with Al_2O_3 particles of 0.05μm diameter. These particles tend to agglomerate into much larger size clumps. The bed is also filled with nickel particles of 100μm diameter. Air is fed through the bottom of the seeders and bubbles up through the bed. The bubbling motion helps the larger nickel particles break up the clumps of Al_2O_3 seed particles. The smaller seed particles are entrained in the air flow and carried out the top of the seeder. The larger, heavier nickel and clumps of Al_2O_3 remain within the seeder. A small DC motor is also used to turn a scraper along the bottom of the bed to assist in mixing and fluidization of the bed.

Once the small Al_2O_3 seed particles exit the top of the fluidized bed, they travel to a cyclone separator. The interior of the cyclone separator is a conic shape. The airflow enters along the outside wall, moves in a cyclonic direction and exits at the top center. The cyclonic action forces larger particles towards the outer wall of the cyclone while the smaller particles follow the flow exiting the top.

Two seeders are used in the experiment, one for the top nozzle and one for the bottom. It was important to seed both nozzles to remove any bias in the velocity measurements near the stagnation plane caused by larger particles passing through the stagnation zone. With both nozzles seeded, larger particles would, on average, pass though the stagnation zone from both ends. Therefore, the average velocity would be closer to the actual gas velocity.

6.6 Flow field Characterization

A test was conducted using the LDA system to measure the velocity profile in the counterflow region. This test was conducted with cold air and no flame with the objective of testing the operation of the laser, the application of the measurement technique as well as to the operation of the speakers, nozzles and the rest of the counterflow rig. Cold air exited the nozzle at 10m/s. The speakers were set to 400Hz with an amplitude of 5VAC. The velocity was measured at specified grid points along the centerline from nozzle exit to nozzle exit. The lasers could only get within about 1mm from the nozzle exit due to the laser beams being clipped by the outer diameter of the nozzle structures. Each measured particle was tagged according to the arrival time at the measurement location. The FORTRAN code described above was used to sort each particle arrival time during the cycle. Figure 6.6 is a plot of the bin counts for the location closest to the top nozzle.

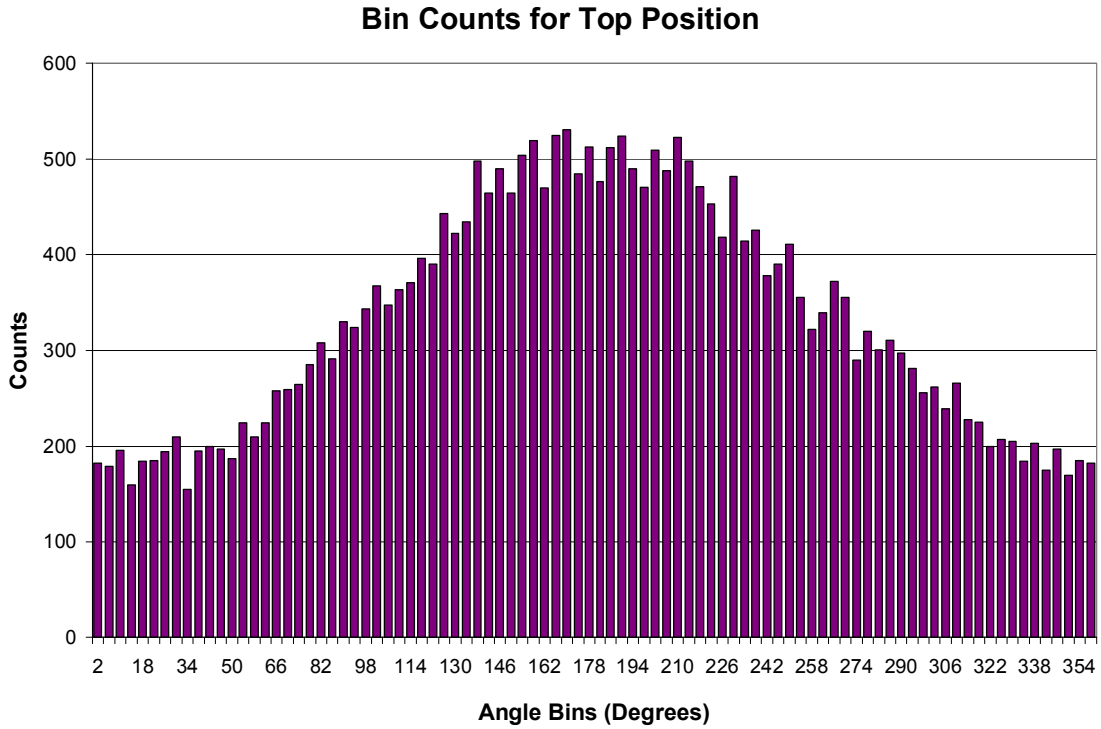

Figure 6.6: Histogram of the 30,000 measured particles sorted into bins according to the particle arrival time.

After sorting and averaging the measurements at each location, a velocity curve can be plotted for each measured location. Figure 6.7 shows the velocity at each location as it varies through a cycle. Measurements taken near the top nozzle are negative, as the flow is moving downward. Velocities near the stagnation point show smaller variations than those closer to the nozzles. The distances are measured relative to the bottom nozzle. The zero distance is the position closest to the bottom nozzle that the laser can reach. The beginning of the cycle was arbitrarily set as the point of minimum velocity measured at the bottom nozzle. A slight phase difference can be seen between the velocity variations near the nozzles versus those closer to the stagnation point.

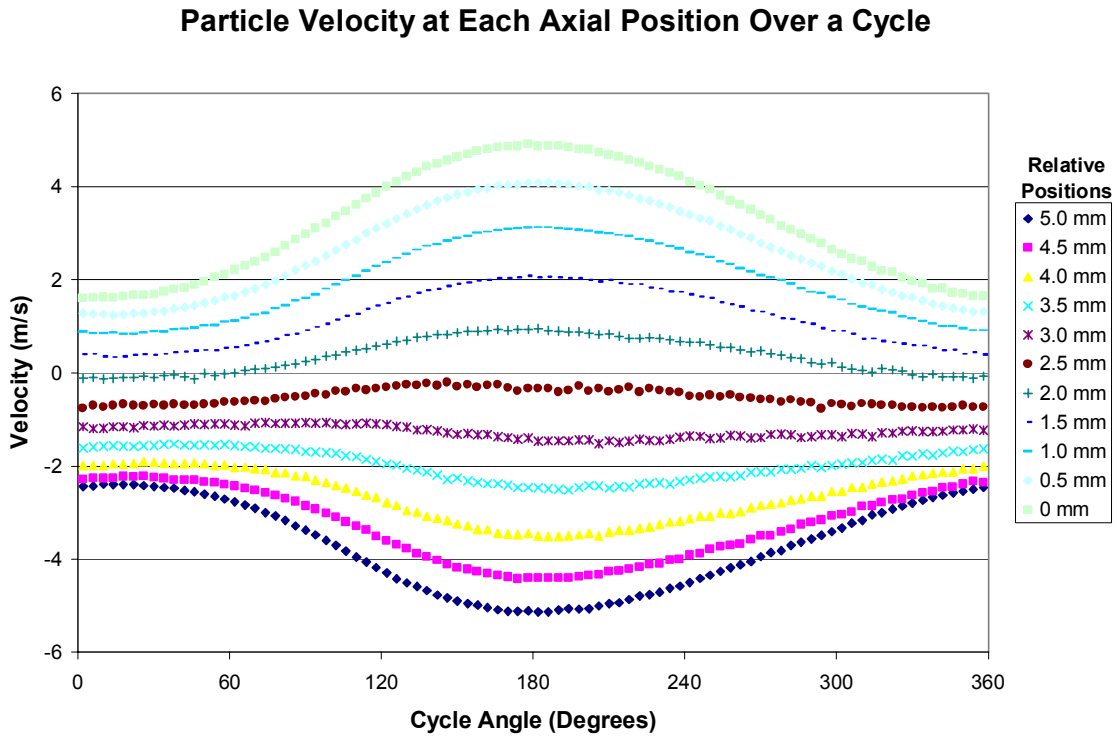

Figure 6.7: Velocities variations over one complete cycle measured at each location.

Figure 6.8 is a lot of the velocity profiles for different moments in the cycle. The maximum (178°) and the minimum (0°) velocity profiles are shown as well as a few intermediate profiles. The intermediate profiles show the progression of the velocity oscillations through one cycle. The fact that the maximum and minimum profiles are almost 180° apart shows that the speakers are imposing symmetric oscillations and gives confidence in the velocity measurement technique. The mean velocity profile is very similar to the 270° profile, as it should be for a sine wave. In addition, the profiles show that the stagnation plane is closer to the top nozzle so the bottom nozzle is flowing at a higher velocity. The cold flow test illustrated that the laser system and seeders were working well enough to make reasonably accurate velocity measurements.

The RMS error of the velocity measurements is shown in Figure 6.9. The plot shows that the error is greater for the measurements near the stagnation zone. This is due significant particle biasing of the measurements toward the velocity of the largest particles in this region. Furthermore, the flame oscillations cause large temperature and density, and thus velocity, fluctuations which also lead to the large RMS values near the stagnation plane. The particle biasing is a source of measurement error while the velocity fluctuations are an expected experimental result.

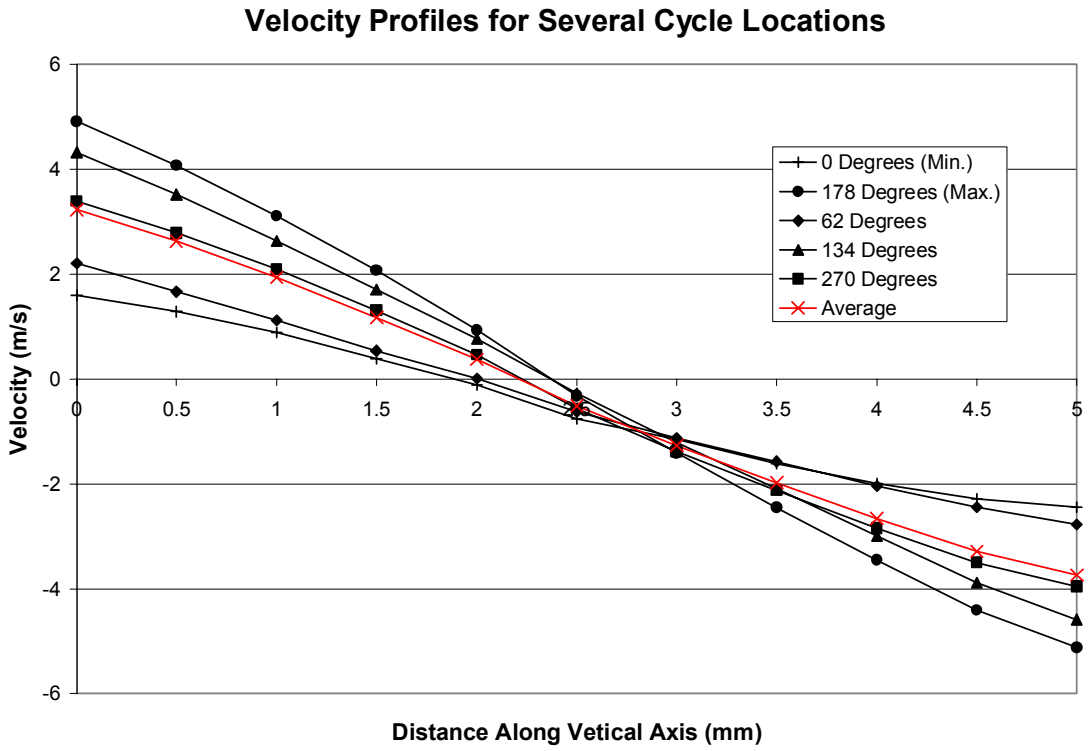

Figure 6.8: Velocity profiles through the counterflow region at different points in the cycle as well as the average profile.

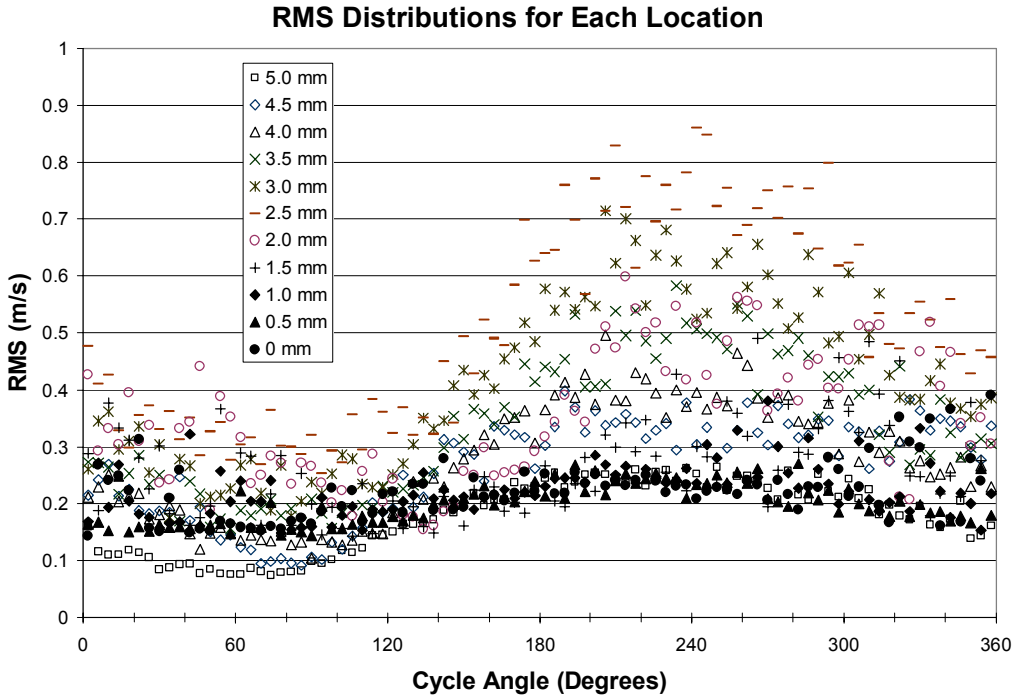

Figure 6.9: The RMS error of the bin sorted velocities for each measurement location.

6.7 Experimental Test Procedure

A test procedure was followed to determine the experimental transient extinction limits. The experimental procedure was similar to the procedure used in the numerical model to find extinction limits. The test rig was set up as described above without the laser system. The first step is to set the desired fuel mixture in the LabView VI. The air flow is then set to the desired nozzle exit velocity and the heaters are turned on to preheat the flow to 300°C. Once the flow temperature stabilizes, the fuel is turned on and the flame ignited. With a stable flame, the signal generator is set to the desired frequency and the signal to the speakers is slowly amplified. The strength of the speaker is noted in VAC from the multimeter display. If the oscillations do not extinguish the flame in 30 seconds, the speaker amplitude is incrementally increased. This procedure is then

iterated until the flame extinguishes. After the flame extinguishes, the test is repeated for a total of at least 3 measurements for each fuel composition and frequency. This procedure provided extinction amplitudes that can be compared to the numerical extinction results.

6.8 Conclusions

The experimental tests were conducted using a specially designed counterflow test rig. Speakers are used to generate transients in axial velocity and pressure. The rig included preheaters to elevate the initial temperature of the flow field to improve flame stability. Furthermore, particle seeders were designed to provide uniform seeding for LDA measurements of axial velocity profiles. Premixed flame responses to the transient conditions will be presented in the following chapter.

Chapter 7 Experimental Results

7.1 Introduction

The test rig described in the previous chapter was used to conduct experiments to investigate the physical phenomena of an oscillating, counterflow premixed flame. This work built on previous studies of steady-state counterflow premixed flames that explored the effects of hydrogen addition on the response to stretch of premixed methane and propane flames [1, 43, 44]. There were several steps in the experimental work. First, the speakers were characterized to determine the magnitude of the oscillations imposed upon the flow. Next, extinction amplitudes were determined for several flame conditions using the procedure described earlier. Finally, the LDA system was used to measure phase-locked velocities within the oscillating counterflow flow fields. The results of these tests are described below.

7.2 Speaker Characterization

Flow oscillations were imposed using acoustic speakers. The imposed oscillations had to be characterized to determine the oscillation amplitude as a function of the desired gas flow temperature, flow velocity, AC voltage and frequency of the signal sent to the speakers. The oscillation amplitude was determined by measuring the pressure variation at the counterflow stagnation plane and computing the velocity variation at the nozzle exit. With the measured pressure variations, the velocity variations were determined using the Bernoulli principle relating the time varying pressure and velocity. It was assumed that since both the experimental flow velocities and the imposed oscillation frequencies are small when compared to the speed of sound,

the transient terms would give only a negligible contribution to the total pressure calculation. Evaluating the Bernoulli equation at the maximum and mean values and subtracting the two gives the pressure difference

$$dP = P_{0,\max} - P_{0,mean} = \frac{1}{2}\rho\left(U_{\max}^2 - U_{mean}^2\right). \tag{7.1}$$

The maximum of the varying velocity is then

$$U_{\max} = \left(\frac{2dP}{\rho} + U_{mean}^2\right)^{1/2}, \tag{7.2}$$

and the amplitude of oscillation is defined as

$$A = \frac{U_{\max}}{U_{mean}} - 1. \tag{7.3}$$

For these tests, the top nozzle was removed from the test rig and a piezoelectric pressure transducer was mounted at the stagnation plane. A piezoelectric transducer was used for its fast response to very small pressure variations at frequencies far greater than the 1000Hz frequency of interest. One difficulty with the transducer was that it could not operate at the desired 300°C conditions. No temperature limit was provided for the transducer but the performance degraded sharply above 100°C. Therefore, the tests were run at lower temperatures and these results were used to extrapolate temperature dependence of the amplitude.

A test matrix of 80 test cases was used to provide a variation throughout the four-dimensional space defined by these four varying conditions: speaker amplitude, oscillation frequency, nozzle exit velocity and nozzle exit temperature. The pressure fluctuations for each test case were recorded for post-processing. Each set of data was then filtered using a Matlab program to apply a Chebyshev band pass filter centered on

the imposed frequency. After filtering the data, the maximum and minimum values of the pressure fluctuations could be determined. Using the *dP* values along with the flow conditions in equations (7.2) and (7.3), the amplitude of the imposed velocity oscillations could be computed.

Next, the measured values were used to generate a curve fit to predict the oscillation amplitude as a function of the flow velocity, flow temperature, and speaker signal AC voltage and frequency. The data was fit to the equation

$$A = a\left(T^{b} f^{c} V_{AC}^{d} U^{e}\right), \tag{7.4}$$

where a, b, c, d and e are constants to be determined for the fit, and T, f, V_{AC} and U are the normalized temperature, frequency, signal AC voltage and mean velocity at the nozzle exit based on total mass flow, respectively. The data was first normalized by dividing by the largest values used in the tests for each input variables. The constants were determined using a singular value decomposition (SVD) method programmed in a FORTRAN code. The code made use of a pre-written subroutine for the actual SVD calculation [57]. The final results of the curve fitting process can be seen in Figure 7.1, Figure 7.2 and Figure 7.3.

Figure 7.1 is a plot of the measured and curve fit oscillation amplitudes versus oscillation frequency for all the cases measured at a nozzle exit velocity of 8m/s. The cases for speaker amplitudes of 1, 4 and 8VAC are labeled. Figure 7.2 is a similar plot for the cases at 12m/s exit velocity. These two plots indicate that the curve fit values do not exactly match all the measured values. The high frequency and low speaker amplitude cases tend to have larger errors.

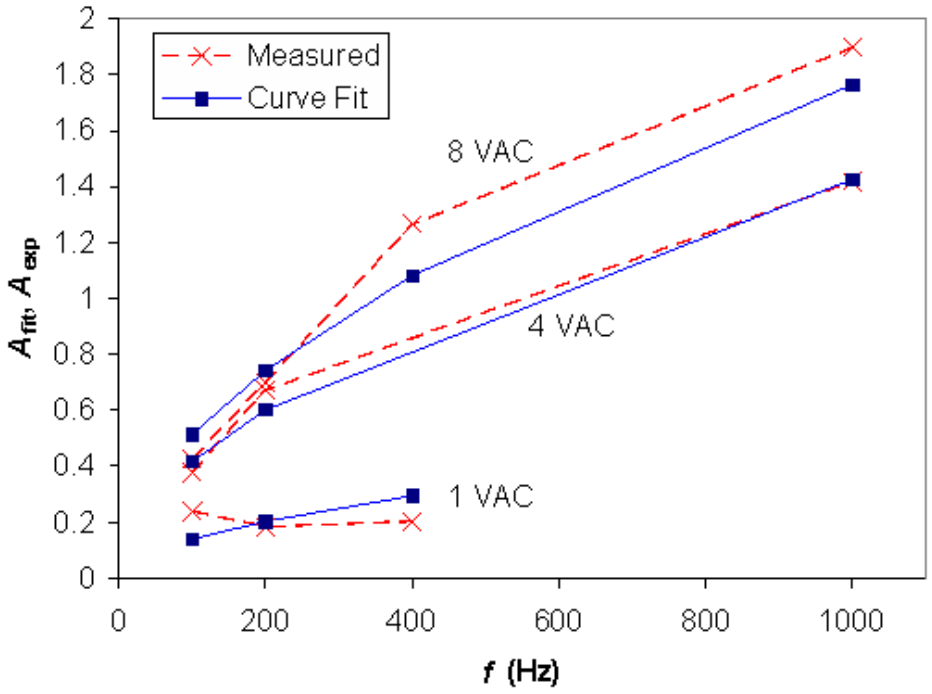

Figure 7.1: Measured and curve fit relative amplitudes versus imposed frequency for nozzle exit velocity U_{in} = 8m/s and speaker amplitudes of 1, 4, and 8VAC.

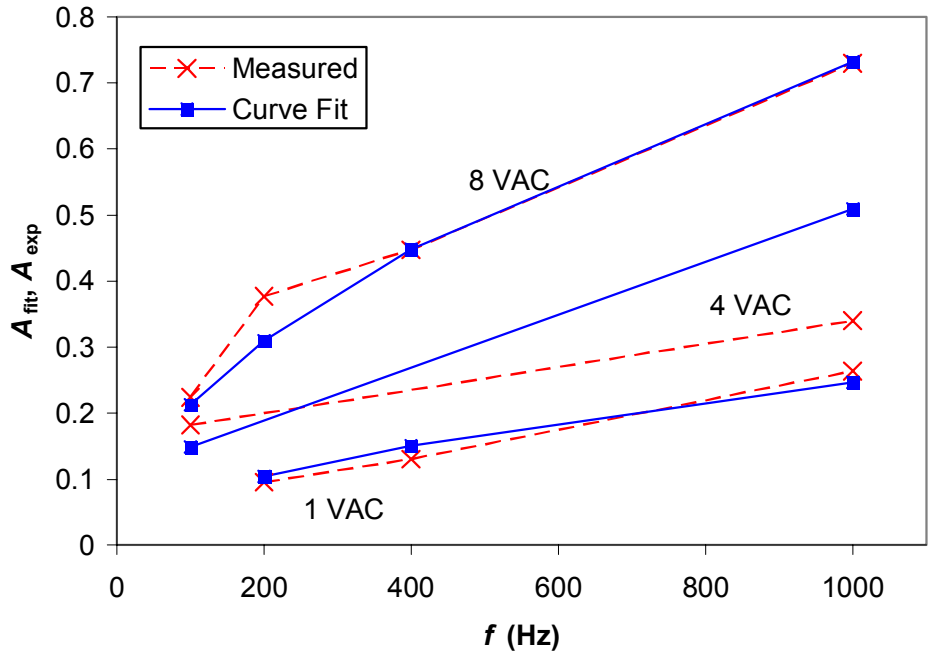

Figure 7.2: Measured and curve fit relative amplitudes versus imposed frequency for nozzle exit velocity U_{in} = 12m/s and speaker amplitudes of 1, 4, and 8VAC.

The overall accuracy of the curve fit can be seen in Figure 7.3 which is a plot of the amplitude of oscillation predicted by the curve fit versus the measured amplitude. The diagonal line represents the one-to-one relationship that would exist for a perfect match between the predicted and measured. It can be seen that the higher amplitude values had more scatter than the lower amplitudes. This curve fit was used later to determine the settings speaker voltage required to produce the desired oscillation amplitude at the set flow velocity, temperature and frequency of oscillation.

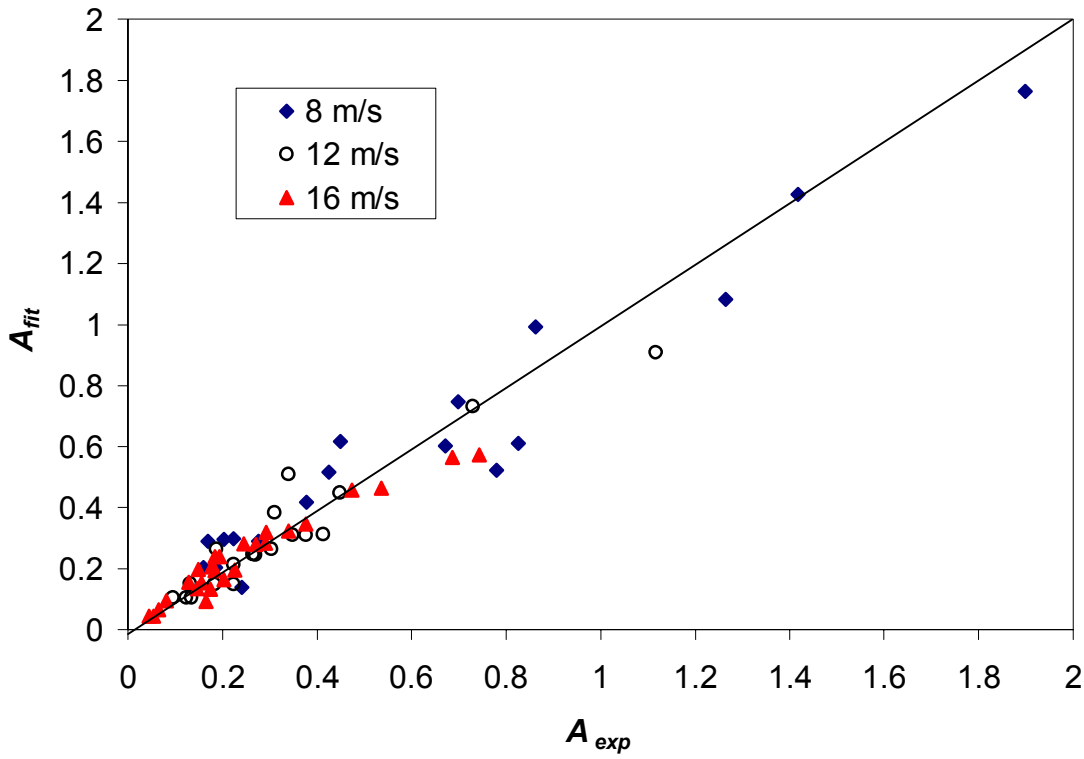

Figure 7.3: Results of the curve fit speaker oscillation plotted versus the measured speaker amplitudes.

7.3 Extinction Amplitudes

7.3.1 Experimental extinction amplitudes

Tests to find the experimental extinction amplitudes were conducted using the procedure described in the previous chapter. There were limitations on what tests could be performed due to the limits of the capability of the test apparatus. The $\phi = 0.5$ cases were not possible due to two problems. First, the low flow rates did not provide enough bypass cooling air to keep the speakers from overheating. Second, at $\phi = 0.5$, pure CH_4 flames are already near flammability limits at atmospheric pressure. Thus, very small variations in conditions can extinguish the flame, and so it was difficult to keep the flame from extinguishing before the speaker amplitudes reached a measurable value. The higher flow rates for the $\phi = 0.75$, $\alpha = 0.10$ case were also difficult because the heaters were unable to preheat the large flow rate of air to the desired temperature. The experiments were conducted with the flow preheated to 300°C. Cases with velocities close to the steady state extinction velocity for the $\phi = 0.75$, $\alpha = 0.10$ flames were not measured in this study.

Table 7.1 summarizes the initial experimental conditions for the cases in this study. The values of actual nozzle exit velocities, U_{mean}, may be determined from the reported U_{ext} in the table and the value of U_{mean}/U_{ext} for each extinction case.

Table 7.1: Mixture composition, nozzle exit temperature, nozzle exit velocity at extinction and extinction strain rate for the experimental cases.

ϕ	α	T_0 (°C)	U_{ext} (m/s)	κ_{ext} (1/s)
0.75	0.00	300.	16.1	4160.
0.75	0.05	300.	19.7	5850.
0.75	0.10	300.	26.0	7800.

To experimentally assess the relationship between strain rate and flame extinction, some means of translating mean nozzle exit velocities into the counterflow field strain rate is needed. The extinction experiments can only measure inlet velocity and not the velocities throughout the entire flow field due to the long time required for LDA measurements and the rapidly unsteady nature of extinction. Thus, for the extinction measurements, velocities at the nozzle exits can be measured easily while strain can only be computed from measure velocity profiles. Strain and inlet velocity are generally linearly related, so plotting experimental results by inlet velocity ratio should be similar to plotting versus strain rate ratio. However, for some cases at high frequencies ($f \geq$ 1000Hz), a lag develops between the variation in nozzle exit velocity and the variation in strain rate. This may lead to the experimental flame actually experiencing lower strain than would be indicated by the nozzle exit velocity.

Figure 7.4 is a plot of the extinction amplitudes for a $\phi = 0.75$, $\alpha = 0.00$ flame. It can be seen that the results follow the correct trend. The extinction amplitude increases with decreasing initial strain rate or U_{mean}/U_{ext}. At low frequencies there is a smaller difference between the measured amplitudes than at the higher frequencies. Furthermore, the amplitudes for the $U_{mean}/U_{ext} = 0.77$ case appear to be twice those for the $U_{mean}/U_{ext} =$

0.84 case. This is similar to the difference between the $\kappa_{init}/\kappa_{ext} = 0.95$ and $\kappa_{init}/\kappa_{ext} = 0.9$ amplitudes for the numerical results.

It can be seen that at 200Hz, the extinction amplitudes have decreased from 100Hz. This occurs for all the test cases. The numerical results show a slight increase in A_{ext} from 100Hz to 200Hz, so the experiments may not have been able to capture this small increase. It is also possible that there may have been a problem with the speaker performance or the amplitude correlation at 200Hz which gave consistently poor accuracy.

The experimental extinction amplitudes for $\phi = 0.75$ and $\alpha = 0.05$ are plotted in Figure 7.5. Again the trends of the experimental results are consistent with the numerical results. The extinction amplitude increases with increasing frequency. The problem at 200Hz mentioned above can also be seen in this figure. It is interesting to note that at $U_{mean}/U_{ext} = 0.49$, the 1000Hz extinction amplitude is over 1.0. This means that at the minimum velocity during the oscillation, the flow is temporarily reversed. At these high amplitudes the flame was flickering and was noticeably blurred. This appears to indicate the flame zone thickened with the imposed 1000Hz oscillations.

Figure 7.6 is a plot of the experimental results for a $\phi = 0.75$, $\alpha = 0.10$ flame. The range of U_{mean}/U_{ext} values tested for this flame are less than the earlier tests due to the problems with preheating the high flow rates previously discussed. The extinction results for this flame also agree with the trends shown in the numerical results. A_{ext} increases with increasing f, and decreasing U_{mean}/U_{ext}.

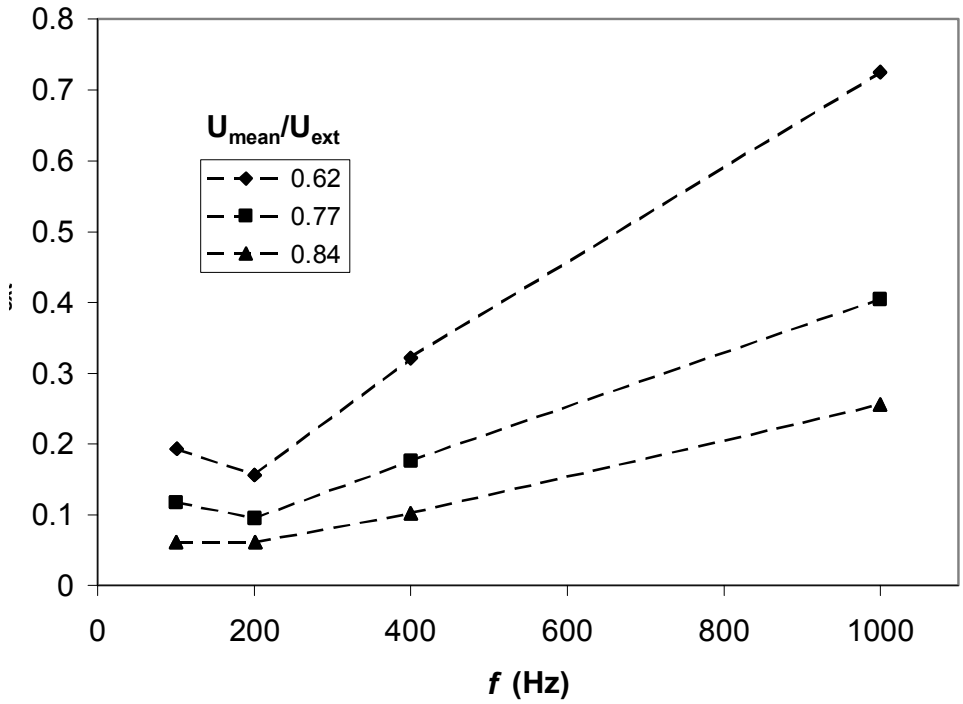

Figure 7.4: Experimental extinction amplitudes for a $\phi = 0.75$ and $\alpha = 0.00$ flame computed at three values of U_{mean}/U_{ext}.

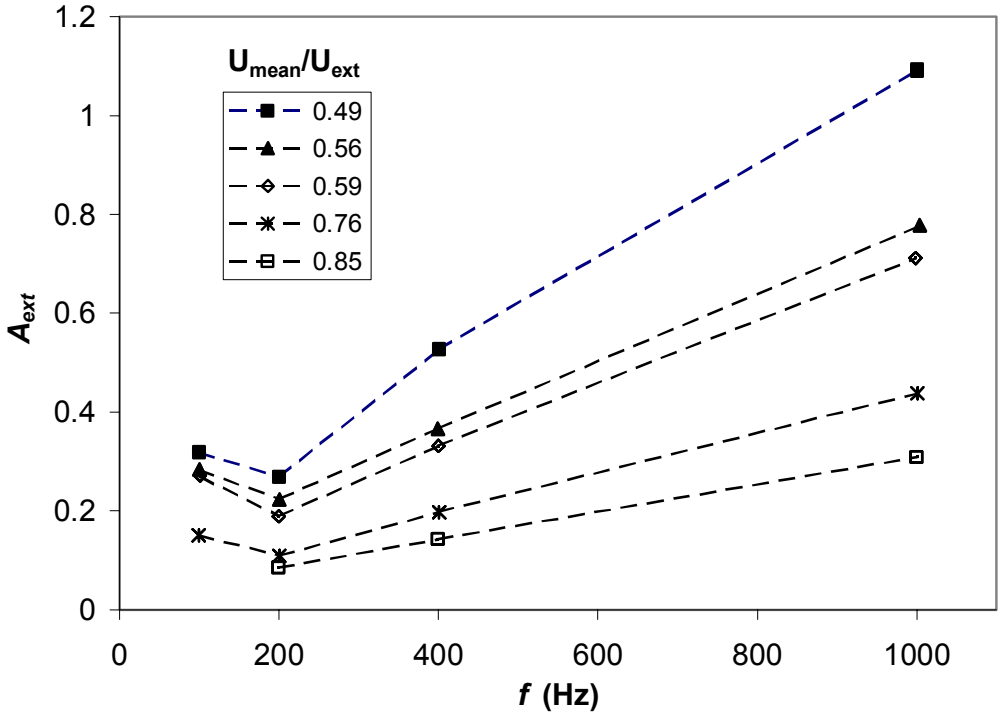

Figure 7.5: Experimental extinction amplitudes for a $\phi = 0.75$ and $\alpha = 0.05$ flame at several values of U_{mean}/U_{ext}.

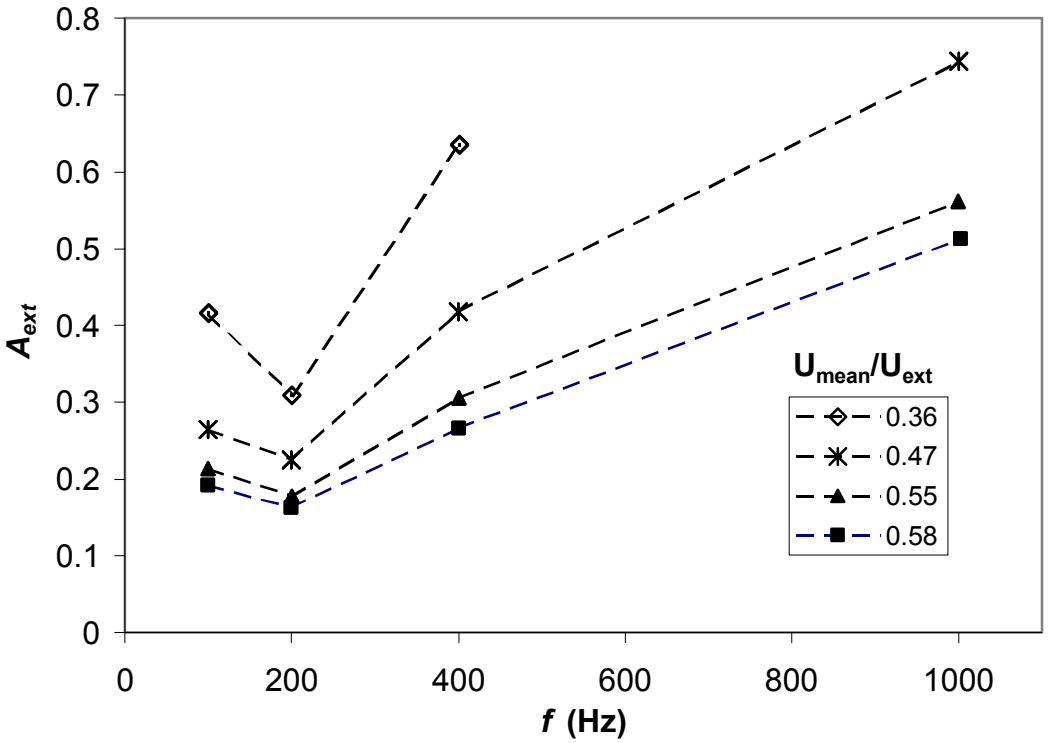

Figure 7.6: Experimental extinction amplitudes for a $\phi = 0.75$ and $\alpha = 0.10$ flame at several values of U_{mean}/U_{ext}.

7.3.2 Effects of H_2 addition

To experimentally examine the effects of H_2 addition, the extinction amplitudes of flames with different α's are plotted in Figure 7.7. The values of U_{mean}/U_{ext} were determined after the experiments were completed, so the different α cases are not all at the same value of U_{mean}/U_{ext}, but they are all similar. The amplitudes for the $\alpha = 0.00$ and $\alpha = 0.05$ cases are almost the same, even at high frequencies. According to both the numerical and experimental results, a flame with $U_{mean}/U_{ext} = 0.58$ should have larger extinction amplitudes than a flame with $U_{mean}/U_{ext} = 0.62$. However, the addition of H_2 to the $U_{mean}/U_{ext} = 0.58$ flame has reduced its dimensionless extinction amplitude. The absolute amplitude U_{mean} has actually increased due to the increase in U_{ext} with increasing

α. The same can be seen for the $\alpha = 0.10$ flame. The $\alpha = 0.10$ flame is at the same value of U_{mean}/U_{ext}, 0.58, as the $\alpha = 0.05$ flame, yet the relative extinction amplitudes are lower for the case with more H_2. This was seen in the numerical results as well and leads to the conclusion that H_2 addition decreases a flame's ability to sustain combustion during strain rate oscillations.

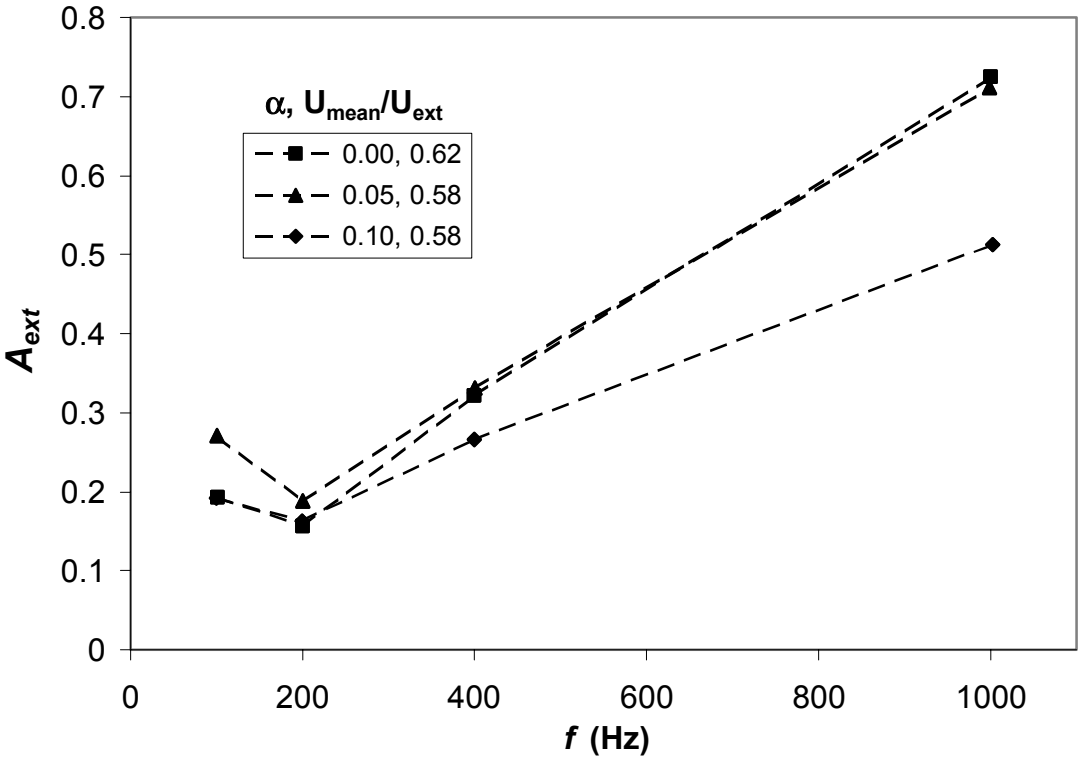

Figure 7.7: Experimental extinction amplitudes for flames with $\phi = 0.75$ and $\alpha = 0.00$, 0.05, 0.10, and $U_{mean}/U_{ext} = 0.62$, 0.58, 0.58.

7.3.3 Experimental and numerical extinction amplitudes

The numerical and experimental extinction values are plotted together in Figure 7.8 for the $\phi = 0.75$, $\alpha = 0.00$ flame. The results in this figure clearly show the matching

trends. The extinction amplitudes appear to match best between the $\kappa_{init}/\kappa_{ext} = 0.8$ and the $U_{mean}/U_{ext} = 0.62$, and the $\kappa_{init}/\kappa_{ext} = 0.95$ with the $U_{mean}/U_{ext} = 0.84$ cases. The fact the experimental and numerical results match between flame conditions $\kappa_{init}/\kappa_{ext} > U_{mean}/U_{ext}$ may point to a change in the previously reported steady extinction velocity. The U_{ext} velocities used in the experiments were from initial tests after the speakers were added to the test rig. If later maintenance altered the rig behavior, the measured U_{ext} values may actually be higher than reported. If this is the case, the U_{mean}/U_{ext} values would be higher bringing the experimental and numerical results to closer agreement.

For the experimental flames, it was not possible to test at U_{mean}/U_{ext} higher than those reported here because the flame could not be maintained even during low amplitude oscillations due to transients in the speaker-driven oscillations as they were adjusted from one condition to another. The flames behaved as if they were very close to the steady state extinction velocity and were susceptible to extinction from speaker oscillations too small to accurately measure. The maximum practical U_{mean}/U_{ext} for these tests was about 0.84.

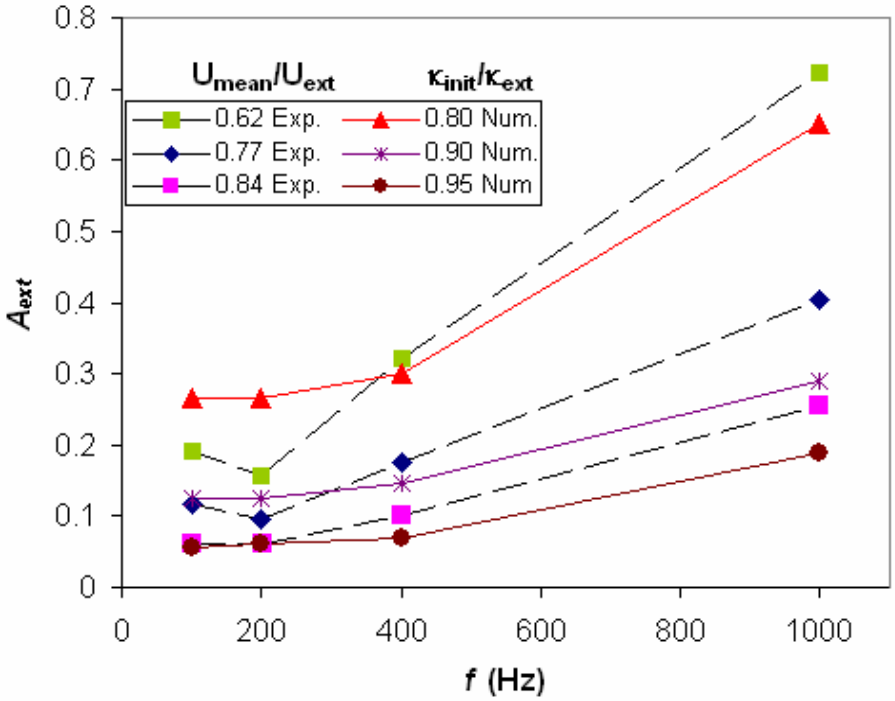

Figure 7.8: Comparison of experimental and numerical extinction amplitudes for ϕ = 0.75 and α = 0.00 for three initial experimental and computational initial flames.

A second comparison of experimental and numerical results is plotted in Figure 7.9 for the ϕ = 0.75, α = 0.05 flame. These results are similar to those in Figure 7.8 in that the trends match but the magnitudes do not. Furthermore, if the steady state extinction velocity was actually lower during these tests, the experimental and numerical results may be closer. It can also be seen, especially in Figure 7.8, that the lower frequency values agree better than the higher frequency. This would support the earlier conclusion that at lower frequencies flames act more like steady state flames. Fuel compositions with similar ϕ's extinguish under similar conditions. As the oscillation frequency increases, the flow oscillation frequency timescales become more important and the flame behavior diverges from the low frequency response.

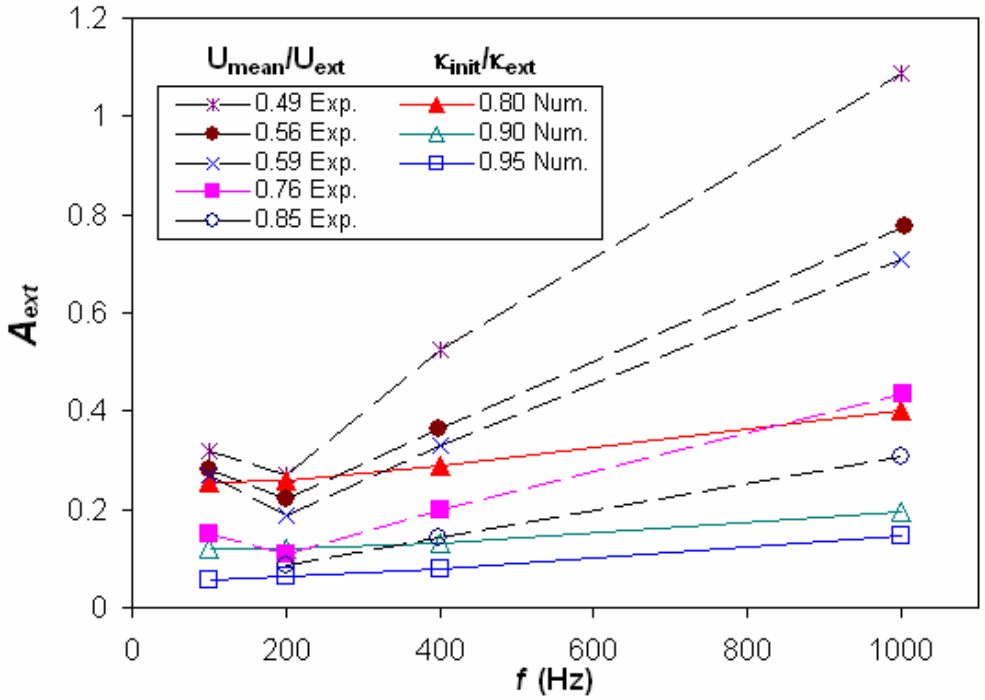

Figure 7.9: Comparison of experimental and numerical extinction amplitudes for ϕ = 0.75 and α = 0.05 for four experimental and computational initial flames.

As mentioned above, none of the extinction experiments were conducted with the flow preheated to 300°C. This makes it difficult for a direct comparison between the experimental and numerical A_{ext}. To check the significance of the difference in initial temperature, a set of computational cases were completed to determine A_{ext} versus f for a premixed composition of ϕ = 0.75, α = 0.05 with an initial temperature of 27°C, $\kappa_{init}/\kappa_{ext}$ = 0.80 and U_{mean} = 3.84m/s. The A_{ext} results can be seen in Figure 7.10. When these results are compared to those in Figure 7.9, it can be seen that the non-preheated A_{ext} are similar to the preheated values for low frequency oscillations of 100 and 200Hz. At higher oscillation frequencies, the non-preheated A_{ext} are much higher than the preheated computational values. It must be pointed out that the A_{ext} values are relative amplitudes. Since the mean axial velocity is much lower for the non-preheated cases (comparing to

numerical cases in Table 4.2 and experimental cases in

Table 7.1), the absolute magnitude of the velocity oscillation is much higher for the preheated case. It can also be seen that the non-preheated A_{ext} values match the trends of the experimental results, but again do not match the actual values. These results lead to the conclusions that the A_{ext} values are a function of preheat temperature but the change in A_{ext} caused by lower initial temperatures can not account for the discrepancy between the numerical and experimental A_{ext} values.

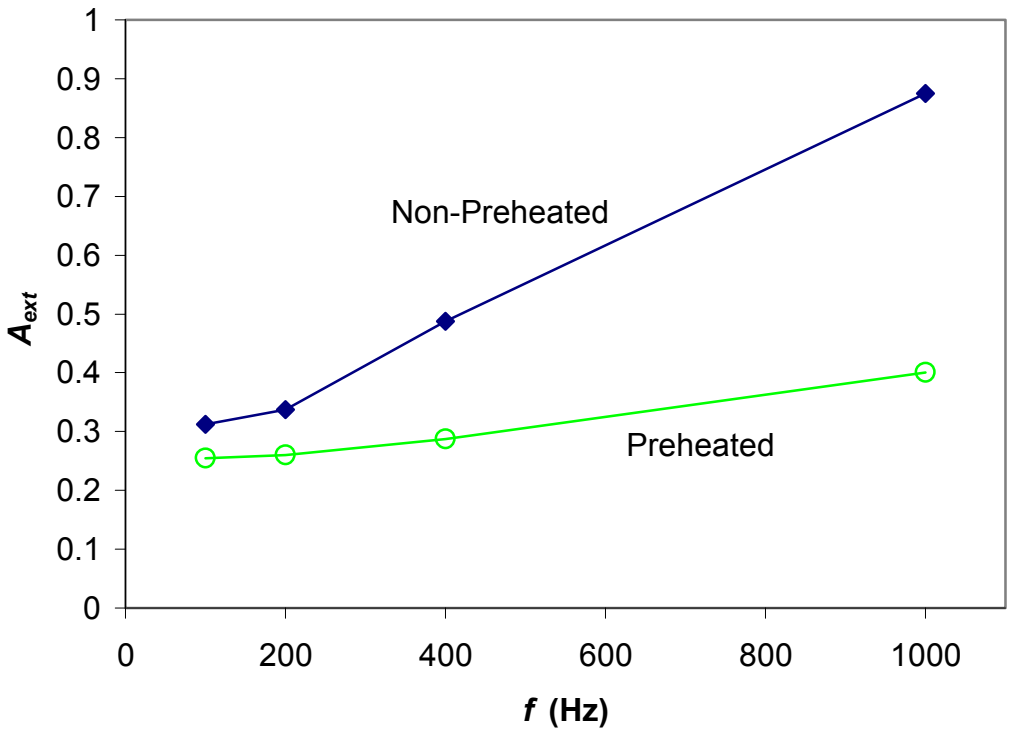

Figure 7.10: Numerical prediction of A_{ext} versus f for non-preheated flame CH_4/H_2-air flame with $\phi = 0.75$, $\alpha = 0.05$ and $\kappa_{init}/\kappa_{ext} = 0.80$.

7.4 LDA Measurements

Laser Doppler Anemometry (LDA) was used to measure velocity profiles within the counterflow regime of several oscillating flames. The LDA system measured particle

velocities at each point in a grid of locations along the counterflow centerline. Due to temperature constraints on the acoustic speakers, running experiments with the reactant preheated to 300°C was not feasible. The speakers are cooled using bypass air, but each LDA test required on the order of 30 minutes to collect the data. The speakers could not be kept cool over that long of a test. Therefore, the tests were run with either very low preheat or no preheat at all. A table describing each of the test cases can be seen in Table 7.2. The results of the LDA tests were used to help validate the trends discovered from the computational results.

Table 7.2: Table of all the LDA test cases and their descriptions.

Test Case	ϕ	α	f **(Hz)**	U_{in} **(m/s)**	**Preheat**
1	0.75	0.10	200	5.5	None
2	0.75	0.10	200	5.5	None
3	0.75	0.10	400	5.5	None
4	0.75	0.10	400	5.5	None
5	0.75	0.05	400	5.5	None
6	0.75	0.05	400	5.5	None
7	0.75	0.10	400	7.5	60°C
8	0.75	0.10	400	8.5	60°C

For each case, the test was conducted and the data reduced as previously described. Unfortunately, the data for Test Case 1 did not provide reasonable results. The predefined set of grid points for Case 1 did not provide adequate resolution of the

flame zone for the results to be of any use. After Test 1, the grid was modified and the new grid was used for Tests 2, 3, 4, 5 and 6. For Tests 7 and 8, the flames were closer to the actual center and second new grid was used.

Figure 7.11 is a plot of the velocity profiles for Test Cases 2, 3 and 4, a $\phi = 0.75$, $\alpha = 0.10$ flame, at the instant in the cycle when the inlet velocity is equal to U_{mean}. The velocities were measured at the grid locations spanning the distance between the two nozzles. At measurement location 0mm, the laser is just touching the exit plane of the upper nozzle. At location 4.75mm, the laser is just touching the exit plane of the lower nozzle. The measurement locations span 4.75mm of the approximately 7.0mm total separation distance between the nozzles.

In Figure 7.11, the positive velocities are near the bottom nozzle and the negative velocities are above the stagnation plane and near the top nozzle. The counterflow flames are not centered geometrically and are closer to the bottom nozzle. However, both nozzles were flowing the correct mixture composition, so the flames may balance themselves between the two nozzles with no adverse effects on experimental accuracy. The non-centered flames spread out the counterflow region for the upper nozzle, making it easier to resolve flow details. Therefore, only measurements for the top nozzle are used in this study.

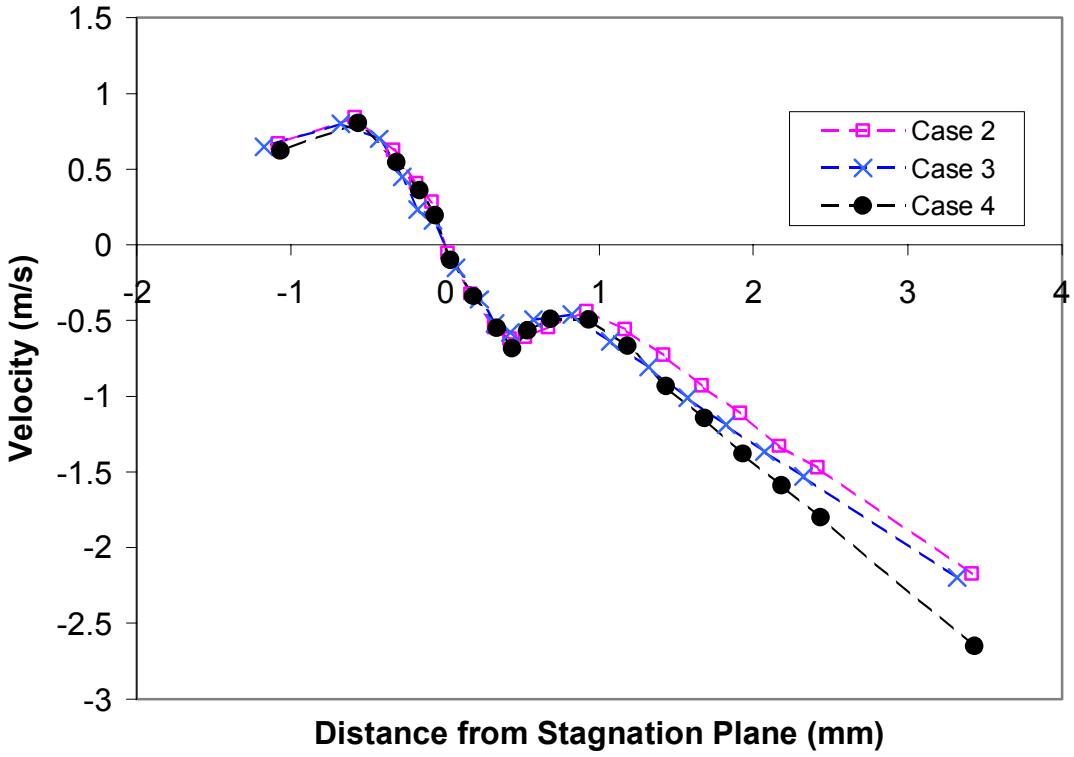

Figure 7.11: Mean experimental velocity profiles of the cycle averaged measurements for Test Cases 2, 3, and 4.

The profiles in Figure 7.11 are very similar to each other even though Case 1 is at 200Hz and Cases 3 and 4 are at 400Hz. All the profiles converge to approximately the same profile from the beginning of the flame zone to the stagnation plane. The flame zone is characterized by strong heating of the incoming flow and causes the bulk flow to expand and accelerate. After passing through the large temperature increase at the beginning of the flame zone, the flow then slows approaching the stagnation plane. The fact that the 200 and 400Hz profiles are so similar shows that oscillating at moderate frequencies does not affect significant changes to the mean properties in and near the flame zone. In addition, the fact that the velocity profiles are similar and repeatable over the three test cases provides confidence in the measurement accuracy.

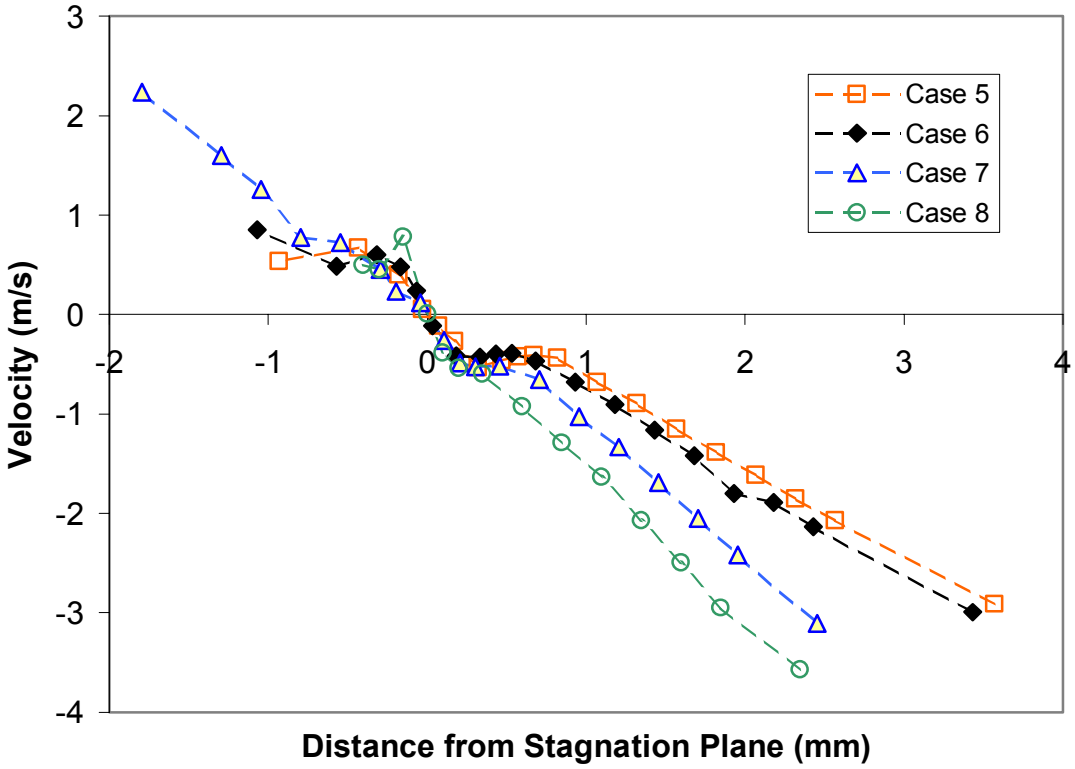

Figure 7.12: Mean experimental velocities profiles of the cycle averaged measurements for Tests Cases 5, 6, 7, and 8.

Figure 7.12 is a plot of the mean velocity profiles at U_{mean} for Cases 5, 6, 7 and 8. Cases 5 and 6 had a similar problem with the flame unbalance that again lead to the profiles for the lower nozzle being unreliable. The flames for Cases 5 and 6 are for a flame with $\phi = 0.75$ and $\alpha = 0.05$. The reduction in H_2 mass fraction makes the steady state flame weaker than the $\alpha = 0.10$ cases. When compared to the mean velocity profiles for Cases 2, 3, and 4, it can be seen that the expansion region for this weaker flame has moved closer to the stagnation plane. Also, the magnitude of the acceleration is smaller for Cases 5 and 6. This is a validation of the one-dimensional steady state

computational results which show that a reduction of H_2 leads to a weaker flame with the same characteristics described here.

Test Cases 7 and 8 used moderate preheating of 60°C to improve the flow balancing and better center the flames. Furthermore, the nozzle exit velocity was increased to push the flame closer to the steady state extinction strain. The profiles for these two cases are very similar from the top nozzle exit through the flame zone until near the stagnation plane. During the Case 8 test, the flame extinguished and the profile was not measured beyond the stagnation plane. The upper nozzle profiles for these two cases show very a very weak thermal expansion zone. However, the expansion zone may not be as weak as measured. The higher nozzle exit velocity generates larger velocity gradients, which make it more difficult for the entrained particles to follow gas velocity. Therefore, the particle velocity may not show the true extent of the gas velocity variations and the measured velocity profiles in the acceleration zone may appear flatter than the actual gas velocity profile.

The data in Figure 7.13 are three velocity profiles for Case 2. The three profiles are those measured at the moments in the cycle when the inlet velocity is equal to U_{mean}, U_{max}, and U_{min}, respectively. The plot is centered on the flame region. It can be seen that all three profiles converge to the same velocities in the flame zone. Therefore, the velocities in the flame zone do not change much over one cycle. Because of this, the velocity profiles downstream of the flame are very similar as they approach the stagnation plane.

All three cases show some acceleration of the flow approaching the flame zone. However, the U_{min} case accelerates the most. This higher acceleration occurs because the

flame is stronger at the minimum velocity and the stronger flame generates a stronger expansion zone. The U_{max} velocity causes a weaker flame and accelerates the flow less. Furthermore, at U_{min} the stronger flame affects the flow further from the stagnation plane so the particles are affected by the flow velocity changes over a slightly larger distance than at the other moments in the cycle. This is similar to the numerical transient results that showed increasing velocity caused decreasing flame temperature and decreasing thermal diffusion zone length. The larger acceleration taking place at the U_{min} part of the cycle, and the smaller acceleration at the U_{max} part of the cycle work together to bring the two velocity profiles closer to the mean profile.

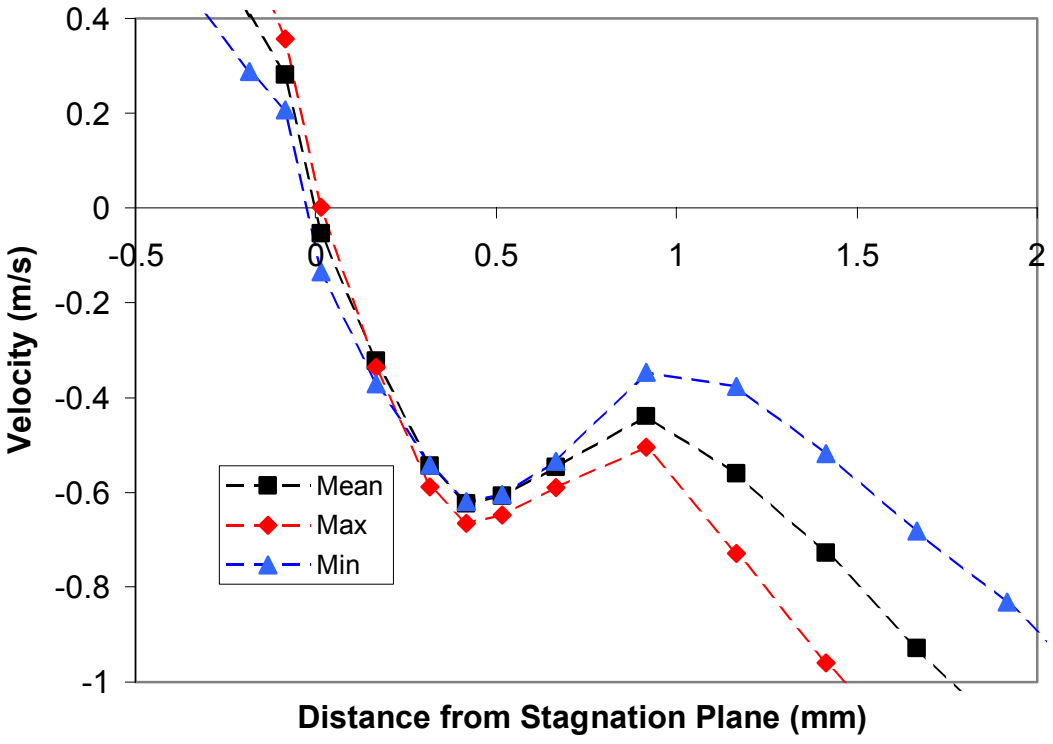

Figure 7.13: Mean, maximum and minimum velocity profiles near the stagnation plane for Test Case 2.

The U_{mean}, U_{min} and U_{max} profiles for Cases 3 and 4 are plotted in Figure 7.14. The difference between Figure 7.13 and Figure 7.14 shows that the 400Hz oscillations have a greater effect on the flame strength than the 200Hz oscillations. This confirms the numerical results that showed increasing the frequency of oscillation has a significant effect on the conditions within the flame zone. The velocity profiles appear similar through the expansion zone. The similarity near the expansion zone is caused by the particle interaction with the flow velocity. As discussed above, the velocity through the expansion zone at the U_{min} profile accelerates the flow more than the velocity of the U_{max} velocity, causing the particle velocities to approach the same profile in the thermal expansion zone.

There is, however, a significant difference in the profiles as they approach the stagnation plane. These differences between the minimum and maximum profiles are not seen in the 200Hz case. When looking at the same measurement location in Figure 7.14 near the stagnation plane, the velocities are lower for all the U_{max} cases. This scatter seems to indicate the 400Hz oscillations impose variations downstream of the thermal expansion zone, while the 200Hz oscillations could not. Cases 5 and 6 also show similar results but are not plotted here.

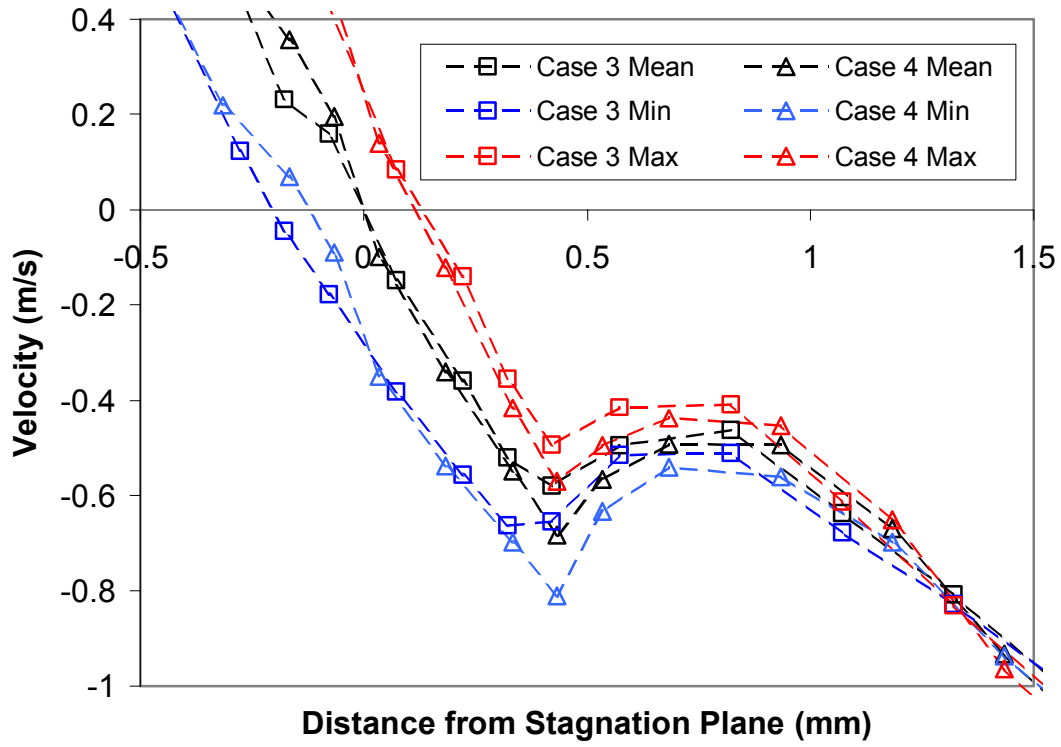

Figure 7.14: Mean, maximum and minimum velocity profiles near the stagnation plane for Test Cases 3 and 4.

7.5 Conclusions

Experiments were conducted using a counterflow test rig with acoustic speakers to impose oscillations on the flow field. Three types of tests were run. The first tests were used to correlate the amplitude of the imposed oscillations to the speaker and flame conditions. The next set of tests measured the extinction amplitudes of several initial flames and the final set of tests measured velocity profiles for oscillating flames using a LDA system.

The experimental results matched the trends shown in earlier numerical models. Increasing α decreases the extinction amplitude for a given initial flame condition. The velocity profiles measured using the LDA system validated both the steady state and

transient modeling results. Furthermore, the profiles helped define the complex interactions between the counterflow region dominated by the bulk flow properties and the region dominated by the combustion and thermal effects. Finally, the non-preheated A_{ext} results show that the extinction amplitudes are a function of the initial temperature. Flames with a lower initial temperature actually had a higher relative extinction amplitude, A_{ext}, but lower absolute extinction amplitudes.

Chapter 8 Summary and Conclusions

8.1 Summary of Work

This study of premixed, multi-component flames was motivated by the documented benefits of H_2 addition to a steady state system. H_2 addition improves the lean flame stability by extending the lean extinction limit beyond that of pure CH_4 at the same equivalence ratio. Adding H_2 to a hydrocarbon-air reactant mixture creates a multi-component fuel mixture. Such mixtures are becoming more important in modern combustion systems. Simplified models predicting flame temperature for these conditions are of use in examining the contributions of each fuel species to the overall flame properties. Furthermore, the effects of H_2 addition to hydrocarbon flames exposed to strain rate transients are only beginning to be investigated.

This study investigated the effects of mixture composition on flame properties and stability of lean, premixed hydrocarbon-air flames. Analytical, experimental and numerical studies were conducted to examine the effects of H_2 addition to CH_4 and analytical studies also investigated C_3H_8/H_2-air flames. All three methods were based on premixed, counterflow flames.

8.2 Conclusions

Two analytical relations were developed to predict T_{flame} based on Le and imposed non-dimensional strain. Both results gave identical predictions for single component fuels and these results were also identical to published results of prior integral analyses. When applied to multi-component fuels, the T_{flame} predictions varied between the relations. The analytical predictions were compared to a computational flame model

which used detailed chemistry and species diffusion. The relation developed assuming discrete reaction zones for each fuel species correctly captured the linear response of the reacting mixtures to low strain, $Ka < 0.2$. The discrete model was able to capture the correct behavior for both lean CH_4/H_2, with *Le* generally less than 1.0, as well as for lean C_3H_8/H_2 mixtures, with *Le* generally greater than 1.0. H_2 addition to the C_3H_8 mixture lowers the effective *Le* of the reactant composition. An effective *Le* could be calculated, Le_{eff}, which when used with the analytical models would predict the correct response of the flame to imposed strain.

The numerical investigations were conducted using a computer code to model the counterflow domain including detailed chemistry and diffusion effects. The code provided extinction amplitudes, A_{ext}, and time varying mass fractions of species and flow velocities. The results showed that, when exposed to oscillations of $f = 100$ or 200Hz, the flame is able to maintain a quasi-steady state response. At higher frequencies, a phase lag develops between the imposed oscillation and the flame response. The flame acts as a low pass filter. As frequency increases, the flame response attenuates which causes A_{ext} to increase with increasing f.

The experimental investigations measured extinction amplitudes, A_{ext}, of the imposed oscillations for CH_4-H_2-air flames. The measured A_{ext} matched the trends found with the numerical results. A_{ext} decreases with increasing ϕ or α. When ϕ or α are increased, the flame temperature is increased, which in turn increases the reaction rate in the flame zone. The increased reaction rates allow the flame to more easily adjust to the oscillating conditions and maintain the quasi-steady state behavior. Therefore, these

flames will extinguish at lower strain rates while flames with lower ϕ or α may be sustained through momentary excursions beyond the steady state extinction strain rate.

8.3 Recommendations

This investigation served to answer many questions concerning transient and multi-component combustion. However, many other questions were raised as well. Further work could be done in all three areas of this investigation to extend the results found here.

The multi-component integral analysis could be extended to account for the non-linear effects of higher strain rates. This would have to include the effects of the flame zone decreasing in size as it is constrained against the stagnation plane while the flow velocity increases and would allow for the prediction of steady state strain induced extinction. Furthermore, it would be interesting to determine if the simplified models could be used to model the flame properties under transient strain rate conditions.

The numerical modeling results could be extended to investigate the response of fuels other than CH_4. C_3H_8, with a $Le > 1.0$ for lean flames, would provide interesting data to compare with the current CH_4 results. In addition, investigating the flame response to impulsive changes in conditions, versus oscillatory, may provide insight into the flame's ability to maintain quasi-steady behavior.

Finally, it would be very beneficial if the experimental test rig could operate reliably for long tests at elevated temperatures. While measuring extinction amplitudes, the rig required periodic downtimes to allow for cooling of the speakers. The interruptions made the extinction tests difficult to run. Furthermore, running for longer operating times would allow preheating the flow during the LDA tests. This would allow

tests at higher mean velocities which would, in turn, improve the seeding quality and LDA.

Bibliography

1. Jackson, G.S., et al., *Influence of Hydrogen on the Response of Lean Methane Flames to Highly Strained Flows.* Combustion and Flame, 2003. **132**(3): p. 503-511.

2. Jackson, G.S., et al., *Erratum: Influence of H2 on the response of lean premixed CH4 flames to high strained flows.* Combustion and Flame, 2003. **135**(3): p. 363.

3. Vagelopoulos, C.M. and F.N. Egolfopoulos, *Laminar Flame Speeds and Extinction Strain Rates of Mixtures of Carbon Monoxide with Hydrogen, Methane, and Air.* Twenty-Fifth Symposium (International) on Combustion, The Combustion Institute, Pittsburgh, 1994.

4. Yu, G., C.K. Law, and C.K. Wu, *Laminar Flame Speeds of Hydrocarbon + Air Mixtures with Hydrogen Addition.* Combustion and Flame, 1986. **63**: p. 339-347.

5. Gauducheau, J.L., B. Denet, and G. Searby, Combustion Science and Technology, 1998. **137**: p. 81.

6. Flores, R.M., V.G. McDonnell, and G.S. Samuelsen, *Impact of Ethane and Propane Variation in Natural Gas on the Performance of a Model Gas Turbine Combustor.* J. Eng. Gas Turbines Power, 2003. **125**(3): p. 701-708.

7. Flores, R.M., et al., *Response of a Model Gas Turbine Combustor to Variation in Gaseous Fuel Composition.* J. Eng. Gas Turbines Power, 2001. **123**(4): p. 824-831.

8. Maiya, P.S., et al., *Maximizing H2 Production by Combined Partial Oxidation of CH4 and Water Gas Shift Reaction.* Applied Catalysis A: General, 2000. **196**: p. 65-72.

9. Sankaran, R. and H.G. Im, *Dynamic Flammability Limits of Methane-Air Premixed Flames with Mixture Composition Fluctuations.* Proceedings of the Combustion Institute, 2002. **29**.

10. Tsuji, H. *Experimental Studies of Near Limit Flames Using Counterflow Flame Techniques*. in *ASME-JSME Thermal Engineering Joint Conference Proceedings*. 1983. Honolulu, HI.

11. Peters, N., *Turbulent Combustion*. 2000, Cambridge, UK: Cambridge University Press.

12. Sai, R., et al. *Further Studies on Lean Stability of Premixed CH4 H2 Flames*. in *2001 Technical Meeting of the Eastern States Section of the Combustion Institute*. 2001.

13. Bradley, D., P.H. Gaskell, and X.J. Gu, *The Modeling of a Aerodynamic Strain Rate and Flame Curvature Effects in Premixed Turbulent Combustion.* Twenty-Seventh Symposium (International) on Combustion, The Combustion Institute, 1998(1998): p. 849-856.

14. Chung, S.H. and C.K. Law, *An Integral Analysis of the Structure and Propagation of Stretched Premixed Flames.* Combustion and Flame, 1988. **72**: p. 325-336.

15. Im, H.G., J.H. Chen, and J.Y. Chen, *Chemical response of methane air diffusion flames to unsteady strain rate.* Combustion and Flame, 1999. **118**(1-2): p. 204-212.

16. Law, C.K. and C.J. Sung, *Structure, Aerodynamics, and Geometry of Premixed Flamelets.* Progress in Energy and Combustion Science, 2000. **26**(4-6): p. 459-505.

17. Stahl, G. and J. Warnatz, *Numerical Investigation of Time-Dependen Properties and Exinction of Strained Methane- and Propane-Air Flamelets.* Combustion and Flame, 1991. **85**: p. 285-299.

18. Sun, C.J. and C.K. Law, *On the Nonlinear Response of Stretched Premixed Flames.* Combustion and Flame, 2000. **121**: p. 236-248.

19. Sung, C.J. and C.K. Law, *Structural sensitivity, response, and extinction of diffusion and premixed flames in oscillating counterflow.* Combustion and Flame, 2000. **123**(3): p. 375-388.

20. Plaia, J.M. and G.S. Jackson, *Effects of CH4/H2 Fuel Mixture Composition on the Transient Response of Strained Premixed Flames.* Proceedings of the Third Joint Meeting of the U.S. Sections of The Combustion Institute, 2003.

21. Sankaran, R. and H.G. Im, *Effect of Hydrogen Addition on the Flammability Limit of Stretched Methane/Air Premixed Flames.* Proceedings of the Third Joint Meeting of the U.S. Sections of The Combustion Institute, 2003.

22. Buckmaster, J., *The Quenching of a Deflagration Wave Held in Front of a Bluff Body.* Seventeenth Symposium (International) on Combustion, The Combustion Institute, 1979: p. 835-842.

23. Buckmaster, J., *The Effects of Radiation on Stretched Flames.* Combustion Theory and Modeling, 1997. **1**: p. 1-11.

24. Buckmaster, J. and D. Mikolaitis, *A Flammability-Limit Model for Upward Propagation through Lean Methane/Air Mixtures in a Standard Flammability Tube.* Combustion and Flame, 1982. **45**: p. 109-119.

25. Sivashinsky, G.I., Acta Astronautica, 1997. **4**: p. 1177-1206.

26. Kee, R.J., et al., *A FORTRAN Computer Code Package for the Evaluation of Gas-Phase Multicomponent Transport Properties*. 1986, Sandi National Laboratories.

27. Kee, R.J., F.M. Rupley, and J.A. Miller, *Chemkin-II: A Fortran Chemical Kinetics Package for the Analysis of Gas-Phase Chemical Kinetics*. 1991, Sandia National Laboratory.

28. Dixon-Lewis, G., *Aspects of Laminar Premixed Flame Extinction Limits.* Proceedings of the Combustion Institute, 1994. **25**: p. 1325-1332.

29. Kee, R.J., et al., *A Computational Model of the Structure and Extinction of Strained, Opposed Flow, Premixed Methane-Air Flames.* Proceedings of the Combustion Institute, 1988. **22**: p. 1479-1494.

30. Korusoy, E. and J.H. Whitelaw, *Extinction and Relight in Opposed Flames.* Experiments in Fluids, 2002. **33**: p. 75-89.

31. Williams, F.A., *Progress in Knowledge of Flamelet Structure and Extinction.* Progress in Energy and Combustion Science, 2000. **26**: p. 657-682.

32. Guo, H., J. Yiguang, and T. Niioka, *Effects of Radiative Heat Loss on the Extinction of Counterflow Preximed H2-Air Flames.* Combustion Theory and Modeling, 2000(4): p. 459-475.

33. Schuermans, B.B.H. and W. Polifke. *Modeling Transfer Matrices of Premixed Flames and Comparison with Experimental Results*. in *International Gas Turbine & Aeroengine Congress & Exposition*. 1999. Indianapolis, Indiana: ASME.

34. Buchner, H., C. Hirsch, and W. Leuckel, Combustion Science and Technology, 1993. **94**: p. 219.

35. Sardi, K., A.M.K.P. Taylor, and J.H. Whitelaw, *Extinction of Turbulent Counterflows Under Periodic Strain.* Combustion and Flame, 2000. **120**: p. 265-284.

36. Im, H.G. and J.H. Chen, *Effects of Flow Transients on the Burning Velocity of Laminar Hydrogen/Air Premixed Flames.* Proceedings of the Combustion Institute, 2000. **28**: p. 1833-1840.

37. Im, H.G., et al., *A Numerical Study of Transient Ignition in a Counterflow Nonpremixed Methane-Air Flame Using Adaptive Time Integration.* Combustion Science and Technology, 2000. **158**: p. 341-363.

38. McIntosh, A.C., J. Brindley, and X.-S. Yang, Combustion Theory and Modeling, 2002. **6**: p. 35.

39. Clavin, P. and G. Joulin, *High-Frequency Response of Premixed Flames to Weak Stretch and Curvature: a Variable-Density Analysis.* Combustion Theory and Modeling, 1997. **1**: p. 429.

40. Grcar, J.F., *The TWOPOINT Program for Boundary Value Problems*. 1996, Sandia National Laboratories: Albuquerque.

41. Bowman, C.T., et al., *GRI-Mech 3.0*., http://www.me.berkeley.edu/gri_mech/.

42. Sung, C.J., J.B. Liu, and C.K. Law, *Structural Response of Counterflow Diffusion Flames to Strain- Rate Variations.* Combustion and Flame, 1995. **102**(4): p. 481-492.

43. Sai, R., *A Study on the Effects of H2 Addition to Highly Strained Lean Premixed Laminar Methane and Propane Flames*, in *Mechanical Engineering*. 2003, University of Maryland: College Park.

44. Egolfopoulos, F.N., D.L. Zhu, and C.K. Law, *Experimental and Numerical Determination of Laminar Flame Speeds: Mixtures of C2-Hydrocarbons with Oxygen and Nitrogen.* Proceedings of the Combustion Institute, 1990. **23**: p. 471-478.

45. Giovangigli, V. and M.D. Smooke, *Adaptive Continuation Algorithms with Application to Combustion Problems.* Applied Numerical Mathematics, 1989. **5**: p. 305-331.

46. Smooke, M.D., et al., *Comparison Between Expermental Measurements and Numerical Calculations of the Structure of Counterflow, Diluted, Methane-Air, Premixed Flames.* Proceedings of the Combustion Institute, 1990. **23**: p. 463-470.

47. Raja, L.L., R.J. Kee, and L.R. Petzold, *Simulation of the Transient, Compressible, Gas-dynamic Behavior of Catalytic-Combustion Ignition in Stagnation Flows.* Proceedings of the Combustion Institute, 1998. **27**: p. 2249-2257.

48. Patankar, S.V., *Numerical Heat Transfer and Fluid Flow*. 1980: Hemisphere Publishing Corporation.

49. Petzold, L.R., *Computer Methods for Ordinary Differential Equations and Differential-Algebraic Equations*. 1998, Philadelphia, PA: Society for Industrial and Applied Mathematics. 314.

50. Petzold, L.R., *DASSL*. 1991, Lawrence Livermore National Laboratory: Livermore, CA.

51. Ehrig, R. and U. Nowak, *LIMEX*. 2000, Konrad-Zuse-Zentrum fuer Informationstechnik: Berlin-Dahlem.

52. Sung, C.J., C.K. Law, and J.Y. Chen, Twenty-Eighth Symposium (International) on Combustion, The Combustion Institute, Pittsburgh, 1998: p. p.295.

53. Panton, R.L., *Incompressible Flow*. 1996, New York: John Wiley & Sons, Inc.

54. Cong, Y., *The Effects of Hydrgen Doping on Lean Stability of Premixed Flames*, *Mechanical Engineering*. 1999, University of Maryland: College Park.

55. Dantec, D.A.S., *BSA Flow Software Installation & User's Guide*. 7th Edition ed. 2002, Skovunde, Denmark: Dantec Dynamics A/S.

56. Sung, C.J., J.B. Liu, and C.K. Law, *On the Scalar Structure of Nonequidiffusive Premixed Flames in Counterflow.* Combustion and Flame, 1996. **106**(1-2): p. 168-183.

57. Press, W.H., et al., *Numerical Recipes in Fortran 77 The Art of Scientific Computing Second Edition*. Vol. 1. 1992, Cambridge: Press Syndicate of the University of Cambridge.